ANALYSIS OF BALL BEARING DEFECTS IN SYNCHRONOUS MACHINES

USING ELECTRICAL MEASUREMENTS

A Dissertation

by

TENGXI WANG

Submitted to the Office of Graduate and Professional Studies of
Texas A&M University
in partial fulfillment of the requirements for the degree of

DOCTOR OF PHILOSOPHY

Chair of Committee,	Alexander G. Parlos
Committee Members,	Gholamreza Langari
	Won-Jong Kim
	Edgar Sanchez-Sinencio
Head of Department,	Andreas A. Polycarpou

August 2017

Major Subject: Mechanical Engineering

ABSTRACT

Rolling element bearings are used in most electrical machines, especially for small and medium size applications. Under non-ideal operating conditions, ball bearing condition degrades by fatigue, ambient vibration, misalignment, overloading, contamination, corrosion from water or chemicals, improper lubrication, shaft currents and residual stress left from the bearing manufacturing process. All of these conditions eventually lead to increased vibration and acoustic noise during machine operation which at some point in time results in unexpected bearing failure. Over the years, a great number of publications have been devoted to the detection of mechanical faults, including rolling element bearing defects and torsional defects, in electrical machines based on Electrical Signature Analysis (ESA). It has been observed that these faults can affect either the stator to rotor air-gap distribution or the running speed of the machine, which can be reflected in the signature of the electrical signals. However, the physical link between the mechanical degradation and the electrical signature is still not explained well.

A multi-physics model is developed by joining the detailed mechanical model of a rotor bearing system and the electrical model of a synchronous machine in this research. This combined model is capable of describing the transmission of information originating from bearing faults and their impact on the variations of the measured electrical signals. The electrical machine model is developed based on winding function approach and its validity is demonstrated by a more accurate Finite Element Method (FEM) model. The mechanical model consists of a high fidelity rotor-bearing system with detailed nonlinear

ball bearing model and a flexible finite element shaft model. It is validated using the housing vibration data collected from some experiments.

Generalized roughness bearing anomalies are linked to load torque ripples and airgap variations, while being related to current signature by phase and amplitude modulation. Considering that the induced characteristic signatures are usually subtle broadband changes in the current spectra, these signatures are easily affected by input power quality variations, machine manufacturing imperfections and environmental noise.

In this research, a new algorithm is proposed to isolate the influence of the external disturbances of power quality, machine manufacturing imperfections and environmental noise, and to improve the effectiveness of applying the ESA for generalized roughness bearing defects. The results show that the proposed method is effective in analyzing the generalized roughness bearing anomaly in synchronous machines. Furthermore, the electrical signatures are analyzed in a synchronous machine with bearing defects. The proposed fault detection method employs a Zoomed Fast Fourier Transform (ZFFT) and Principal Component Analysis (PCA) and it is also tested on the available experimental data. The results show that amplitude induced electrical harmonics are related to the level of vibration, and the electrical signatures are affected heavily by other variables, such as power quality and load fluctuation. The proposed method is shown to be effective on detecting generalized roughness bearing defects in synchronous machines.

ACKNOWLEDGEMENTS

I would like to express my deepest gratitude to my academic advisor, Dr. Alexander G. Parlos, for helping and guiding me to finish this research. Without his technical knowledge and patience, this work would not have been possible. I am also very grateful to Dr. Won-Jong Kim, Dr. Reza Langari, and Dr. Jose Silva-Martinez, for serving as the members of my graduate committee.

Thanks also go to my friends and colleagues, especially, Pang-Chun Chu, Yong Li, Gang Li, and Jianxi Fu for making my time at Texas A&M University a great experience.

Finally, thanks to my beloved mother and father for their encouragement and to my dear wife for her patience and love.

NOMENCLATURE

CM	Condition Monitoring
SPSM	Salient Pole Synchronous Machine
ESA	Electrical Signature Analysis
WFA	Winding Function Approach
FEM	Finite Element Method
AM	Amplitude Modulation
EDM	Electrical Discharge Machining
SE	Static Eccentricity
DE	Dynamic Eccentricity
ME	Mixed Eccentricity
IR	Inner Race Fault
OR	Outer Race Fault
DOF	Degrees of Freedom
PCA	Principal Component Analysis
ZFFT	Zoom Fast Fourier Transform
RMS	Root Mean Square
THD	Total Harmonics Distortion

TABLE OF CONTENTS

LIST OF FIGURES

LIST OF TABLES

CHAPTER I

INTRODUCTION AND LITERATURE REVIEW

1.1 Overview

Ranging from high voltage generators used in decentralized power plants including electric utilities and district heating plants to low voltage generators which are ideal for standalone and emergency power supplies for schools, hospitals, offices and factories, synchronous AC generators are widely used in the power generation industry. For example, the capacity of installed diesel generators in the United States, reportedly as high as 350,000 units with more than 127 gigawatts [1], constitutes a significant component of the nation's power generating infrastructure.

The reliable operation of power generation systems is very critical because of the enormous financial losses resulting from disruption of production, machine replacement, human injury and/or fatality, etc. [2]. Although synchronous AC generators are generally well manufactured and robust, mechanical anomalies, such as the sub-synchronous resonance induced by load troubles, high vibrations resulting from worn bearings, and greater torque variation and oscillation caused by faulty prime mover are likely to occur in abnormal conditions. These incipient faults, which degrade system performance can also lead to failures of other components, finally resulting in an unexpected outage event. System operators use condition monitoring (CM), which is a major component of predictive maintenance, to monitor machinery and schedule appropriate maintenance based on the information that CM provides. By using CM, maintenance planners can arrange service during a planned downtime and avoid the costs of an unexpected outage.

Vibration analysis is the most commonly used technique for CM [3]. Housing vibration is measured through a seismic or piezo-electric accelerometer mounted on the machine housing. For machines with more critical reliability requirements, radial vibration of the shaft is directly measured by an eddy-current proximity sensor mounted on the bearing casing. Torsional vibration is measured by a strain gauge directly on the surface of the shaft or an encoder attached to it. In a common vibration analysis procedure, the vibration data collected and the historical baseline data are compared to observe any trends indicative of possible failure.

Although vibration analysis is quite sensitive to the mechanical anomalies and has proved its effectiveness in many situations [4] [5], it can be expensive, difficult to use and hard to interpret. While large industrial machines equipped with journal bearings and built-in diagnosis sensors can easily be adapted with the technique mentioned above, smaller electrical machines that are often equipped with rolling-element bearings and have no built-in vibration sensors, require additional sensors. Since the associated accessories result in higher production and maintenance expenses for smaller machines, the application of CM is limited to large and expensive machines [6]. Furthermore, the characteristics of the vibration signal obtained are always related with the sensor's mounting location and orientation. A vibration in a particular part of the mechanical component is altered while transmitting through the material, which will separate the source from the accelerometer. The requirement of professional knowledge of the machine's vibration transmission characteristics makes it difficult to interpret the vibration signal. For example, background noise caused by external devices can interfere with the

vibration signal. Therefore, the industry increasingly demands low-cost, non-intrusive, and simple-to-use CM technologies and products that can be integrated with the existing systems and maintenance planning.

Electrical signature analysis (ESA) was first developed and patented in 1990 by Oak Ridge National Laboratory to overcome the shortcomings of the traditional vibration method [7]. ESA is based on the concept that a system's electrical machine generating power/torque also acts as a built-in transducer. Changes in the mechanical/electrical system will induce variations in electrical signals, e.g., voltages and currents. These signals, although small compared to the total energy provided by the machine, can be extracted through modern signal processing technology to characterize the system's overall health condition. ESA is an attractive technology for the following reasons:

- Equipment-mounted sensors are unnecessary

- Monitoring a system's health condition can be done remotely and non-intrusively

- Continuous monitoring capability for online condition assessment is provided

- Applicability to both large and small electrical machines, either AC or DC

- High sensitivity to a range of mechanical disorders, e.g., misalignment, worn bearings and gears, loose belts, and degraded power systems

Surveys Of Electric Machine Failures

	Bearing	Stator	Rotor	Other
PCIC Survey 1994	836	258	117	426
ERPI Survey 1985	431	379	95	147
IEEE-IAS Survey 1985	319	175	58	132

Pie chart: Bearing 47%, Stator 24%, Rotor 8%, Other 21%
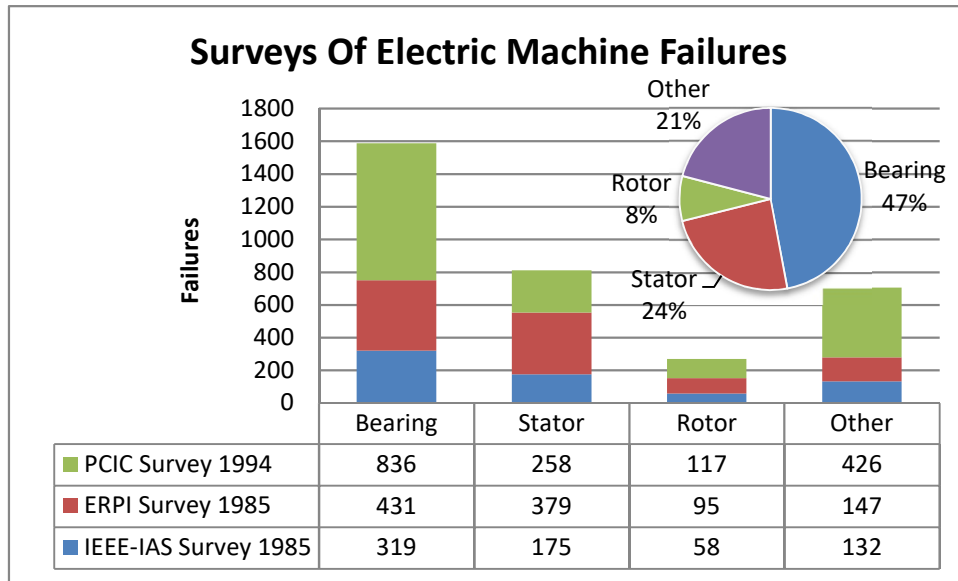
Figure 1 Surveys of electric machine failures

About 60% of the common failures in the components of an electrical machine can be attributed to malfunctions of mechanical components, such as worn bearings, cracked shafts, etc. Figure 1 reports the results of the IEEE-IAS and ERPI surveys in 1985 and the PCIC Survey in 1994 [8]. It is clear that about half of failures are initiated in the bearings. Single point/localized defect, and generalized roughness/distributed defect are two major classes of faults in rolling element bearings used by most electrical machines. The former usually occurs as pits, spalls, or cracks on a raceway or rolling elements, and the latter usually occurs because of contamination, lack or loss of lubrication, corrosion, etc., Unlike the characteristic defect frequencies of signal point faults, the induced characteristic signature is usually a subtle broadband change in the spectrum [9] [10]. More studies are needed to understand how this type of bearing fault affects the electrical signature.

Other than bearing faults, torsional vibration is another common issue in power generation system. Excessive torsional oscillation of a rotor can lead to fatigue, gear damage, power fluctuations, etc. Generally, calculations of the torsional natural frequencies occur during the design phase, rather than in the testing phase. As mentioned, using a strain gauge or an encoder to monitor torsional oscillation increase the complexity of the system and makes it less robust. Hence, cost-effective ESA technology has a great potential in this area.

1.2 Literature Review

This subsection summarizes the important mechanical failures in electrical machines and the corresponding diagnosis techniques proposed in the literature. Modeling methods for both electromagnetic circuit and bearing faults are reviewed to give a clearer understanding of ESA.

1.2.1 Diagnosis of Mechanical Faults Using ESA

1.2.1.1 Bearing Faults

Under non-ideal operational conditions, rolling element bearings are gradually deteriorated by fatigue, ambient vibration with non-uniform forces on the balls, misalignment, overloading, contamination, water or chemical corrosion, incorrect lubrication, and shaft current and residual stress left from the manufacturing process, which eventually lead to increased vibration and acoustic noise during machine operation which at some level results in unexpected system failures. According to [11], bearing faults can be categorized into single point defect and generalized roughness defect, or into

localized fault and extended/distributed fault [5, 12]. Limited literature has been reported on the subject of diagnosis rolling element bearing faults in synchronous machines using ESA, while there are plenty of published papers dealing with bearing fault for induction machines in the last decade. Considering the similarities in electrical machines, some of the proposed ESA techniques for induction machines can serve as a guideline for this research on synchronous generators.
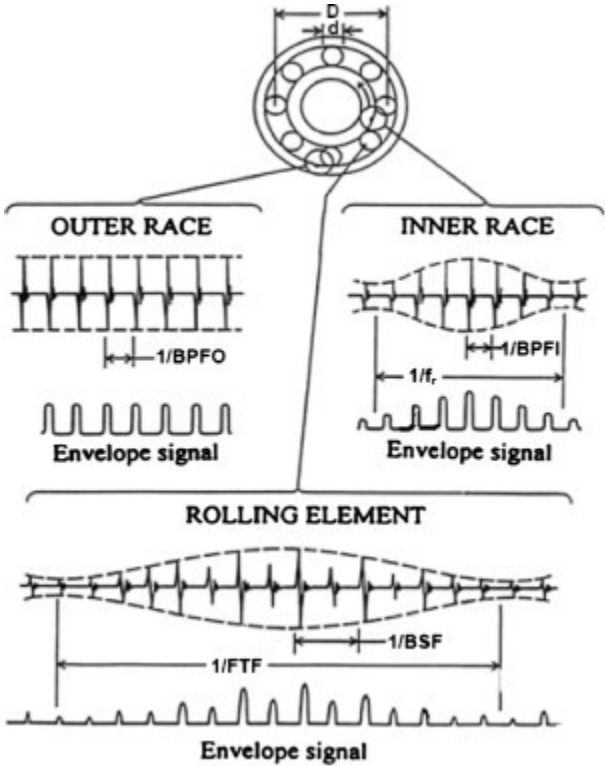
Figure 2 Typical vibration signals from localized faults in rolling element bearings [5]

A single point defect produces sharp impulses when the rolling element passes the defected area on raceways. The impulses generate mechanical vibrations at the rotational speeds of the defected component. Figure 2 shows the structure and typical vibration signals from localized faults in different components of a rolling element bearing, where

BPFO, BPFI, FTF, and BSF are the ball passing frequency for outer race, ball passing frequency for inner race, fundamental train frequency/cage frequency, and ball spin frequency, respectively. Periodically, the vibrations can cause air-gap variations between the stator and rotor, which can induce harmonics in the air-gap permeance and flux density and result in a fault-related harmonic in the machine's electrical signatures. In [13], the relationship of the bearing vibration to the stator current spectrum is given by

$$f_{brg} = | f \pm k f_v |$$ (1.2)

where

$$f_v = (N_b / 2) f_r [1 - b_d \cos(\beta) / d_p] \quad \text{BPFO}$$

$$f_v = (N_b / 2) f_r [1 + b_d \cos(\beta) / d_p] \quad \text{BPFI}$$

$$f_v = (N_b / 2) f_r [1 - (b_d \cos(\beta) / d_p)^2] \quad \text{FTF}$$

N_b is the number of balls, b_d is the ball diameter, d_p is the pitch, and β is the contact angle of the ball with race. To simulate the outer race fault, a hole is drilled on the outer race of the shaft end bearing of an induction motor. While this bearing fault is an artificial failure which does not occur in realistic cases, the bearing frequencies produced are easily found in both the vibration and current spectrums. Many studies have noted the potential of utilizing electrical signals to diagnose bearing faults. In [14], an amplitude modulation (AM) detector based on high order spectrum has been developed to identify the characteristic frequencies of outer race bearing faults. A novel method based on a fuzzy logic algorithm for incipient bearing defect detection has been presented in [15]. Wavelet packet transform (WPT) and principal component analysis (PCA) are used in pre-

7

processing the signals, and then fuzzy logic is used to distinguish the faults. Electro-discharge machining (EDM) has been used to generate localized bearing faults with fault diameters of 7, 14, and 21 mils at the inner raceway, rolling element and outer raceway, respectively. Conventional frequency analysis methods, however, do not work very well with low power machines or under non-stationary loads. To address this issue, Short Time Fourier Transform (STFT) and Gabor Spectrogram have been used to detect damaged bearings on a permanent magnet synchronous machine (PMSM) [16], although the type of bearing faults is not specified. Although the above-stated methods have been verified by experimental results, the simulated faults were artificially fabricated offline and re-assembled into the motor, which would change the system model and made the results doubtful.

External induced vibration is common in many industrial applications, while traditional developed electromechanical fault diagnosis methods in electric machines are based on the assumption of a constant radial load on the bearing. Recently [17], has addressed bearing fault detection according to the air gap variation model on an induction motor under this situation. Both vibration analysis and ESA were applied with the healthy bearing and a bearing with spheres removed. The author concluded that the current signal is a more robust indicator compared to the vibration signal, because its modulations are not affected by external excitation.

Harmonics of specific frequencies are expected to appear in the current spectrum, as a single point defect occurs in the bearing. However, when the small localized spalls have become extended and smoothed by wear, no sharp impacts will be generated

necessarily [5]. Instead, a broadband change in the current spectrum will be found. Several papers [18, 19, 20, 21] investigated applying ESA on the detection of this generalized roughness bearing defect. The authors simulated in-situ bearing deterioration by injecting high AC current externally. A model-based technique for bearing fault detection of induction motor has been proposed in [19]. The harmonics unrelated to bearing faults were filtered out and the residual was estimated via an autoregressive (AR) model. The parameters of the AR model increased as the bearing degraded. However, the proposed indicator showed poor performance with large load variations. In [18], a Wiener filter based noise cancellation technique has been employed to reduce the significant harmonics that are unrelated to bearing faults. The author in [20] extended this method by adapting it to variable load and running speed. This method has been further proved proficient in a claw-pole synchronous generator [21]. The results of vibration or current signatures under different external radial loads applied to the shaft investigated in [22], have shown that radial load has a negligible effect on the output torque, vibration, and current signals.

Several studies have focused on the detection and diagnosis of rolling element bearing faults in electrical machines based on ESA. However, the physical links between the mechanical vibrations and electrical spectrum components is still unclear [23]. Thus, there is a strong need to develop an electromechanical coupled model that can explain the physical link between vibrations and electrical signatures.

1.2.1.2 Torsional Vibration

Torque dynamic variations, torsional oscillations, and load troubles induced by internal or external factors are common factors that can be encountered during the

9

operation of electromechanical system. Under these conditions, premature failures will occur when the cumulative stress acting upon the mechanical components exceeds design limitations. For instance, in an engine-generator system, the reciprocating motion of the piston attached to the crankshaft mainly generates the torsional vibration. Should a misfire occur, which causes an imbalance in the cylinder pressures, the reciprocating frequency of the malfunctioning cylinder induces torsional vibration. Although a torque meter or strain gauge [24] is generally used to investigate the mechanical behavior of the torsional vibration, electrical signature analysis is also considered as a good alternative for mechanical monitoring.

Detecting shaft torsional vibration using stator currents has been first published in [25]. This paper has claimed that the current components at specific frequencies which are the modulation products of the power system frequency and the vibration frequency were the proper indicators of torsional vibration. A general closed form proof and experimental validation have been given for both induction and synchronous machines. In [26], harmonic analysis of stator current for Permanent Magnet Synchronous Machines (PMSM) has been presented to develop a robust real-time rotor unbalance estimation scheme for condition monitoring. Forced steady state response of torsional vibration of induction machine has been analyzed under different excitation frequencies and magnitudes [27]. In [28], a 2DOF dynamic model of a single stage gearbox, which accounts for the characterization of the pinion-wheel contact point with damping and stiffness, has been used in the electromechanical model to show the effects of external input and mesh frequency on the electromagnetic torque and stator current signature in the

induction machine. The results showed that both the current spectrum and the estimated electromagnetic torque gave significant information about system health .

1.2.2 Electromagnetic Circuit Modeling

In an electrical machine operating under ideal conditions, the air-gap between the stator and rotor is uniform and the radial magnetic forces are well balanced. Nonetheless, due to shaft deflection, inaccurate mounting of the rotor with respect to the stator, bearing wear, stator core looseness, etc., the spinning center of the shaft may not be concentric with rotor axis and stator bore axis [29]. This will disrupt the fine balance between the magnetic forces of adjacent poles, by increasing the unbalanced magnetic pull (UMP) and placing more load on the bearing. Excessive stresses resulting from the eccentricity fault can cause rubbing of the stator and rotor, eventually damaging the stator core and stator windings. When eccentricity occurs, varying inductances cause unbalanced magnetic flux within the air-gap that creates fault harmonics in the line current, which can be identified in the spectrum. Because bearing faults will cause radial motion of the shaft which varies the air-gap length and generate eccentricity, it is feasible to apply an electromagnetic model for eccentricity faults on bearing failures.
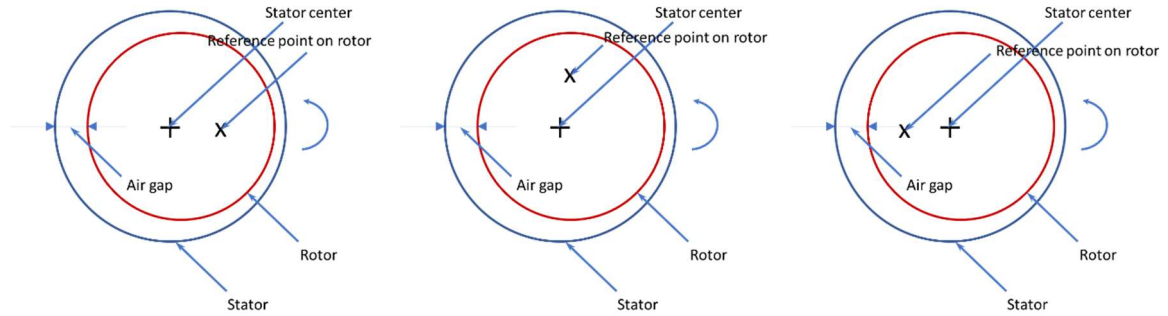
Figure 3 Static eccentricity

In general, there are two types of eccentricity fault: static eccentricity and dynamic eccentricity. Figure 3 shows the case of static eccentricity, where the rotation center is coincident with the rotor center but outside the stator bore axis. The minimum air-gap position does not change as the rotor rotates. Figure 4 shows the case of dynamic eccentricity, where the rotor spins around its own centerline and also whirl around the stator axis. The air-gap length varies as the rotor rotates. In reality, both static and dynamic eccentricities occur simultaneously, which is known as a mixed eccentricity fault [30].
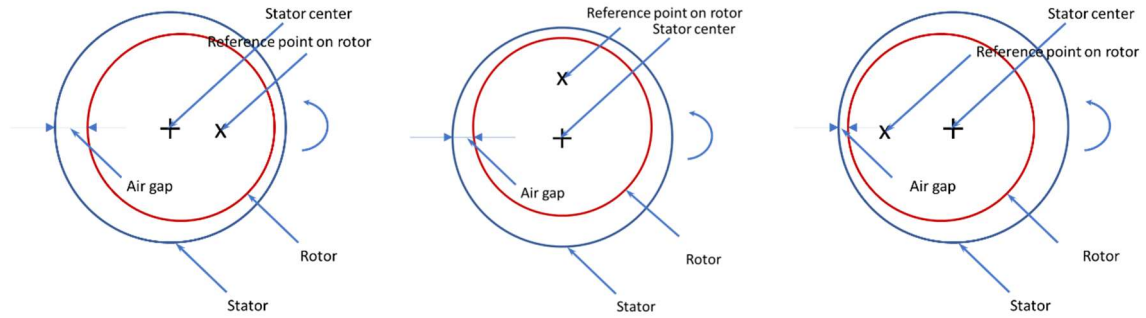
Figure 4 Dynamic eccentricity

Many studies have investigated the use of a current signal as the medium to detect air-gap eccentricity faults. Some studies have focused on the detection of fault-related signatures in the current signals, while others have focused on modeling and simulating faults.

The winding function approach (WFA) is the most widely used method because it requires less computation complexity and it is comparably accurate. In [31] [32], the sidebands of either the slot frequencies or fundamental have been used to detect air-gap eccentricity. However, the underlying theory behind had not yet been established. Toliyat [33] was the first to use the winding function approach (WFA) to study the performance of induction motor with SE fault. Unlike a traditional lumped model using only the fundamentals, WFA accounts for the space harmonics induced by non-sinusoidal distributed winding, therefore making it possible to simulate motor performance with SE. The simulation results closely agreed with the experiments.

An improved analytical approach known as the modified winding function approach (MWFA) has been proposed in [34] [35]. The simulation as well as experiments

of a single phase and a three-phase induction machine under mixed eccentricity faults demonstrated the possibility that monitoring slot harmonics in the stator current to detect eccentricity faults. MWFA has been further improved by accounting for the skewing of the rotor bars and the resulting linear rise in the MMF across the slots [36]. In [37], a more practical case, the axial non-uniformity of air-gap known as inclined eccentricity has been reported. In [38], startup transient simulations have been performed on an induction motor with mixed rotor eccentricity fault using Time-Stepping Finite Element (TSFE) approach. In the simulation, the applied voltage was used as an input. The results showed that the sidebands of fundamental were well indexed for detecting mixed eccentricity.

Since the 1990s, the needs to improve energy efficiency and the advancements in power electronics have prompted researchers to turn their attention to synchronous machines. For example, in [39], a MWFA based model has been created to study DE in a salient pole synchronous machine, where the 17th and 19th harmonics have been reported as a good indicator of DE fault. By incorporating the open slot effect, a more accurate model has been reported in [40]. Rotor faults in turbo-generators have been studied in [41] using transient FE analysis. The response of a two pole turbo-generator to DE fault has been analyzed in both time and frequency domain. Frequency domain signatures in the no-load voltage spectrum of the generator were found to identify the existence of rotor fault, even though fault discrimination could not be achieved.

The different effects of SE and DE on the external electric variables of an on-board ship salient-pole synchronous generator have been presented in [42]. Unlike monitoring particular fault-related harmonics, the increment of a no-load EMF space vector has been

14

investigated by 3D FEM as a useful tool to detect eccentricity faults. A different oval shaped EMF space vector was found with SE but not DE, proving that the shape of the loci can be used to distinguish the type of eccentricity. However, no discussion regarding the effect of ME was reported. In a later publication [43], compared comparison of an MWFA-based model with an improved air-gap function and the 3D FEM model has found similar results; the author concluded that no-load voltage harmonics also showed good dependence on level and type of eccentricity. In [44], another comparison between MWFA and FEM on a 2 kW, 3 phases, 60Hz, star connected salient pole synchronous motor, where the fault related harmonics have been found in both models, has been verified by experimental results. In [45] and [46], based on a MWFA model, general criteria to predict the fault-related voltage harmonics for no-load synchronous generator affected by static eccentricity have been carried out, and followed by the use of a 15kVA four pole fractional-slot synchronous generator for experimental validation. The SE was attached by an innovative flange with the capability of adjusting amplitude and direction of both SE and DE. The influences of different excitation schema, AC and DC exciting currents, have been discussed. SE has been found to introduce a double fundamental frequency ripple in the field current. While the experimental results confirmed the theoretical prediction, they showed that linear models useful for the simplest cases were not sufficient in providing precise quantitative results when a mixed type eccentricity fault occurs in a real machine.

1.2.3 Bearing Modeling

In studying bearing faults and fault mechanisms, the underlying physics and behavior of bearing systems should be well interpreted. This understanding is achieved by reviewing and developing bearing models, and understanding how experiments can validate the modeling methods.

References [47] [48] have provided a solid foundation for the modeling of bearings by developing bearing element stiffness, deflections, damping, constraints, forces, moments and general governing equations of motion. All of the derivations were based on fundamental theories ranging from Hertzian contact theory to Lagrangian dynamical derivations.

Gupta [49] has provided a detailed formulation of specific bearing dynamical behavior which was previously neglected, such as ball-race interactions, ball-cage interactions, churning and drag losses, and lubrication effects. In [50], Gupta (1985) refined his model and validated it experimentally. Both the simulation and the experiments indicated a certain critical shaft speed at which the cage begins to whirl. A more detailed analysis has been presented by Datta and Farhang [51], which treated each element in the bearing as a nonlinear spring.

To model the bearing defects, McFadden [52] has taken a different approach by using impulse train to model the vibration produced by the impact of a bearing element with a single point defect. A multiplying factor on the impulse function was applied to represent the level of severity of the defect. Later, the author extended the model to adapt for multiple point defects [53]. An experiment was also performed to verify the model.

In [12], to study the extended fault located at the inner/outer race of rolling element bearings, a combined dynamic model for gears and bearings has been proposed to obtain a better understanding of the physical link between the two components. The extended faults do not necessarily produce high frequency impact responses, but do modulate the gear-mesh signals. Gaussian noise filtered by low pass filter was generated to simulate the rough surface. The simulation results mostly agreed well in with the experimental data, showing that the extended fault could be clearly detected after removing the gear contribution and comparing the cyclic spectra.

In 2015, Linkai Niu et al. [54] have carried out a systematic study of ball passing frequencies (BPFs). Localized surface defects were modeled by considering the ball size, the clearance due to material absence, and contact force directions. The study showed that several elements, including the shaft speed, external loads, friction coefficient, raceway groove curvature, initial contact angle, and defect sizes, affected the BPFs. The 1-2% variation of the spacing between impulses caused by a defective ball bearing reported in previous studies, was only satisfied when the skidding effect in the bearing is small. Two experiments were performed to verify the findings.

In 2015, an extensive review for the vibration modelling of rolling element bearings with localized and extended defects has been undertaken by Sarabjeet et al. [55]. The authors also discussed the benefits and limitations of algorithms for estimating the size of bearing defects. They recommended conducting a full parametric model including load, rotational speed, clearance, and various defect types in the future.

1.3 Research Objective

Over the years, a great number of works have been devoted to detection of mechanical faults including rolling element bearing defects and torsional defects in electrical machines based on ESA. It has been discovered that these faults can affect either stator to rotor air-gap distribution or running speed of the machine, which can be reflected in the signature of electrical signal. In addition, many talented works have been contributed to the understanding of the dynamics of rolling element bearing while a localized or a distributed fault occurs. However, the physic link between the mechanical signature and the electrical signature are still not clear enough. The objectives of this research can be listed as follows:

The published literature concerning the use of ESA to detect mechanical faults including rolling element bearing defects and torsional defects in electrical machines has determined that the faults, which can affect either stator to rotor air-gap distribution or running speeds of the machine, can be reflected in the electrical signature. The physical link between the mechanical signature and the electrical signature, however, has not been determined conclusively. Therefore, the objectives of this research are:

- To include both rolling element bearing dynamics modeling and synchronous generator modeling into a new comprehensive model capable of describing the transmission between bearing faults and electrical signal variations

- To analyze the impact of a synchronous generator with a bearing defect on different components in order to guide the development of an ESA-based bearing fault detection schema

- To conduct an in situ experiment and analyze the electrical signatures caused by the general roughness bearing defects to gain practical insights into the use of electrical measurements as a bearing fault detection source

1.3.1 Proposed Approach

The proposed scope of this dissertation will include synchronous generator modeling, bearing modeling, multi-body dynamics modeling for drive trains, and model verification. The first step is to model an electrical machine with the capability of introducing mechanical defects. As mentioned in the literature review, WFAs are widely used in modeling internal faults including short windings, broken rotor bars, eccentricity, etc. Compared with the traditional lumped model, WFAs account for all of the space harmonics and interpret the influences from the variation of air-gap between stator and rotor. A promising synchronous generator model based on MWFA will be built to simulate various rotor eccentricity scenarios. A more accurate FEM model created with the commercial FE package JMAG will be used to validate the model.

The majority of the literature on eccentricity faults assumes that the rotor rotates along a round circle orbit synchronized with the shaft spinning speed. However, it is not the case for realistic machines. As shown in [56], the measured shaft orbits are irregular and altered depending on load conditions. To illustrate the practical air-gap variations induced by bearing faults, a new rolling element bearing model will include a flexible, physically based introduction of mechanical faults into the system. The proposed model will provide a quantified system response to a comprehensive set of typical bearing failures.

The electromagnetic circuit model and the mechanical models including bearing defects will be coupled to explore the electrical signatures induced by the faults introduced. ESA will be carried out using the simulated data obtained from the inter-coupled synchronous machine system and the experimental data from the in-situ bearing deterioration experiment. The results will be compared to the trend of vibration signatures.

1.3.2 Anticipated Contribution

Reliable operations of synchronous machines are critical in power generation systems. Moreover, there is a growing need for inexpensive, non-intrusive, easy-to-use diagnostic technique. Although various ESA-based algorithms have been developed and verified in the laboratory, a clear theoretical understanding of the physical link between the mechanical signature and the electrical signature has not been determined. The proposed inter-coupled simulation model will bridge the gap between electromagnetic circuit modeling of electrical systems and the dynamic modeling of mechanical system. The research will make the following contributions:

- A new model combining a detailed bearing model in a synchronous generator will allow introducing bearing faults

- Comprehensive analysis of synchronous generator voltages and currents under bearing defects that induce air-gap variation

- A useful tool for analyzing the performance of ESA-based diagnosis algorithms in a controlled environment

CHAPTER II

MODELING SALIENT POLE SYNCHRONOUS MACHINES WITH

ECCENTRICITY FAULTS

In the last few years, more and more researchers have shown great interests in the condition monitoring of synchronous AC machines, on-line and/or off-line, because of enormous cost on parts replacement and production lost. If properly used, condition monitoring (CM), can extend the lifecycles of various types of ac machines. CM is based on modeling the machine faults that are subsequently used to analyze the full effects on a machine's behavior. To analyze the behavior of synchronous machines under faulty conditions, developing simple models for the machines which can take the faults into account is very important.

In this chapter, a model based on WFA that can simulate synchronous machines under rotor eccentricity faults is built firstly. Secondly, the effects of dynamic and static eccentricity are studied using the developed model on the self-magnetizing and mutual inductances of a salient pole synchronous machine (SPSM). Thirdly, a finite element model built in a commercial software, which is widely employed in the industry, is used to validate the WFA model. Lastly, specific harmonic components in the current signatures are discussed under different eccentricity level in both WFA and FEM models.

2.1 Winding Function Approach

Conventional modeling methods of electrical machines do not take the winding configuration and geometry of the machine into consideration, which results in the incapability of simulating the space harmonics changes induced by various fault conditions such as broken bars, short turns, and rotor eccentricities. Although the novel method FEM provides precise modeling, its application is complicated and the computation cost is huge especially for the transient analysis of electrical machines with asymmetry in the motor body [57] [58]. WFA is based on the geometry and the winding distribution of the machine, which makes it possible to analyze the machine's behavior under winding and rotor position variations due to faulty conditions [57]. Because of its moderate accuracy and much less computation effort requirement, this method has been broadly applied to analyze broken rotor bars [58], fault condition in stator windings [61], eccentricities in induction and synchronous machines [35] [44]. In a recent publication [62], it was extended for radial and axial non-uniform air gap in SPSMs.

Calculating the machine inductances accurately is the most important step to get a validity model, which can improve the accuracy of the analysis of electrical machines. In [63] an analytical equation of the air gap for an eccentric SPSM was presented. The turns function and the inverse air-gap function are expanded into Fourier series. The inductances are calculated with the simplified analytical solutions. However, the rotor motion is assumed to be a synchronous whirling under eccentricity faults. In this research, air gap function is not only a function of rotating angle but also a function of rotor offsets.

2.1.1 Winding Function
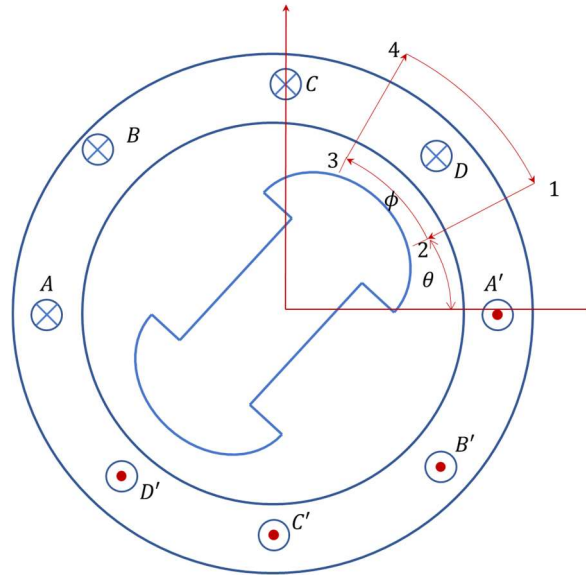
Figure 5 Winding Function of an elementary SPSM

The basic idea of winding function approach has been introduced in [64], and the derivations below is following the book. An elementary two-pole salient pole synchronous machine (SPSM) with four concentrated stator coils A,B,C and D is shown in Figure 5. Each stator coil is configured to full pitch. The current which goes into the paper is denoted with a cross "×" and is defined as positive. The current which goes out of the paper is denoted with a dot "●" and defined as negative. A reference angular position is selected as $\theta = 0$. The path 12 is taken across the gap from stator to rotor at θ and the path 34 returns across the gap at $\theta + \phi$.

The same current i is carried in all coils of the windings enclosed by the closed path 1-2-3-4-1. According to Ampere's Law, the following relation can be obtained considering the closed path 1-2-3-4-1 illustrated in Figure 5:

$$\oint_{12341} \vec{H} \cdot \vec{dl} = n(\varphi, \theta)i,$$ (2. 1)

where H is the magnetic field intensity and dl is defined to be along the closed path 1-2-3-4-1. This equation states that the circulation of magnetic field intensity in free space around any closed path is equal to the total current enclosed by the path. The function $n(\varphi, \theta)$, which expresses the number of turns surrounded by the closed path 1-2-3-4-1, is called the turns function. It is a function of φ for stationary coils in the stator. For the coils of the rotating rotor, it is a function of φ and rotor position θ. Turns are considered as positive, if the current they carry goes into the page. Otherwise turns are considered as negative. The turns function $n(\varphi, \theta)$ for the arbitrary windings is shown in Figure 6, assuming that each side of the coil has N turns.

When the closed path is split into four components, the magnetomotive force (MMF) drops in the closed path can be written as:

$$MMF_{12} + MMF_{23} + MMF_{34} + MMF_{41} = n(\varphi, \theta)i$$ (2. 2)
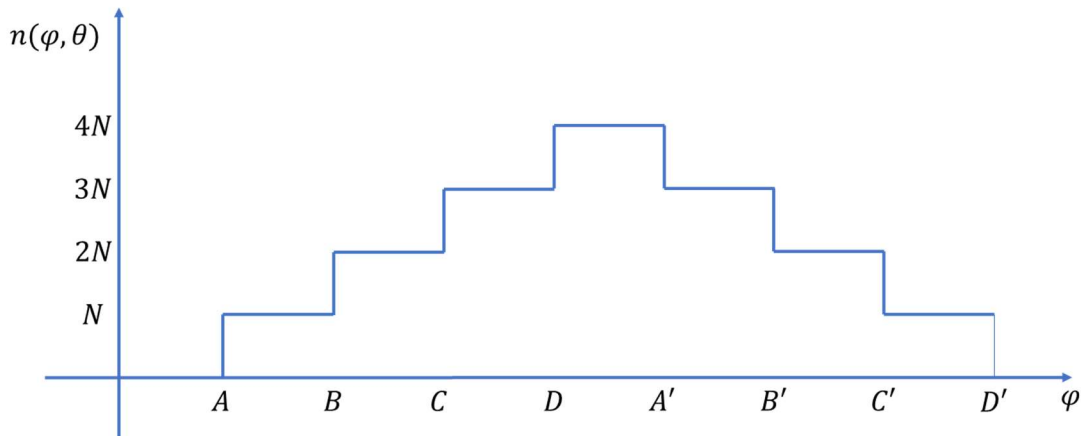

Figure 6 Turns function for the winding distributions

24

Because the magnetic permeability of the stator iron is much larger than that of the air gap, the iron permeability is assumed to be infinite by ignoring the saturation effects. Therefore, the MMF drops MMF_{23} and MMF_{41} can be neglected and (2. 2)reduces to:

$$MMF_{12}(0,\theta) + MMF_{34}(\theta,\varphi) = n(\varphi,\theta)i. \tag{2. 3}$$

By Gauss's law for magnetic fields:

$$\oint_S B \cdot dS = 0, \tag{2. 4}$$

where B represents the magnetic flux density and S represents the surface of an closed cylindrical shape. This equation states that there are no magnetic flow sources, and the magnetic flux lines always close upon themselves, i.e., the magnetic flux through any closed surface is zero [57]. Since all flux is assumed to pass through the air gap and the iron permeability is infinite, (2. 4) can be written as:

$$\oint_S B \cdot dS = \int_0^{2\pi}\int_0^L \mu_0 r_s H(\varphi,\theta)dld\varphi = \mu_0 r_s \int_0^{2\pi} H(\varphi,\theta)d\varphi = 0 \tag{2. 5}$$

where μ_0 is the free space permeability, r_s is the stator inner radius, L is the effective axial stack length of the machine. Since B does not vary with respect to the axial length, after eliminating the constant components, (2. 6) can be written as:

$$\int_0^{2\pi} H(\varphi,\theta)d\varphi = \int_0^{2\pi} \frac{MMF(\varphi,\theta)}{g(\varphi,\theta,x,y)}d\varphi = 0 \tag{2. 6}$$

Because MMF can be expressed as the product of the magnetizing force and the flux radial length, substituting equation (2. 3) into (2. 6) yields:

$$\int_0^{2\pi} \frac{MMF_{12}(0,\theta) + MMF_{34}(\varphi,\theta)}{g(\varphi,\theta,x,y)} d\varphi = \int_0^{2\pi} \frac{n(\varphi,\theta)}{g(\varphi,\theta,x,y)} i d\varphi \qquad (2. 7)$$

Substitute the relation of (2. 6) into (2. 7). The equation above can be reduced to:

$$\int_0^{2\pi} \frac{MMF_{12}(0,\theta)}{g(\varphi,\theta,x,y)} + \frac{MMF_{34}(\varphi,\theta)}{g(\varphi,\theta,x,y)} d\varphi =$$

$$MMF_{12}(0,\theta) \int_0^{2\pi} g(\varphi,\theta,x,y)^{-1} d\varphi = \int_0^{2\pi} \frac{n(\varphi,\theta)}{g(\varphi,\theta,x,y)} i d\varphi \qquad (2. 8)$$

Therefore, $MMF_{12}(0,\theta)$ can be expressed as:

$$MMF_{12}(0,\theta) = \int_0^{2\pi} \frac{n(\varphi,\theta)}{g(\varphi,\theta,x,y)} i d\varphi \left/ \int_0^{2\pi} g^{-1}(\varphi,\theta,x,y) \, d\varphi \right. \qquad (2. 9)$$

By substituting (2. 9) into (2. 3), $MMF_{34}(\varphi,\theta)$ can be solved as:

$$MMF_{34}(\varphi,\theta) = (n(\varphi,\theta) - \frac{1}{\int_0^{2\pi} g^{-1}(\varphi,\theta,x,y) d\varphi} \int_0^{2\pi} n(\varphi,\theta) g^{-1}(\varphi,\theta,x,y) d\varphi) i \qquad (2.10)$$

Therefore, the modified winding function $M(\varphi,\theta)$ [39] with non-symmetric air-gap can be defined by:

$$M(\varphi,\theta) = n(\varphi,\theta) - \frac{1}{\int_0^{2\pi} g^{-1}(\varphi,\theta,x,y)d\varphi} \int_0^{2\pi} n(\varphi,\theta)g^{-1}(\varphi,\theta,x,y)d\varphi \qquad (2.\ 11)$$

The general form of the modified winding function is defined in (2. 11). It is applicable to any given winding configurations or non-symmetric models.

2.1.2 Eccentricity Modeling

Flaws in the manufacturing process, shaft misalignment, unbalanced rotor, and vibration excited by connected mechanical components, all these factors may result in eccentricity fault in an electrical machine. As shown in Figure 7, there are three types of air-gap eccentricity [58], which are static eccentricity (SE), dynamic eccentricity (DE) and mixed eccentricity (ME). In the case of SE, the rotor centroid and the center of rotation are identical, but they do not coincide with stator centroid. The minimal air-gap location is fixed with respect to the stator. Dynamic eccentricity occurs when the rotor centroid is off to the center of rotation and the stator centroid coincides with the center of rotation. The minimal air-gap location moves while the rotor rotates. When both SE and DE exist, ME is generated. The rotor centroid, the center of rotation, and the stator centroid are not coincided with each other.
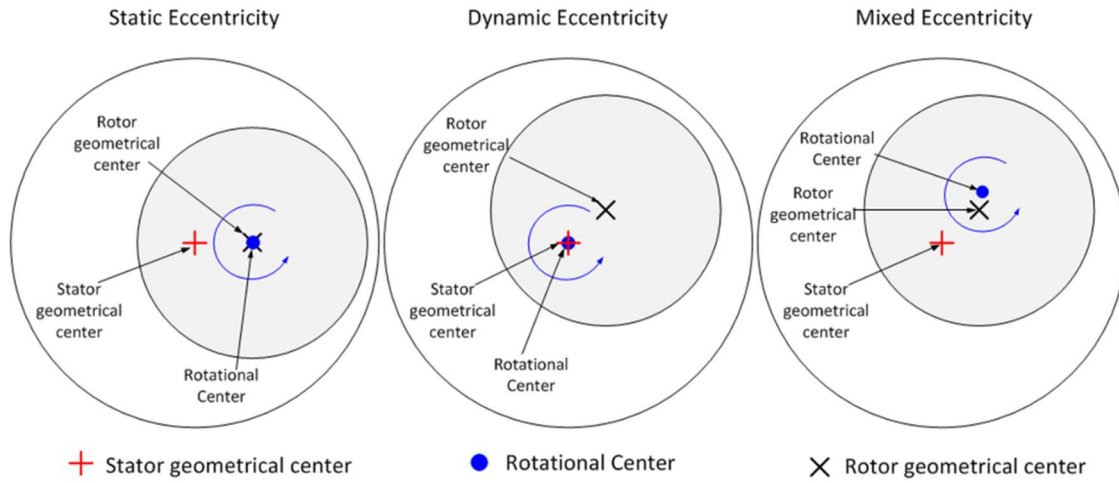
Figure 7 The three eccentricities in a synchronous machine. SE, DE, ME

Apparently, compared to the symmetrical conditions, the winding functions of the stator windings and rotor winding of the machine do not make any difference in non-uniformity conditions. Nonetheless, the functions of the air-gap length and the mean radius will become different in the symmetrical case. In the ME case, the air-gap and mean radius functions are illustrated by:

$$g_e(\phi,\theta,x,y) = g(\phi,\theta)(1 - \delta_s \cos(\phi - \phi_s) - \delta_d\cos(\phi - \phi_s - \theta))$$

(2. 12)

where $g_e(\phi,\theta)$ is the airgap function with eccentricity, $g(\phi,\theta)$ is the airgap function for a healthy machine, θ is the rotor position angle in stator reference, ϕ is the angle in stator reference frame, (x,y) are the rotor offsets on vertical and horizontal direction, ϕ_s is the angle by which the rotation and stator centers are off, and δ_s and δ_d are the static and dynamic relative eccentricity levels which are also functions of (x,y), respectively.

28

2.1.3 Calculation of Inductances

Calculation of inductances is based upon three assumptions:

- Slotted stator effects are negligible,

- Magnetic hysteresis is negligible, and

- The iron core is not saturated.

The MMF drop in the iron core is neglectable, because the relative permeability of the iron is assumed to be infinity in the model. The MMF distribution can be simply calculated using the winding function defined in (2. 11) with the current flowing in the coils.

Let's assume the modified winding function of winding A is $M_A(\varphi, \theta, x, y)$, and winding B has a turns function $n_B(\varphi, \theta)$. According to [64], the flux crossing the air-gap at any position by winding A is given by:

$$d\Phi = MMF_A(\varphi, \theta) \mu_0 r_s L \frac{d\varphi}{g(\varphi, \theta, x, y)} \tag{2. 13}$$

The total flux linkage for winding B due to current in winding A can be defined as:

$$
\begin{aligned}
\lambda_{BA} &= \mu_0 r L \sum_{k=1}^{q_i} \int_0^{2\pi} n_{Bk}(\varphi, \theta) F_A(\varphi, \theta) \frac{d\varphi}{g(\varphi, \theta, x, y)} \\
&= \mu_0 r L \int_0^{2\pi} n_B(\varphi, \theta) F_A(\varphi, \theta) \frac{d\varphi}{g(\varphi, \theta, x, y)}
\end{aligned}
\tag{2. 14}
$$

where $n_B(\varphi, \theta) = \sum_{k=1}^{q_i} n_{Bk}(\varphi, \theta)$ is the turns function for winding B under the assumption that the q_i coils are connected in series. Then the mutual inductance L_{BA} can be calculated

by:

$$L_{BA} = \frac{\lambda_{BA}}{i_A} = \frac{\mu_0 rL}{i_A} \int_0^{2\pi} n_B(\varphi, \theta) F_A(\varphi, \theta) \frac{d\varphi}{g(\varphi, \theta, x, y)} \qquad (2.\ 15)$$

By substituting $F_A(\varphi, \theta) = M_A(\varphi, \theta) i_A$ into (2. 15),

$$L_{BA} = \frac{\lambda_{BA}}{i_A} = \mu_0 rL \int_0^{2\pi} n_B(\varphi, \theta) M_A(\varphi, \theta) \frac{d\varphi}{g(\varphi, \theta, x, y)} \qquad (2.\ 16)$$

Using the same procedure, the self-magnetizing inductance of winding A can be obtained as:

$$L_{AA} = \mu_0 rL \int_0^{2\pi} n_A(\varphi, \theta) M_A(\varphi, \theta) \frac{d\varphi}{g(\varphi, \theta, x, y)} \qquad (2.\ 17)$$

Equations (2. 16) and (2. 17) can be utilized to calculate any electrical machine mutual and magnetizing inductances even when the machine is experiencing failures such as rotor eccentricity and shorted rotor field. It is because the turns function $n(\varphi, \theta)$ and the modified winding function $M(\varphi, \theta)$ are calculated in their general forms to include even the failures and asymmetries, which can be associated to either stator or rotor.

2.2 Electrical Circuit Model for Synchronous Machines

2.2.1 Stator and Field Equations

All of the inductances for solving the machine equations can be calculated using the modified winding function approach (MWFA) described above. Once the inductances of the synchronous machine are obtained, the dynamic response of the system can be computed.

The voltage equations for the stator circuits of a typical 3 phase synchronous machines can be written as:

$$V_{abcs} = R_s i_{abcs} + \frac{d\Lambda_s}{dt}$$ (2. 18)

By the definition of inductance, the stator flux linkages are given by:

$$\Lambda_s = L_s i_{abcs} + L_{sf} i_f$$

V_{abcs} and i_{abcs} , which are the stator voltage vector and current vector, respectively, can be written as:

$$V_{abcs} = \begin{bmatrix} v_{as} \\ v_{bs} \\ v_{cs} \end{bmatrix}, i_{abcs} = \begin{bmatrix} i_{as} \\ i_{bs} \\ i_{cs} \end{bmatrix}.$$ (2. 19)

Stator inductance matrix L_s is a symmetric 3 by 3 matrix that can be written as:

$$L_s = \begin{bmatrix} L_{aa}(x,y,\theta) + l_s & L_{ab}(x,y,\theta) & L_{ac}(x,y,\theta) \\ L_{ba}(x,y,\theta) & L_{bb}(x,y,\theta) + l_s & L_{bc}(x,y,\theta) \\ L_{ca}(x,y,\theta) & L_{cb}(x,y,\theta) & L_{cc}(x,y,\theta) + l_s \end{bmatrix}$$ (2. 20)

where L_{ii} is the self-inductance of phase i, L_{ij} is the mutual inductance between phase i and j, and l_s is the leakage inductance of the stator winding.

L_{sf} is a 3 by 1 matrix comprised of the mutual inductances between the stator windings and the field windings that can be written as:

$$L_{sf} = \begin{bmatrix} L_{af}(x,y,\theta) \\ L_{bf}(x,y,\theta) \\ L_{cf}(x,y,\theta) \end{bmatrix}$$ (2. 21)

The self-inductances and mutual inductances are calculated by the rotor offset (x,y) and the rotating angle θ.

The stator resistance matrix R_s consists of the stator resistance. The resistance in each stator winding identical to r_s is given by:

$$R_S = \begin{bmatrix} r_s & 0 & 0 \\ 0 & r_s & 0 \\ 0 & 0 & r_s \end{bmatrix} \tag{2.22}$$

The voltage equation of the field winding is given by:

$$V_f = R_f i_f + \frac{d\Lambda_f}{dt}$$
$$\Lambda_f = L_{fs} i_{abcs} + L_f i_f \tag{2.23}$$

where R_f is the field winding resistance, i_f is the field current, $L_{fs} = L_{sf}^T$ is the matrix of the mutual inductances between the field and the stator windings, and L_f is the self-inductance of the field winding.

2.2.2 Mechanical Coupling with the Torque

Assume the rotor of the synchronous machine is a simple disk with moment of inertia J. The equation of motion is given by:

$$T_e - T_L = J\ddot{\theta} + B\dot{\theta} \tag{2.24}$$

where T_e is the electromagnetic torque, T_L is the load torque, B is the rotor bearing damping, and θ is the rotor position.

According to the co-energy method, the electromagnetic torque can be calculated by

$$T_e = \frac{dW_{CO}}{d\theta} \tag{2.25}$$

In a linear magnetic system, the co-energy is equal to the magnetic energy stored in all inductances. Thus, when the damping winding is ignored, the co-energy can be expressed as:

$$W_{co} = \frac{1}{2}(I_s^T L_s I_s + I_f^T L_f I_f + I_f^T L_{fs} I_s + I_s^T L_{sf} I_f) \qquad (2.26)$$

Substitute it back to the torque equation, we have:

$$T_e = \frac{1}{2}(I_s^T \frac{\partial L_s}{\partial \theta} I_s + I_f^T \frac{\partial L_f}{\partial \theta} I_f + 2I_f^T \frac{\partial L_{fs}}{\partial \theta} I_s) \qquad (2.27)$$

2.2.3 Assembling the Equations for the Dynamic Model

To solve for the unknown variables, a set of differential equations, including the stator and field voltage equations and the equations of motion for the rotor given above is assembled. For the motor, the unknown variables are the currents. When the electrical machine runs as a generator, the stator voltages are also unknown. In addition to the unknown voltages, the electromagnetic torque becomes the load torque, and the torque applied on the shaft becomes the input torque for the mechanical system. The assembled set of differential equations is:

$$\frac{d\Lambda}{dt} = V - RI$$

$$\frac{d\omega}{dt} = \frac{1}{J}(T_e - T_L) \qquad (2.28)$$

$$\frac{d\theta}{dt} = \omega$$

$\Lambda = LI$, then the first differential equation becomes:

$$\frac{d\Lambda}{dt} = \frac{dLI}{dt} = \frac{dL}{dt}I + L\frac{dI}{dt} = V - RI \qquad (2.29)$$

Inductance matrix L is a function of θ, x, y; therefore:

33

$$\frac{dL}{dt} = \frac{\partial \theta}{\partial t}\frac{\partial L}{\partial \theta} + \frac{\partial x}{\partial t}\frac{\partial L}{\partial x} + \frac{\partial y}{\partial t}\frac{\partial L}{\partial y} = \omega\frac{\partial L}{\partial \theta} + u\frac{\partial L}{\partial x} + v\frac{\partial L}{\partial y}$$

Substitute it back to (2. 28), the final expression of the differential equations used to find the unknown currents becomes:

$$\frac{dI}{dt} = L^{-1}(V - RI - \omega\frac{\partial L}{\partial \theta} - u\frac{\partial L}{\partial x} - v\frac{\partial L}{\partial y})$$

$$\frac{d\omega}{dt} = \frac{1}{J}(T_e - T_L) \tag{2. 30}$$

$$\frac{d\theta}{dt} = \omega$$

The vectors and matrices used in the equations are defined as:

$$I = [I_{abcs} \quad I_f]^T$$

$$V = [V_{abcs} \quad V_f]^T$$

$$R = \begin{bmatrix} R_s & 0 \\ 0 & R_f \end{bmatrix} \tag{2. 31}$$

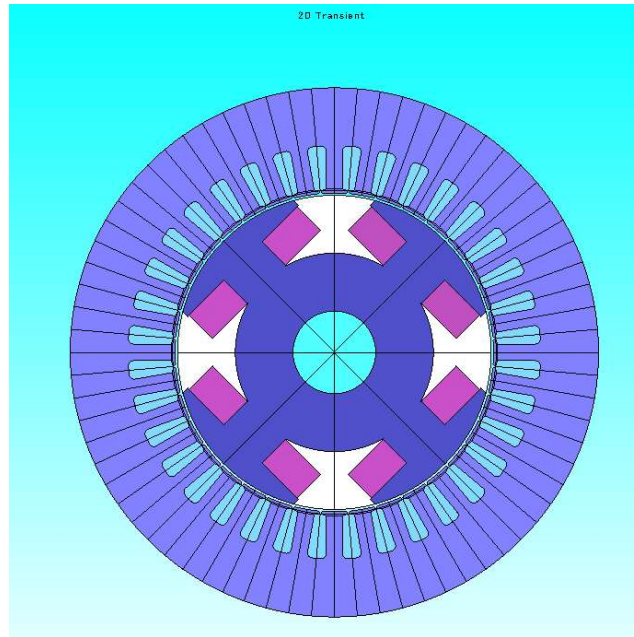$$L = \begin{bmatrix} L_s & L_{sf} \\ L_{fs} & L_f \end{bmatrix}$$

Figure 8 Cross section model of the SPSM

To validate the proposed method, a 13kVA, 3 phases, 4 poles, 60Hz SPSM is modeled using both WFA and FEM. The main parameters are listed in Table **1**. The commercial software JMAG is used to create the FEM model. The cross section of the modeled machine is shown in Figure **8**. The next sections describe a comparison of the inductances calculated by both methods followed by a comparison of the voltage/current spectrums in both open circuit cases and loaded cases with different dynamic eccentricity.

Table 1 Main Parameters of the SPSM

Name	Symbol	Value
Synchronous speed	w_s	1800rpm
Phase	m	3
Pole pairs	p	2
Rated power	P_{rate}	13kVA
Number of stator slots	N_s	36
Number of slot layers	q	2
Number of parallel circuits	C	1
Number of turns per phase connected in series	N_{ph}	124
Coil span	$Cspan$	6
Number of turns per pole of field winding	N_r	76
Minimum air gap	g_0	1.4mm
Maximum air gap	g_m	11.2mm
Stator stacking length	l_s	80mm
Pole arc	p_{arc}	120°
Stator resistance per phase	R_s	1.02ohm
Field resistance	R_f	0.48ohm

2.3.1 Calculated Inductances

The accuracy of the electrical circuit model is determined by how well the inductances are calculated. Figure **9** depicts the self-inductances and mutual inductances over 180 degrees of rotation angle as computed by both WFM and FEM. The rotor is moved away from its center 0.7mm (50% of the minimal air-gap) toward the x-axis direction. The shapes of $L_{aa}, L_{ab},$ and L_{ac} are identical, but the phases are shifted by $\pi/6$. In addition, L_{aa} is levitated by about 0.2H because of the eccentricity along the x-

36

axis. As expected, the shapes of inductances calculated by WFM are smoother than those calculated by FEM, because simplifications are made to the magnetic circuit in WFM.
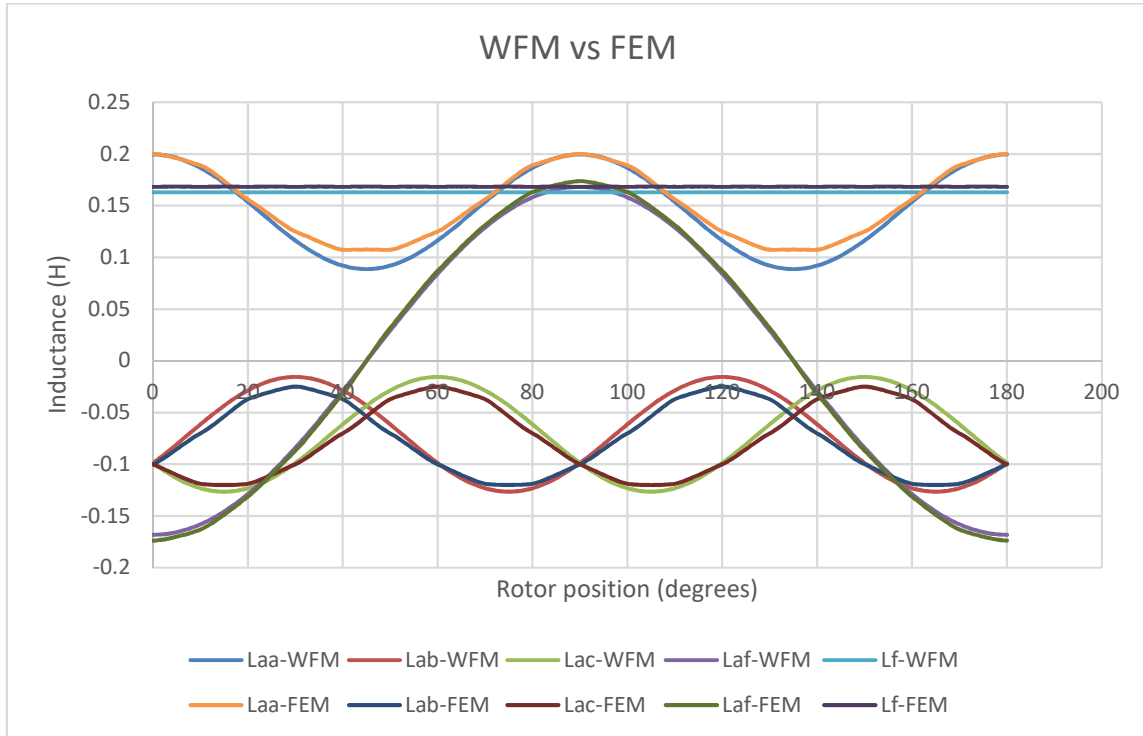

Figure 9 Inductances over different rotating angles

When the dynamic eccentricity is changed from 0% to 50% for the modeled SPSM, the computed inductances are compared as shown in Figure 10. Note that the absolute values of the inductances become larger with the increase of the eccentricity, and the inductances increase nonlinearly with the eccentricity changes. The inductances' errors between the two modeling methods are shown in Table 2. Because the purpose is to investigate the influence of airgap variations on electrical signals, we are trying to find a balance point between accuracy and computational cost. According to the comparison, the errors of the field-related inductances are much higher than the stator-related

37

inductances, which are still acceptable when they match the curve pattern of the inductances in FEM.
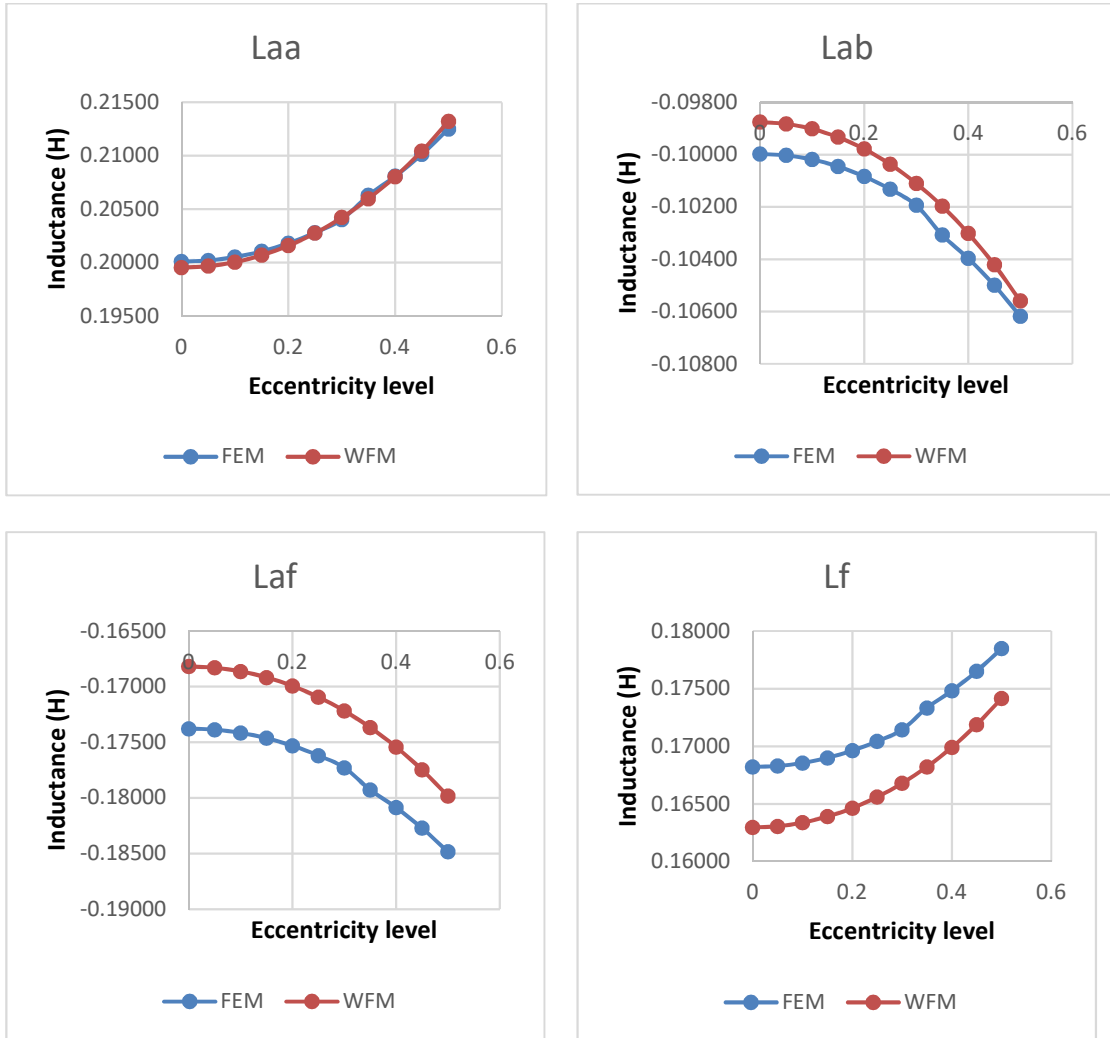

Figure 10 Inductances vs eccentricity

Table 2 Errors between the inductances computed by WFM and FEM

Offset	0	0.05	0.1	0.15	0.2	0.25	0.3	0.35	0.4	0.45	0.5
Laa	-0.3%	-0.3%	-0.2%	-0.2%	-0.1%	0.0%	0.1%	-0.2%	0.0%	0.1%	0.3%
Lab	-1.2%	-1.2%	-1.2%	-1.1%	-1.0%	-0.9%	-0.8%	-1.1%	-0.9%	-0.7%	-0.6%
Lac	-1.2%	-1.2%	-1.2%	-1.1%	-1.0%	-0.9%	-0.8%	-1.1%	-0.9%	-0.7%	-0.6%
Laf	-3.2%	-3.2%	-3.2%	-3.1%	-3.1%	-3.0%	-2.9%	-3.1%	-3.0%	-2.9%	-2.7%
Lf	-3.1%	-3.1%	-3.1%	-3.0%	-2.9%	-2.8%	-2.7%	-2.9%	-2.8%	-2.6%	-2.4%

2.3.2 Simulated Results

The SPSM behavior is simulated during a steady state condition. In this section, the simulation results of open circuit voltage waveforms and loaded current waveforms with DC field current source are presented and the spectrums with different eccentricity levels are compared.
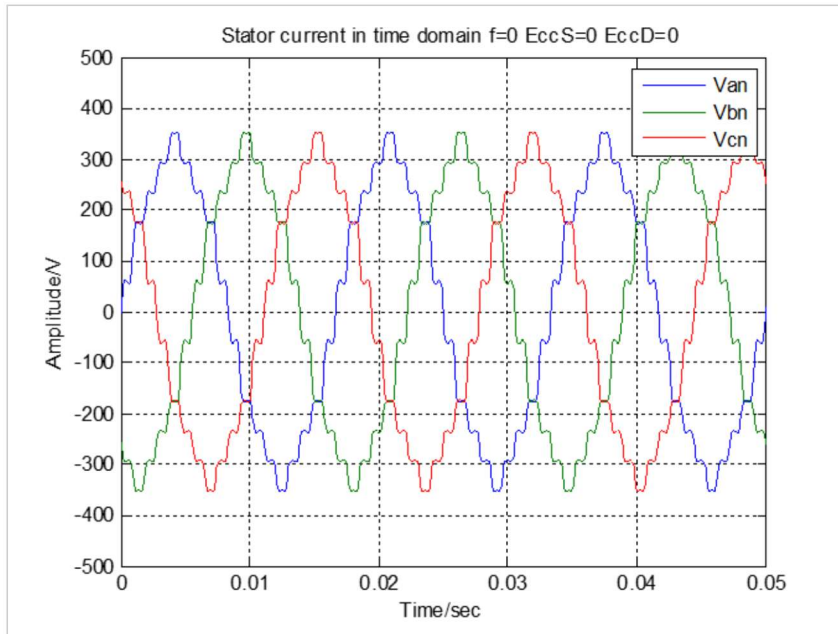
2.3.2.1 Open Circuit

Figure 11 Voltage waveforms for the open circuit case

The three phase voltages $V_a, V_b,$ and V_c at the steady state for the open circuit configuration are shown in Figure 11. Since the circuit is open, the terminal voltages are the same as the back-EMF of the circuit. Note that the voltage waveforms are more like a staircase than a sinusoidal shape, because the shape of back-EMF is determined by the

winding configuration. The staircase waveform represents a full pitch setup of the winding.

Spectrums of the voltages with different dynamic eccentricities are shown in Figure 12. The simulation results from the WFA-based model with static eccentricity levels 0, and 50% are shown in Figure 12 (a), and (b), respectively, and the results for the FEM model are shown in Figure 12 (c) and (d)respectively. Similarly, the results for dynamic eccentricity are shown in Figure 13. For most of the harmonics listed in Table 3, implementing SE and DE increases the induced voltage harmonics. The 19th harmonics obtained with FEM decreases while eccentricity is applied, which may due to the low resolution caused by short simulation period in FEM. The difference between the signatures of SE and DE is that 3rd harmonics is generated in the case of SE. It is because that the air-gap variation for each winding is not identical during one rotate of the rotor.

Table 3 Relative increase of voltage harmonics due to 50% SE and DE – no load

Order of harmonics		3rd	5th	7th	11th	13th	17th	19th
WFA	SE	7833%	15%	15%	15%	15%	15%	15%
	DE	27%	16%	16%	16%	16%	16%	16%
FEM	SE	3460%	8%	7%	12%	12%	15%	-33%
	DE	-62%	8%	8%	9%	12%	15%	-23%

WFA   FEM
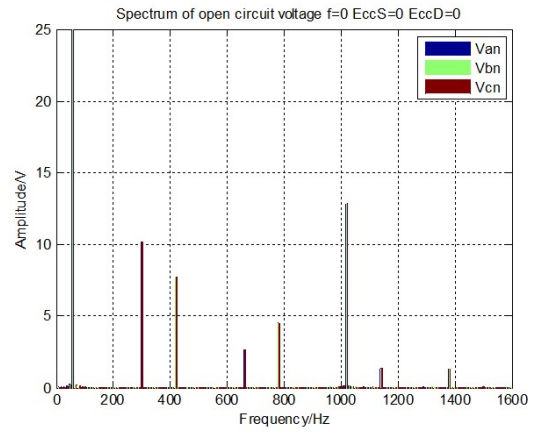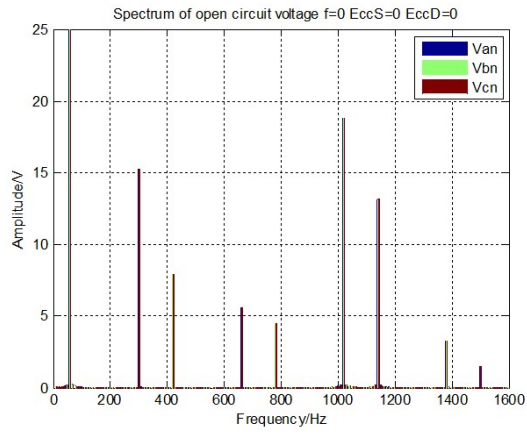
(a)   (c)

(b)   (d)

Figure 12 Open circuit phase voltage spectrums - SE

41

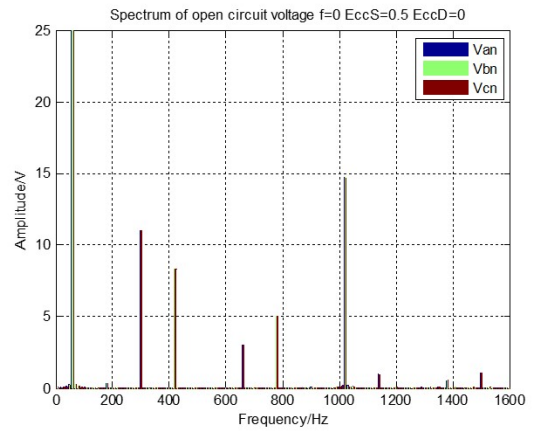WFA   FEM
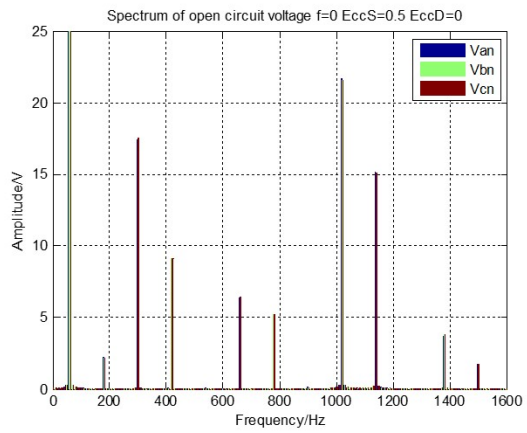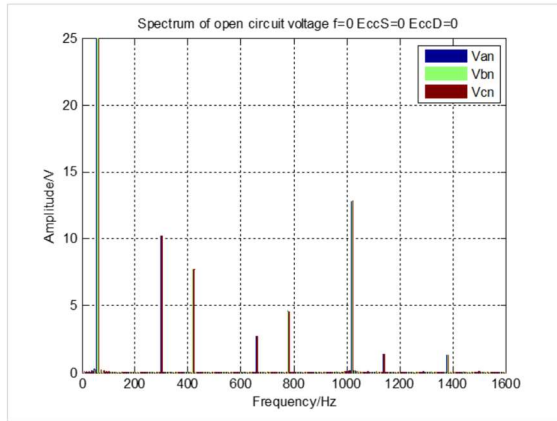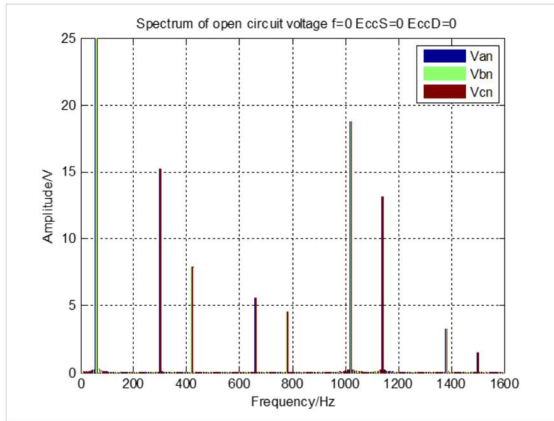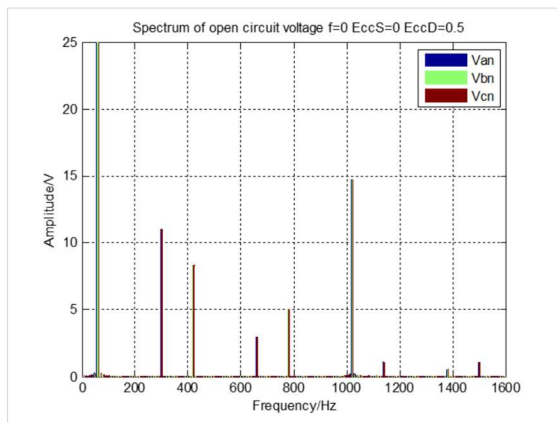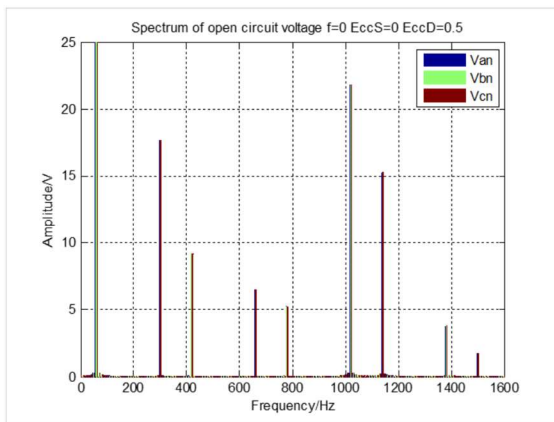

(a)   (c)

(b)   (d)

Figure 13 Open circuit phase voltage spectrums - DE

2.3.2.2 Loaded with Resistors

To simulate the loaded case, the synchronous generator model is connected with 50ohm resistors in a star configuration. The field winding is fed with 4.8A DC current. Figure 14 and Figure 15 show that the current waveforms simulated from both models are not perfect sinusoidal signals. The distortion caused by the interaction of the magnetic fields produces harmonic fluxes that move relative to the stator, and induce corresponding current harmonics in the stationary stator windings. The simulated torque waveform of the WFA model covers the envelope of the FEM result. The torque waveform of the FEM model has higher frequency components than the WFA model, because the slot effect is ignored in the WFA model.

The percentage changes of the harmonics for SE and DE with loaded case are shown in Table 4. Since the modeled SPSM is a three phase system which neutral is not connected to ground, the 3rd harmonic and its multiples are canceled out in the stator windings. The 5th and 7th harmonics decrease while the eccentricity level increases in both models, whereas the 11th, 13th, 17th, and 19th harmonics increase in both models. Either/or both signature analyses can be utilized to detect eccentricity problems, since the stator and rotor current signatures of synchronous machines have changed.
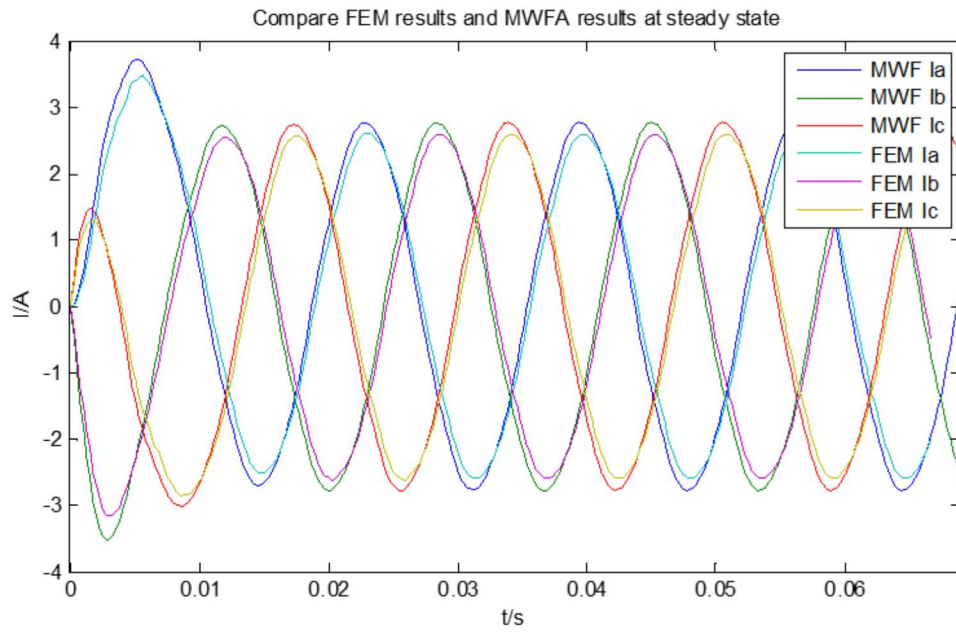
Figure 14 Currents signal in time domain
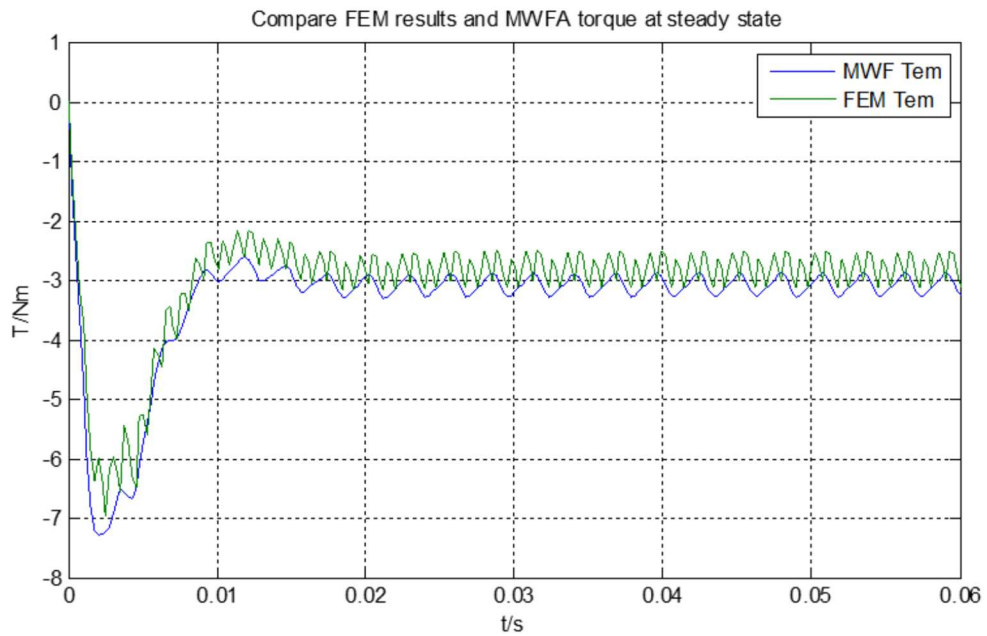
Figure 15 Electromagnetic torque in time domain

44

Table 4 Percentage change of current spectrum due to SE and DE -loaded

Order of harmonics		3rd	5th	7th	11th	13th	17th	19th
WFA	SE	244%	5%	-15%	5%	3%	5%	5%
	DE	-13%	6%	-11%	4%	3%	3%	6%
FEM	SE	1567%	-1%	-6%	3%	6%	8%	11%
	DE	33%	-1%	-6%	3%	7%	8%	12%

CHAPTER III

FLEXIBLE ROTOR WITH ROLLING ELEMENT BEARING FAULTS

In Chapter III, the methods of modeling faults of ball bearing are described and a nonlinear bearing, simplified fault model based on Hertzian contact theory is developed. A flexible rotor with built-on components is modeled using FEM. The supporting system between the housing and the base is modeled as linear springs and dampers. The excitation force caused by the bearing defects is treated as nonlinear. Numerical simulations are conducted to investigate the effects of two types of bearing faults, including outer raceway and inner raceway faults.

3.1 Rolling Element Bearing Fault Model

3.1.1 Root Causes of Rolling Element Bearing Failures

The causes of bearing failures are perhaps as numerous as the bearing installations themselves. Tallian [67] and Johnson [68] listed the many modes of failure for rolling element bearings, all of which are preventable except contact fatigue. The cause or mode of failure appears as changes or irregularities in the rolling surfaces of the bearing.

Contact fatigue is a type of a surface defect or damage that is inevitably related to the operational wear of rolling element bearings. Spalling, pitting, or flaking of the metallic particles from a bearing's rolling surfaces, namely the outer raceway, inner raceway, and rolling elements, characterize contact fatigue.

Faulty installation, including excessive preloading in either radial or axial directions, also causes bearing failure. Misalignment, loose fits, or damage occur because

of the excessive force used in mounting the bearing components. A uniformly wide wear track at the rotating raceway that extends over the entire circumference characterizes the misalignments.

Excessive wear results from dirt and foreign particles entering the bearing because of inadequate lubrication. Severe wear changes the raceway profile and alters the rolling element profile, increasing the bearing clearance. An increase in rolling friction leads to high levels of slip and skidding, and eventual breakdown.

Overheating, the ring and ball materials can be annealed by a temperature in excess of 400°C can anneal. The resulting loss in hardness reduces the bearing capacity and leads to premature failure. Discoloration from gold to blue of the rings, balls, and cages characterizes overheating.

3.1.2 Bearing Model

Studies of localized faults have used two main types of fault models. One method simulates the defect as a signal function of impulsive train for the modelled system. This impulsive train model treats the bearing as two sets of linear springs and dampers on the horizontal and vertical directions. This type of model requires less information and less computation effort, because of the linearly modeled bearing. The other method models the bearing defect as a surface bump or a dent with length, width, and depth. A high degrees of freedom (DOF) model is usually used for the bearing because the passing events of each rolling element,. The DOF is related to the total number of rolling elements. This type of model provides more possibilities for parametric studies, although the computation cost is greater.

The next sections describe a multiple DOF, simplified fault model of a ball bearing and its application to investigate the vibration of a faulty bearing running at a given speed. The assumptions are as follows:

- All rolling elements, and raceways have motions in the plane of the bearing only.

- The elastic deformations of the contacted surfaces are small.

- The mass of inner ring and outer ring is ignored.

- Deformations in the contact occur according to the Hertzian theory of elasticity.

- The cage is rigid. Therefore, all rolling elements have the same angular speed.

- The axial load is large enough, i.e., there is no skidding on the contact surface between the rolling elements and the raceways.

- The flexible housing is modeled by the springs and dampers that connect nodes of shell elements to the rigid base.

A 29 DOF nonlinear and time varying rotor bearing model is built in [67], where the rotor and housing are assumed to be rigid. In this research, the rotor and housing is treated as flexible and modeled using FEM. Lagrange method is used to derive the equations of motion for the ball bearing:

$$\frac{d}{dt}\left(\frac{\partial T}{\partial \{\dot{p}\}}\right) - \frac{\partial T}{\partial \{p\}} + \frac{\partial V}{\partial \{p\}} = \{f\} \qquad (3.1)$$

where T is kinetic energy, V is potential energy, p is the vector of generalized DOF coordinate, and f is the vector of generalized force.

To calculate the potential energy of the contact deformation, the displacements of ball, inner race, and outer race as shown in Figure 16 have to be computed first. The

contact force occurs only if there is a compression in the contact surface. Thus, the inner

and outer contact deformation for the jth ball can be expressed as:

$$\delta_i = \begin{cases} r + \rho_b - \chi_j, & if\ r + \rho_b - \chi_j > 0 \\ 0, & otherwise \end{cases}$$

$$\delta_o = \begin{cases} (\rho_j + \rho_b) - R_o, & if\ (\rho_j + \rho_b) - R_o > 0 \\ 0, & otherwise \end{cases}$$

(3. 2)

where r is the radius of the inner race, ρ_j is the radial position of the jth ball, ρ_b is the

radius of the ball, and the subscripts i and o are the inner race and the outer race,
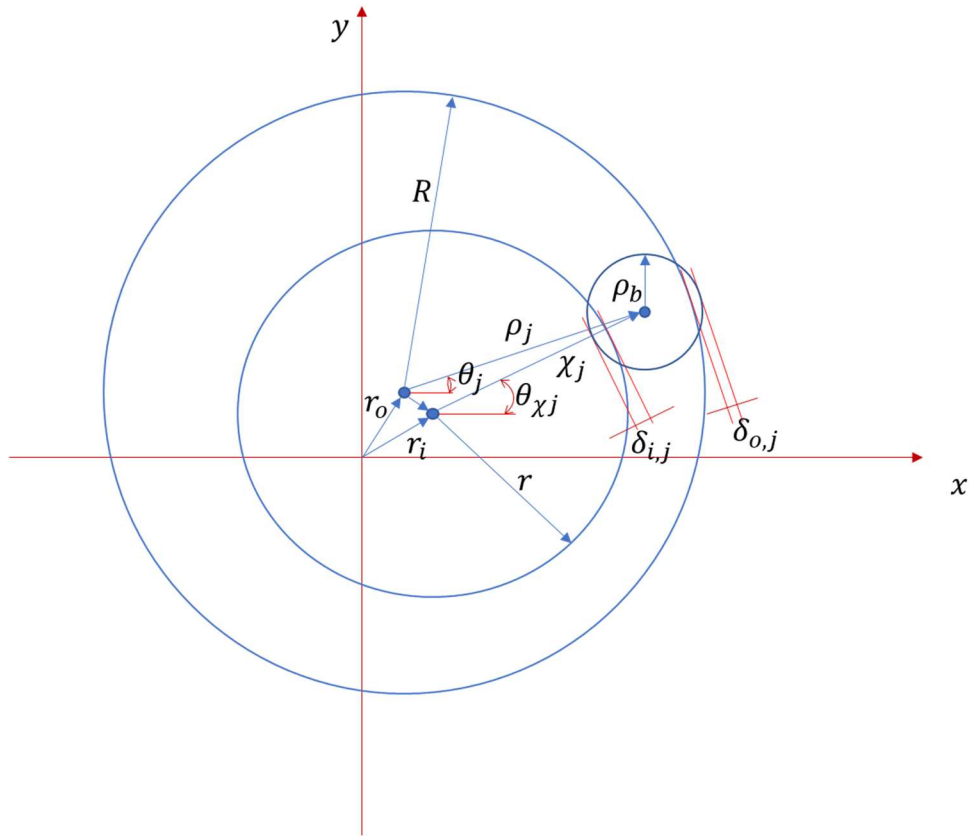
respectively.

Figure 16 The contact deformation between jth ball and the races

The offsets of the inner race and the outer race are given by:

$$\vec{r_i} = x_i i + y_i j$$

$$\vec{r_o} = x_o i + y_i j \tag{3.3}$$

$$\vec{\rho_j} = \rho_j cos\theta_j i + \rho_j sin\theta_j j$$

Since $\vec{\chi_j} = \vec{r_o} - \vec{r_i} + \vec{\rho_j}$, by substituting the expressions of $\vec{r_o}, \vec{r_i}, \vec{\rho_j}$ into the definition, the distance between the inner race center and the ball position can be obtained as:

$$\chi_j = \left((x_o - x_i + \rho_j cos\theta_j)^2 + (y_o - y_i + \rho_j sin\theta_j)^2 \right)^{\frac{1}{2}} \tag{3.4}$$

Following the method in [59], the total potential energy of the bearing is given by:

$$V = \frac{1}{2.5} \sum_{j=1}^{N_b} (k_i \delta_{i,j}^{2.5} + k_o \delta_{o,j}^{2.5}) + \frac{1}{2} u^T K u \tag{3.5}$$

where N_b is the number of rolling elements in the bearing, u is the nodal displacement vector $[x_i \quad y_i \quad x_o \quad y_o]^T$, K is the stiffness matrix of the inner ring, the outer ring and the supporting base, $\delta_{i,j}$ and $\delta_{o.j}$ are the inner and outer deformation of the jth ball, k_i and k_o are the stiffness at the contacts of inner and outer races. K is calculated by Hertzian Contact Theory as:

$$K = \begin{bmatrix} 0 & 0 & 0 & 0 \\ 0 & 0 & 0 & 0 \\ 0 & 0 & k_{hx} & 0 \\ 0 & 0 & 0 & k_{hy} \end{bmatrix} \tag{3.6}$$

The kinetic energy of jth rolling element is given by:

$$T_{b,j} = \frac{1}{2}m_j(\dot{\vec{\rho}}_j + \dot{\vec{r}}_o) \cdot (\dot{\vec{\rho}}_j + \dot{\vec{r}}_o) + \frac{1}{2}I_j\dot{\theta}_j^2 \tag{3.7}$$

The first items in equation (3.7) are from the rotation energy of individual rolling elements with respect to the inertial frame. The second term represents the kinetic energy of rotating around the rotor. For simplicity, the ball spinning energy term is ignored. Substituting (3.3) into (3.7), $T_{b,j}$ can be expressed as:

$$T_{b,j} = \frac{1}{2}m_b(\dot{\rho}_j^2 + \rho_j^2\dot{\theta}_j^2 + \dot{x}_o^2 + \dot{y}_o^2 + 2\dot{x}_o(\dot{\rho}_j cos\theta_j - \rho_j\dot{\theta}_j sin\theta_j)$$
$$+ 2\dot{y}_o(\rho_j\dot{\theta}_j cos\theta_j + \dot{\rho}_j sin\theta_j)) \tag{3.8}$$

Because there is no mass at the nodes of the housing element and the shaft element, only the kinetic energy of the rolling elements must be considered. Thus, the total kinetic energy is obtained as:

$$T = \sum_{j=1}^{N_b} T_{b,j} \tag{3.9}$$

The generalized coordinates are ρ_j, where $j = 1,2,\dots,N_b$ x_i, y_i, x_o ,and y_o . Applying Lagrange method, the equations of motion are given by:

$$m_b\ddot{\rho}_j - \rho_j\omega^2 + m_b(\ddot{x}_o cos\theta_j + \ddot{y}_o sin\theta_j) + k_o\delta_{o,j}^{1.5}$$
$$- k_i\delta_{i,j}^{1.5}\frac{\rho_j + (x_o - x_i)cos\theta_j + (y_o - y_i)\sin\theta_j}{\chi_j} = 0 \tag{3.10}$$

$$k_i\sum_{j=1}^{N_b}\delta_{i,j}^{1.5}\frac{\rho_j cos\theta_j + x_o - x_i}{\chi_j} = Q_{sx} \tag{3.11}$$

$$k_i \sum_{j=1}^{N_b} \delta_{i,j}^{1.5} \frac{\rho_j sin\theta_j + y_o - y_i}{\chi_j} = Q_{sy} \tag{3.12}$$

$$N_b m_b \ddot{x}_o + \sum_{j=1}^{N_b} m_b \ddot{\rho}_j cos\theta_j + k_{hx} x_o$$

$$- k_i \sum_{j=1}^{N_b} \delta_{i,j}^{1.5} \frac{\rho_j cos\theta_j + x_o - x_i}{\chi_j} = Q_{hx} \tag{3.13}$$

$$N_b m_b \ddot{y}_o + \sum_{j=1}^{N_b} m_b \ddot{\rho}_j sin\theta_j + k_{hy} y_o$$

$$- k_i \sum_{j=1}^{N_b} \delta_{i,j}^{1.5} \frac{\rho_j sin\theta_j + y_o - y_i}{\chi_j} = Q_{hy} \tag{3.14}$$

where Q_s and Q_h are the virtual load applied on the node of the shaft element and the housing element, respectively. By comparing (3. 11)-(3. 14), the terms with $\delta_{i,j}$ are clearly the contact forces. The forces are the same but in the opposite direction.

3.1.3 Modeling the Bearing Fault

The bearing faults emulated in the experiments are small oval pits or holes manufactured into the raceway surfaces at specific locations. Adding time varying, position dependent raceway diameters is required to incorporate the localized effects of these bearing faults into the dynamic model. In the case of both inner and outer raceway faults, the bearing defect encompasses a small region of the raceway surface only; thus, not all of the rolling elements roll over a bearing defect at any given time.

The shapes of the localized defects have been discussed in many papers. The objective of this research is to develop a rotor bearing model which can generate the vibration signatures of the bearing faults so they can be used for the SPSM model. The relationship between the vibration signatures and the electrical signatures could be investigated. Therefore, modeling the shape of the defects is beyond the scope of this research. A simplified fault model is used in this dissertation instead.
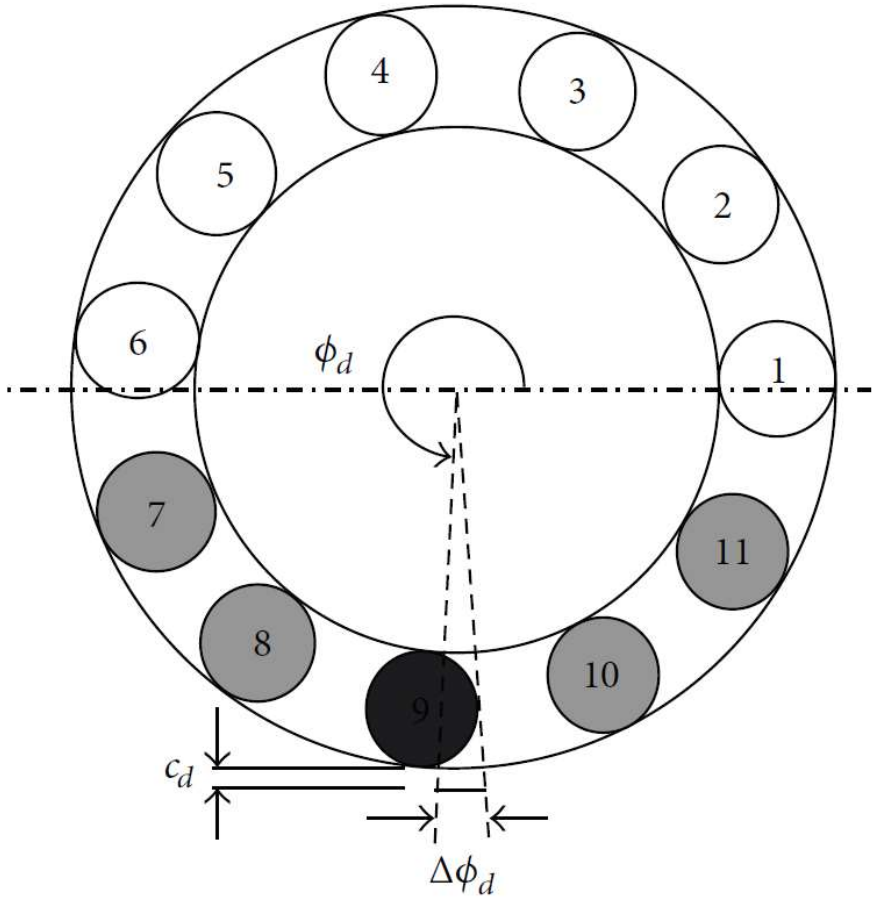

Figure 17 Diagram of outer race fault

A defect on the surface of the outer race at an angle ϕ from the horizontal axis, is shown in Figure 17. The defect formed by an oval pit takes over an angle length of $\Delta\phi_d$ on the surface from ϕ_d to $\phi_d + \Delta\phi_d$. When the jth rolling element passes through this area, the contact deformation is recovered by the extent of the pit depth. Therefore, the deformation function (3. 2), can be replaced by:

$$\delta_{oD} = \begin{cases} (\rho_j + \rho_b) - R_o - D_o , & if \ (\rho_j + \rho_b) - R_o - D_o > 0 \\ 0 , & otherwise \end{cases} \tag{3. 15}$$

Once the rolling element passes the defect area, the deformation function is reset to (3. 2).

In the case of an inner race defect, the defect rotates with the angular speed of the shaft ω_s. If the defect angle $[\phi, \phi_d]$ coincides with one of the balls, the deformation of that ball is written as:

$$\delta_{iD} = \begin{cases} r + \rho_b - \chi_j - D_i, & if \ r + \rho_b - \chi_j - D_i > 0 \\ 0, & otherwise \end{cases} \tag{3. 16}$$

3.2 Modeling the Rotor Bearing System

In this section, the method of modeling and assembling a rotating rotor with flexible housing and nonlinear bearing forces is described. The rotor with built-on components is modeled linearly. The supporting bearing system is modeled nonlinearly as discussed in section 1.

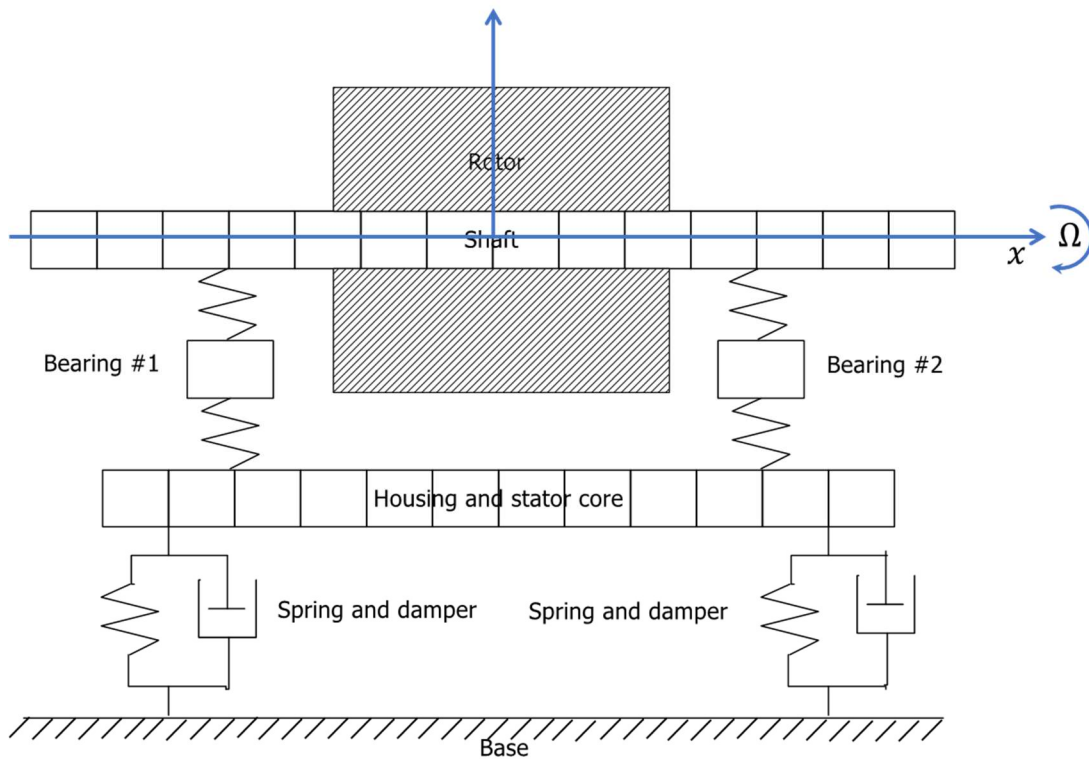**3.2.1 Flexible Rotor Modeling**

Figure 18 Diagram of the rotor-bearing system

To investigate the vibrational motion, FEM is used to model the rotor bearing system. The shaft is assumed to be axial symmetric and modeled using a 4 DOF beam

element based on Timoshenko beam theory, considering shear deformation, rotary inertia, and gyroscopic effect. A 2 DOF shell element is used to model the non-rotating housing connected to the rigid base by springs and dampers. The rotor and stator of the motor are modeled as lumped masses located on the shaft and housing nodes. The governing equations of this rotor bearing system are expressed as:

$$M\ddot{u} + (C + \Omega G)\dot{u} + Ku = F_u(t) + F_n(u, \dot{u}, t) \qquad (3.17)$$

where the displacement vector $u = \begin{bmatrix} \cdots & x_i & y_i & \theta_{xi} & \theta_{yi} & \cdots \\ & \cdots & x_{hj} & y_{hj} & \cdots & \rho_k & \cdots \end{bmatrix}^T$, x_i, y_i, θ_{xi}, and θ_{yi} represent the four DOFs of shaft node i, x_{hj}, y_{hj} represents the 2 DOF of housing node j, and ρ_k is the radial offset of the rolling element k in the bearing, M is the mass matrix, G is the gyroscopic matrix, C is the damping matrix and K is the stiffness matrix; $M, G, C,$ and K are linear terms. The nonlinear terms are moved to the right of (3.17) and included in the nonlinear force $F_n(u, \dot{u}, t)$. $F_u(t)$ is the imbalance force caused by the imbalance mass, and Ω is the angular velocity of the rotor.

3.2.2 Assembling Nonlinear Bearing Fault Model

The entire rotor-bearing system is separated into linear and nonlinear subsystems. First, the three subsystems (the flexible shaft with rotor disk, the nonlinear bearing supporting system, and the flexible housing with an attached stator part of the modelled motor) are modeled separately and then they are assembled. The four steps required to assemble the rotor bearing system are as follows:

1) Generate the linear shaft and the built-on rotor disk matrices of each element using 1D Timoshenko beam theory.

2) Assemble the linear rotor including the shaft and all built-on components and add it to the global matrices. The size of each matrix of the element is 4x4.

3) Assemble the linear housing part and add it to the global matrices. The size of element matrix is 2x2.

4) Add the nonlinear bearing system to the global matrices.

Assuming the bearing is connected to the shaft at node i and to the housing at node j,the nonlinear bearing forces calculated from (3. 11)-(3. 14) are added to force vector at node i and j as:

$$\begin{bmatrix} \ddots & & & \\ & [K_s]^{ii}_{4\times4} & & \\ & & \ddots & \\ & & & [K_h]^{jj}_{2\times2} \\ & & & & \ddots \end{bmatrix} \rightarrow \begin{bmatrix} \vdots \\ F_{brg,s} \\ \vdots \\ F_{brg,h} \\ \vdots \end{bmatrix} \tag{3. 18}$$

where $[K_s]^{ii}_{4\times4}$ is the shaft stiff coefficients of node i, $[K_h]^{jj}_{2\times2}$ is the housing stiff coefficients of node j, and F_{brg} is the nonlinear bearing force.

3.3 Simulation Results

To validate the model, three cases are simulated: healthy machine with unbalanced mass only (Healthy Machine), unhealthy machine with bearings of the outer race defects (Outer Race Fault), and unhealthy machine with bearings of the inner race defects (Inner Race Fault). Experimental data from the Bearing Center at Case Western Reserve University are used to construct the test dataset. All parameters used in this research are obtained from [67]. The test rig is built by a Reliance Electric IQ Prealert 2-horse power, three phase induction motor. The original motor bearings are replaced by defected

bearings; the defects are added to the inner and outer raceways by using the electro-discharge machining (EDM) process. The defect size and depth are 0.007 inches and 0.011 inches for the outer race defects and the inner race defects, respectively. Motor housing vibration data are measured at the 12 o'clock position of both the drive end and the fan end. The geometry of the bearings and the characteristic defect frequencies provided by the OEM are reported in Table 5 and Table 6, respectively.

Table 5 Bearing geometry (in inches) [67]

Bearing	Inner Diameter	Outside Diameter	Thickness	Ball Diameter	Pitch Diameter
Bearing 1	0.9843	2.0472	0.5906	0.3126	1.537
Bearing 2	0.6693	1.5748	0.4724	0.2656	1.122

Table 6 Bearing defect frequencies, where f_m is the shaft rotational frequency [67]

Bearing	Inner Race	Outer Race	Cage	Rolling Element
Bearing 1	$5.4152\,f_m$	$3.5848 f_m$	$0.3983 f_m$	$4.7135 f_m$
Bearing 2	$4.9469 f_m$	$3.0530 f_m$	$0.3817 f_m$	$3.9874 f_m$

3.3.1 Validation of the Rotor Bearing Model

The orbits/airgap variations are plotted in Figure 19, Figure 20, and Figure 21. In a health machine with unbalanced mass, the centrifugal force caused by the mass would pull the shaft off its rotating center, which resulted in an elliptical shaft orbit. In the case of faulty bearings, the vibration caused by the bearing defects is not synchronized with the rotating speed. Thus, shaft orbits move chaotically, not in a perfect ellipse anymore.
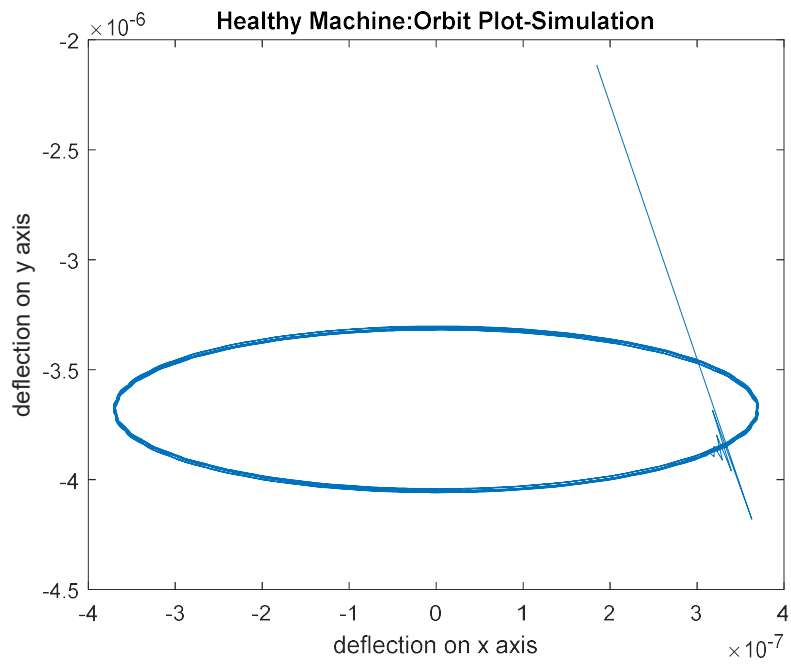
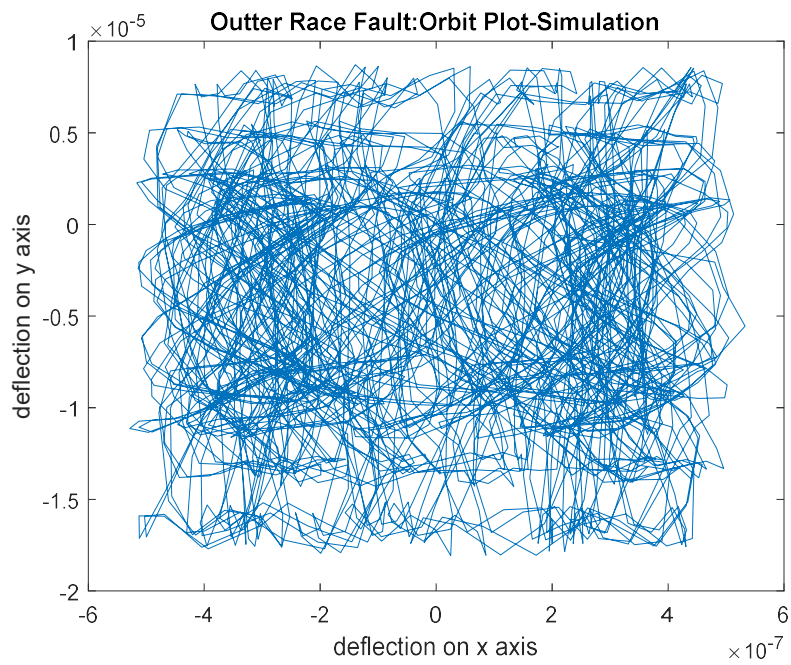Figure 19 Healthy Machine: Orbit Plot Simulation

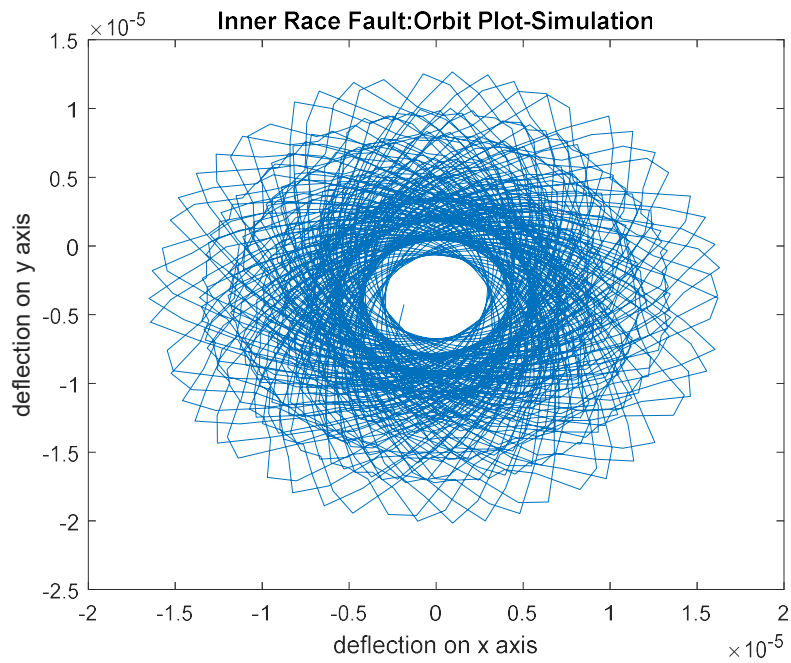Figure 20 Outer Race Fault: Orbit Plot Simulation

Figure 21 Inner Race Fault: Orbit Plot Simulation

The housing vibrations are compared in both the time domain and the frequency domain. Waveforms of the housing vibration in the experimental data and the simulated data are shown in Figure 22-Figure 25. In the time domain, both waveforms illustrate the periodically beating phenomenon caused by the defect correctly.
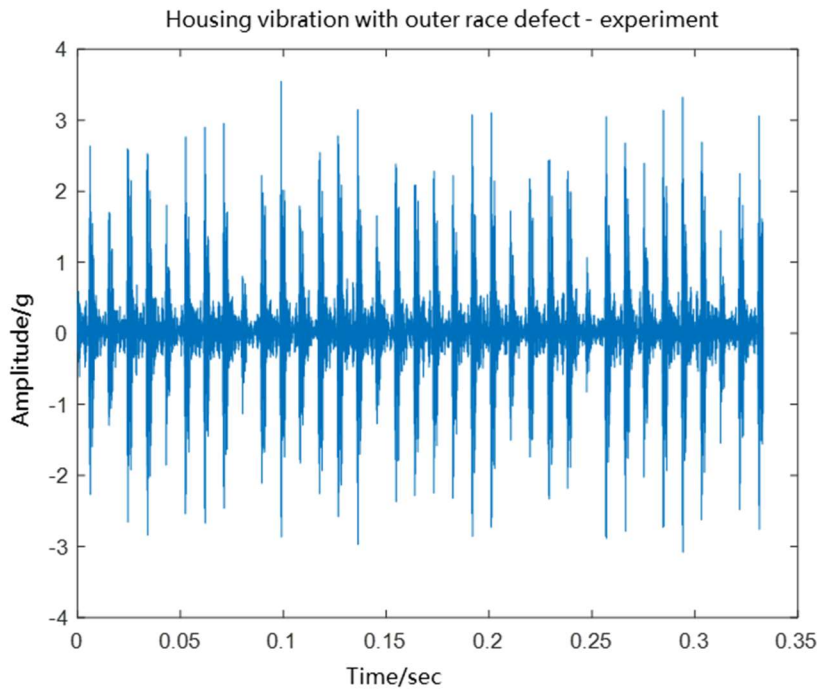
Housing vibration with outer race defect - experiment

Figure 22 Waveform of experimental data with outer race defect

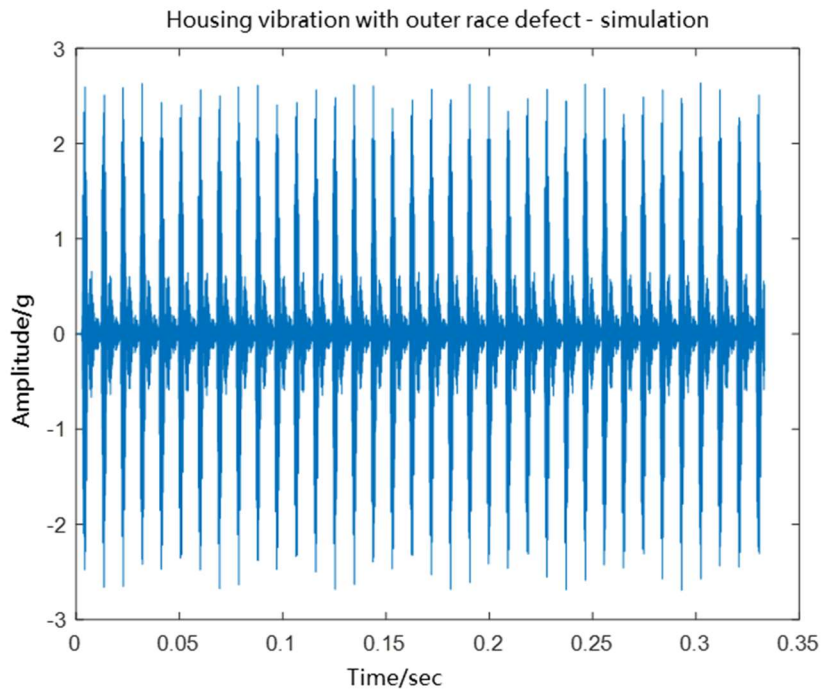Housing vibration with outer race defect - simulation

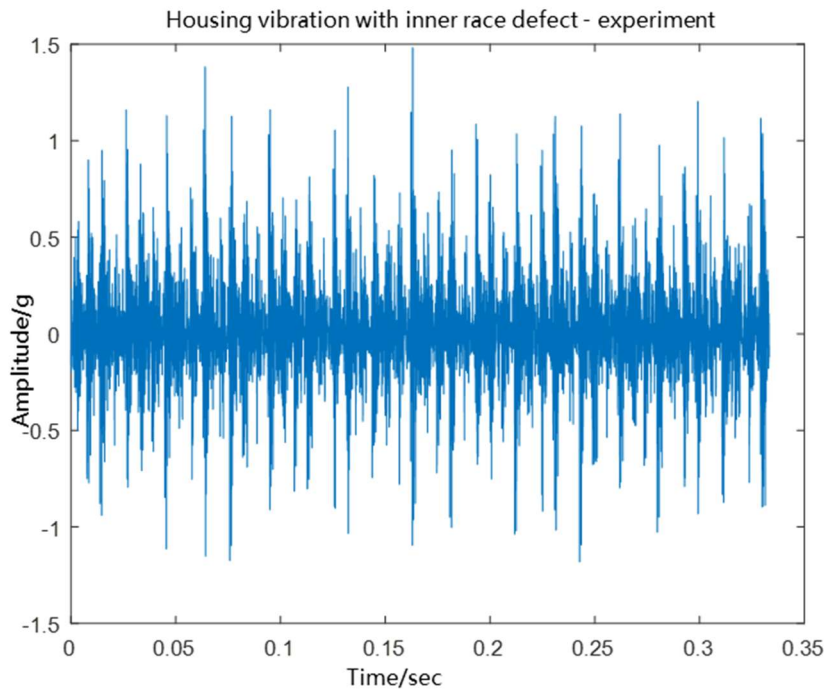Figure 23 Waveform of simulated result with outer race fault

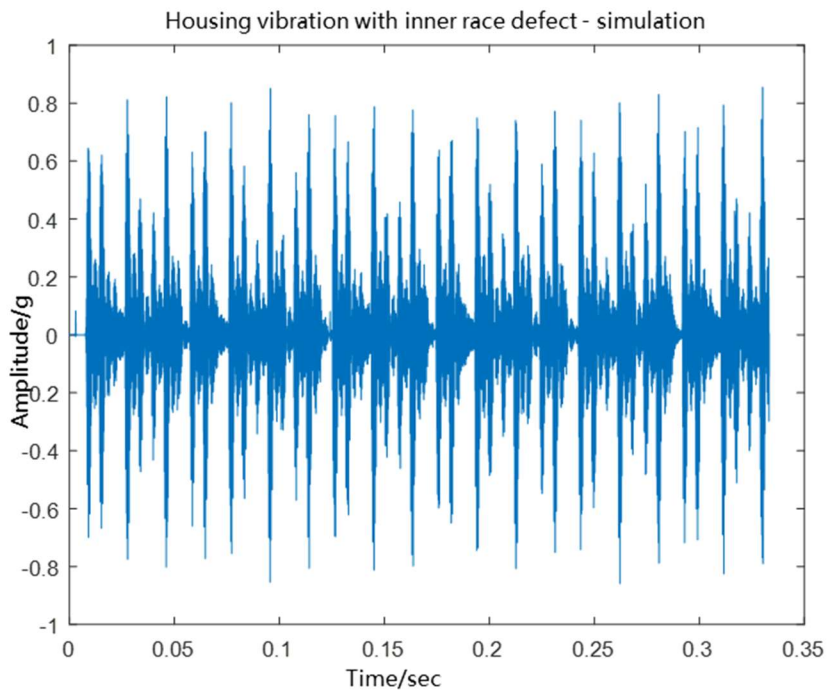Figure 24 Waveform of experiment data with inner race defect

Figure 25 Waveform of simulated result with inner race fault

Figure 26-Figure 29 show the spectral of the housing vibration. Because of the amplitude modulation, the slot between harmonics in the spectrum represents the defect characteristic frequency. The fault frequencies are about 110Hz for the outer race defect and 160Hz for the inner race defect, which match the findings on the spectrums. There are also qualitative similarities between the spectral of the real and simulated data. The bifurcation is about 3kHz in the real data spectrum and about 2.8kHz in the simulated data spectrum. The difference is acceptable considering the parameters' error between the model and the real system.
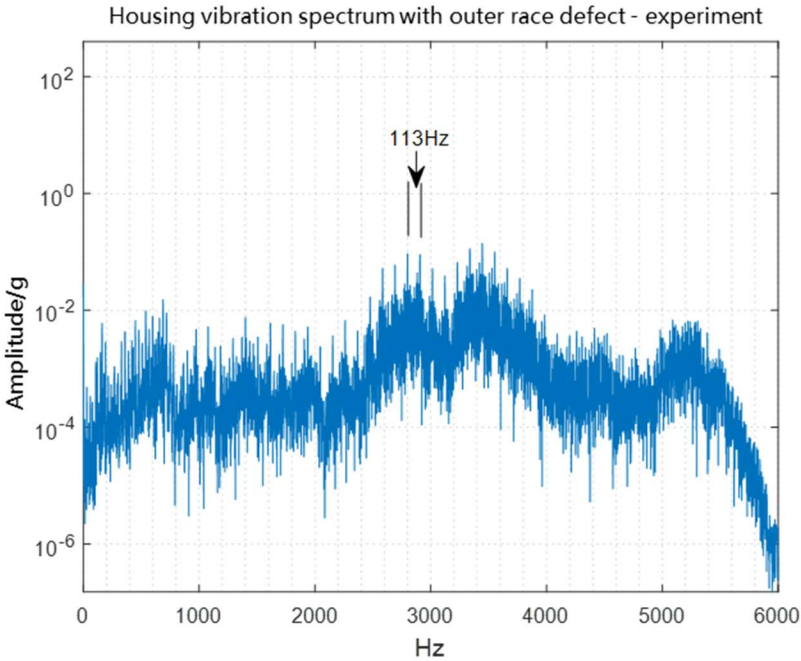

Figure 26 Experiment spectrum of housing vibration under outer race fault
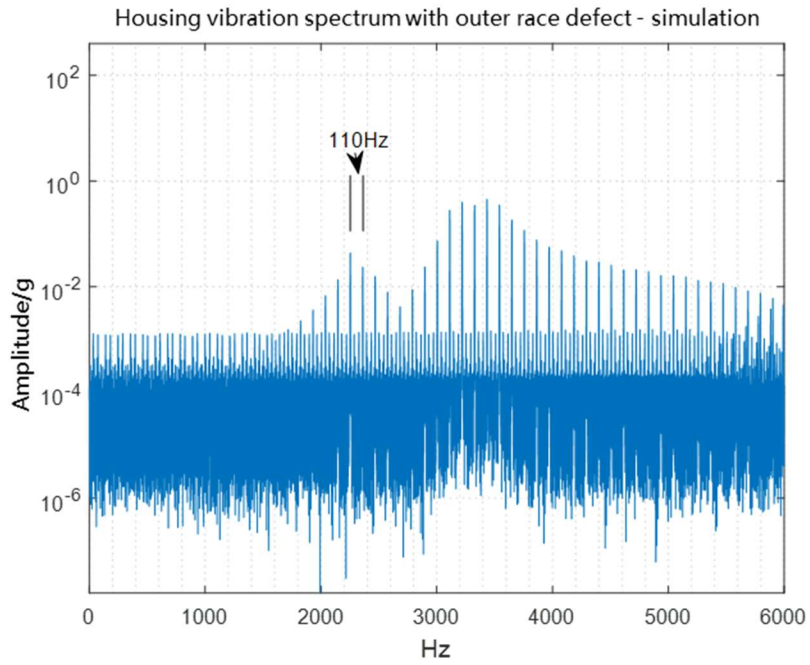
Figure 27 Simulation spectrum of housing vibration under outer race fault
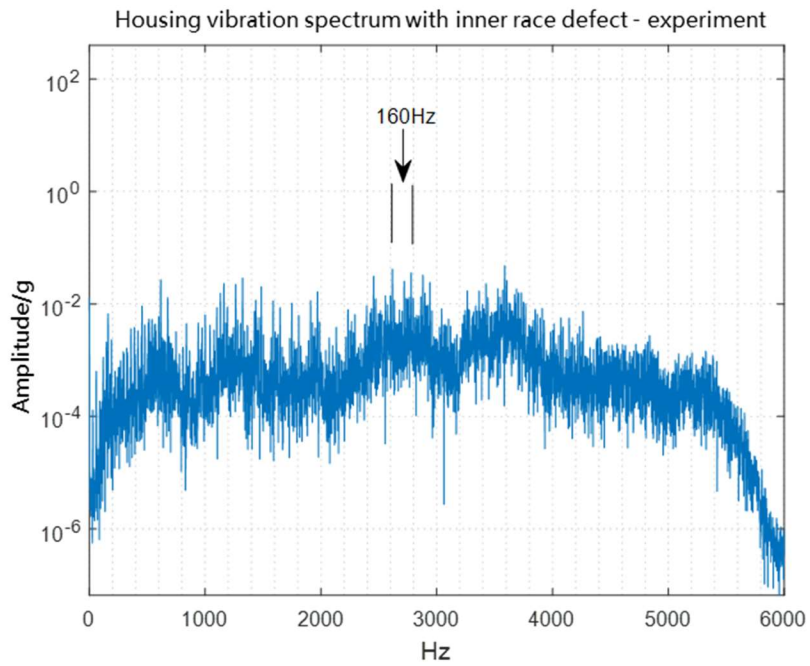
Figure 28 Experiment spectrum of housing vibration under inner race fault
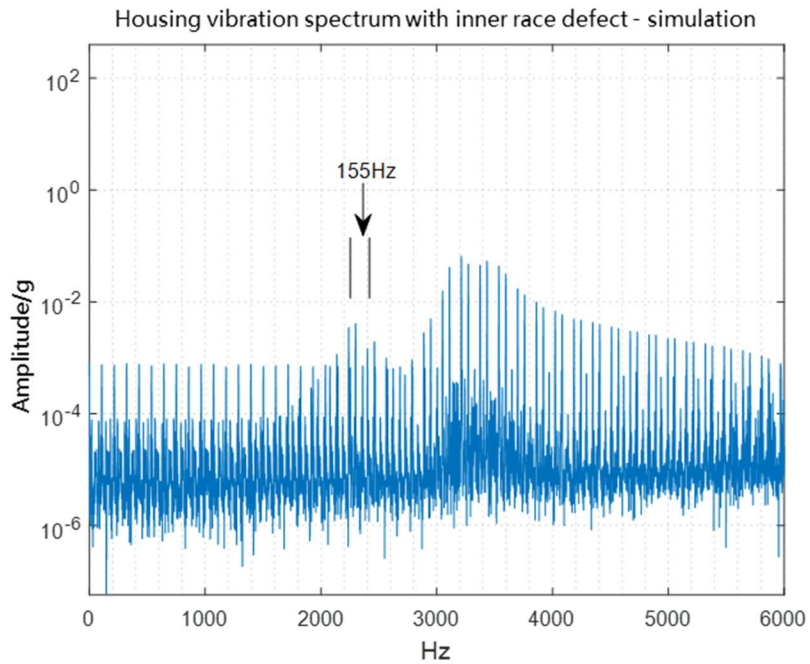
Figure 29 Simulation spectrum of housing vibration under inner race fault

The simulation results are compared to the experiment results in Figure 30 and Figure 32. Both the peak values and the excitation frequencies are well-matched between the simulation and the experiment measurements. Vibration RMS of the waveforms are calculated and the results are summarized in Table 7. The acceptable errors are 2.2% for the outer race fault and 6.7% for the inner race fault.

Figure 30 Housing vibration with outer race fault

Figure 31 Housing vibration with inner race fault(zoomed)

Figure 32 Housing vibration with inner race fault

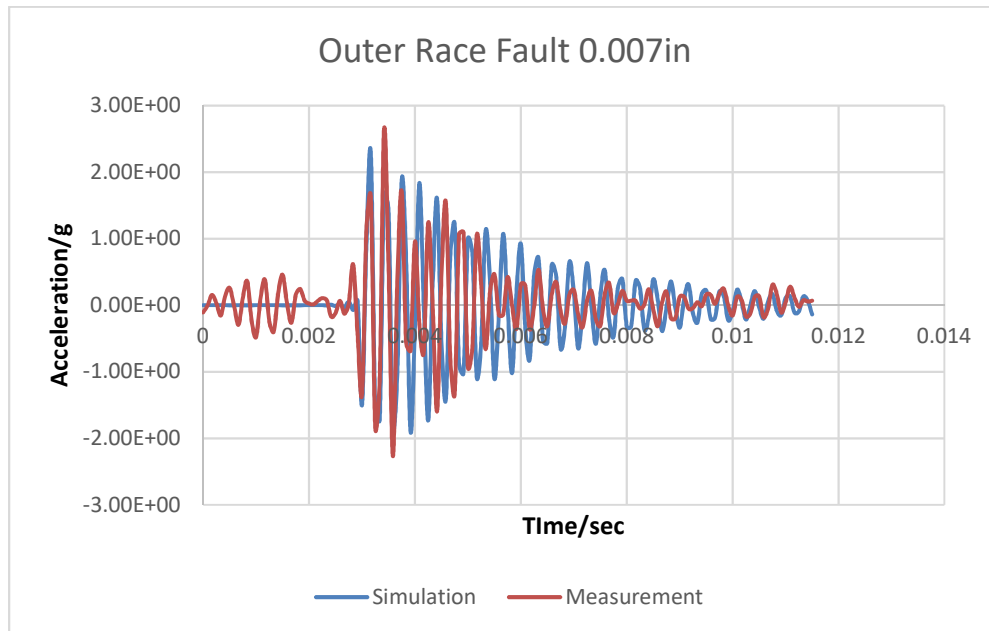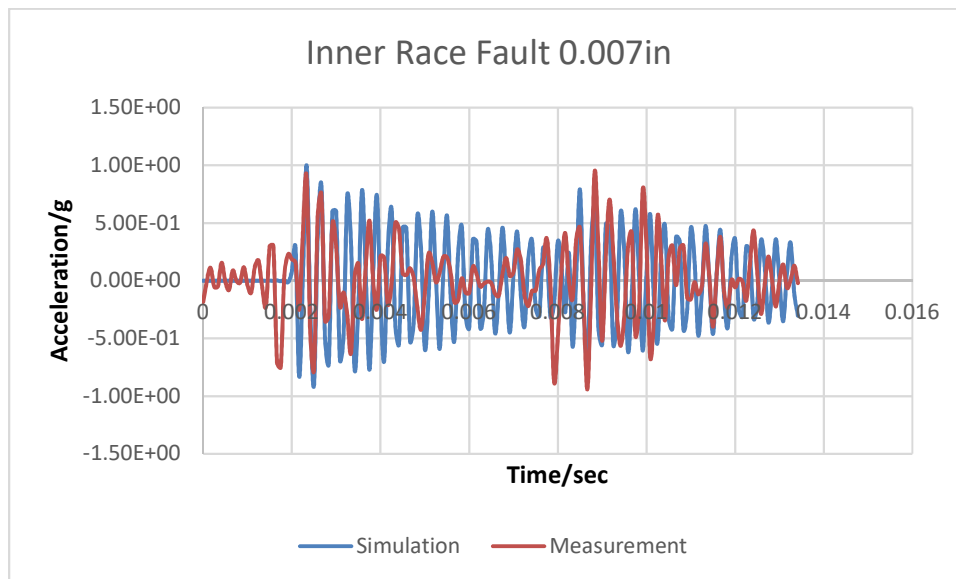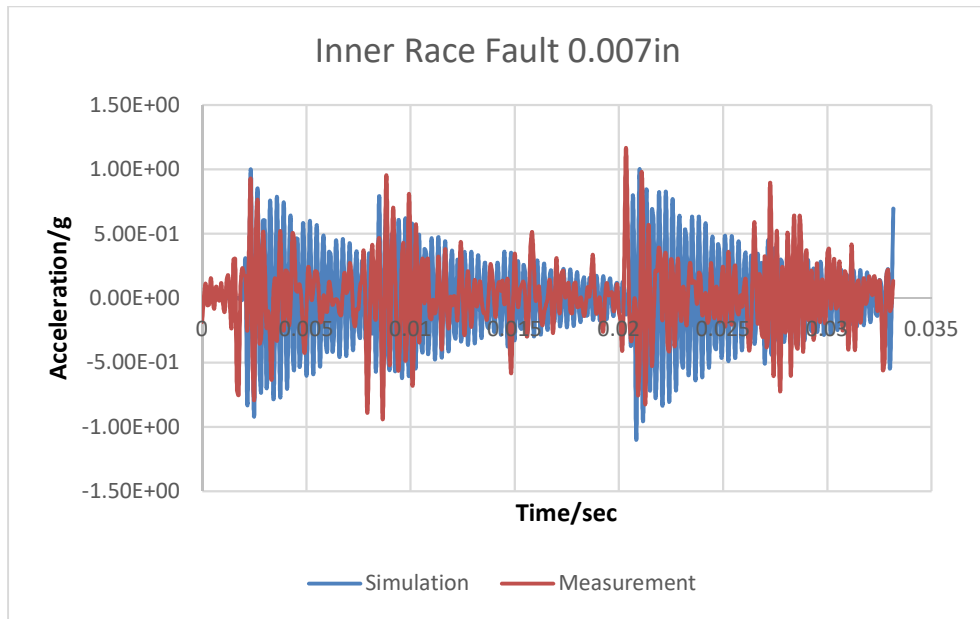Table 7 Vibration RMS

Fault Type	Simulation	Measurement	Error
Outer Race Fault	7.021	6.872	2.2%
Inner Race Fault	2.522	2.364	6.7%

3.3.2 Simulation Results of the Coupled Models

With the similarities of the simulated data and the experiment data, the developed model is considered as valid and credible. The rotor bearing system model is coupled with the synchronous machine model to investigate the electrical signature changes. The flowchart of the coupled simulation is shown in Figure 33. At time $k\Delta t$, the mechanical rotation speed ω_m, the rotation angle θ_m, and rotor center offset (x, y) are calculated based on the accelerations and velocities calculated at the last time step. The inductances are retrieved according to the position information. Electromagnetic torque T_e, terminal voltage vector V, and phase current vector I are calculated by solving the electrical model equations. A trial solution for iteration step i is obtained by applying the boundary conditions to the mechanical model. If the solution error is less than the tolerance error, the variables and the time step are updated. Otherwise, the equilibrium iteration is re-run with the latest known solution. The process is stopped when the maximum time step t_{max} is reached.
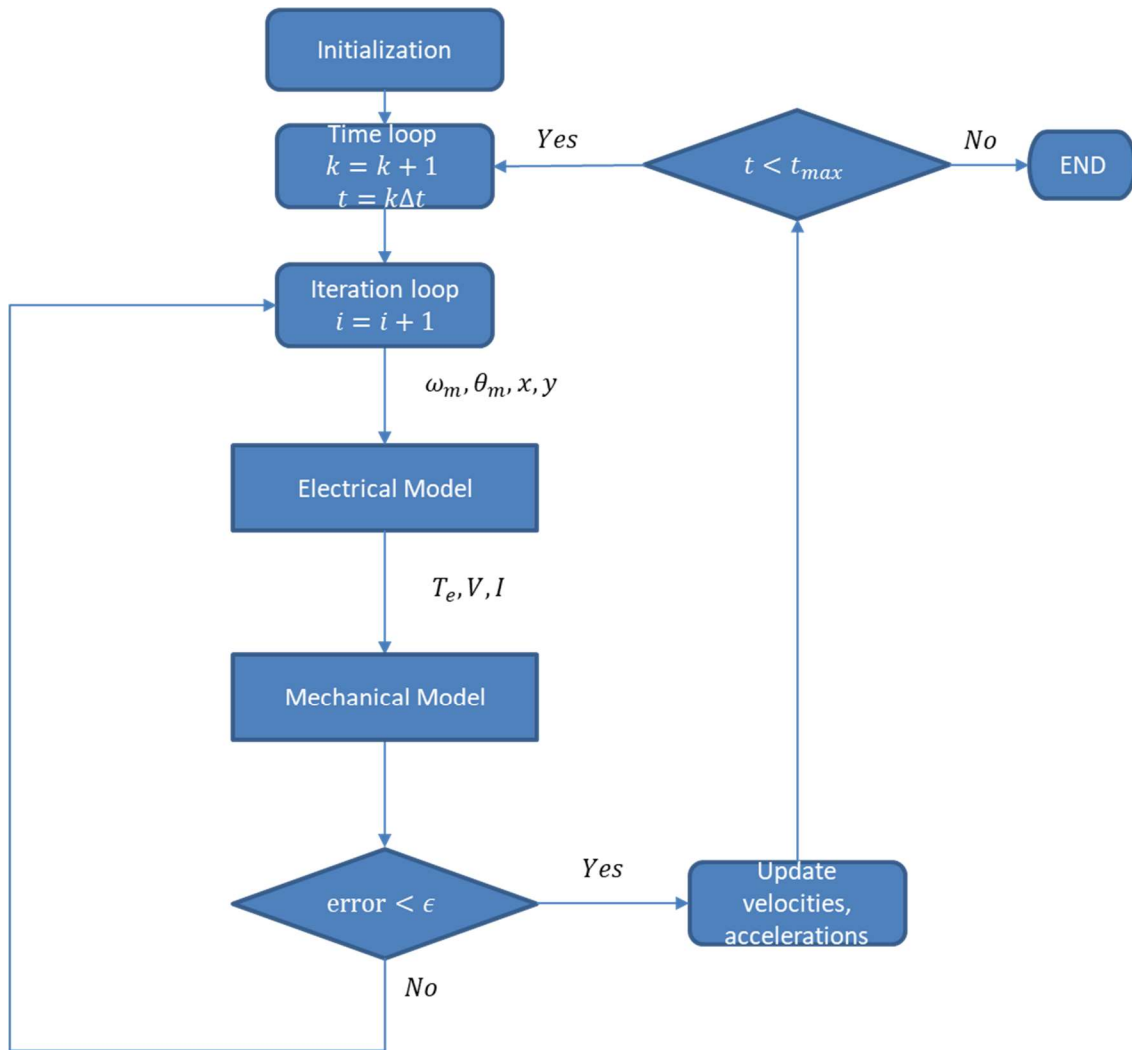
Figure 33 Flowchart of the coupled simulation

The current spectrums of the coupled system simulation with outer race fault and inner race fault are shown in Figure 34 and Figure 35, respectively. The existence of any bearing fault will result in a periodic airgap variation. The airgap changes will induce sideband components modulated on the harmonics at frequencies $kf_r \pm mf_s$, where k and m are integer numbers, f_r is the vibration excitation caused by the mechanical fault, and f_s is the line frequency. In the simulation, $f_r = 110Hz$ for the outer race fault and $f_s =$

$60Hz$ for the inner race fault. The peaks at the series of frequencies, which are clearly shown in the spectrums, reveal the interaction of the mechanical vibration and the electrical signature. According to the findings, the bearing faults' information is included in the electrical signals, and therefore the electrical signals can be used as a source to perform the fault diagnosis for the mechanical faults.
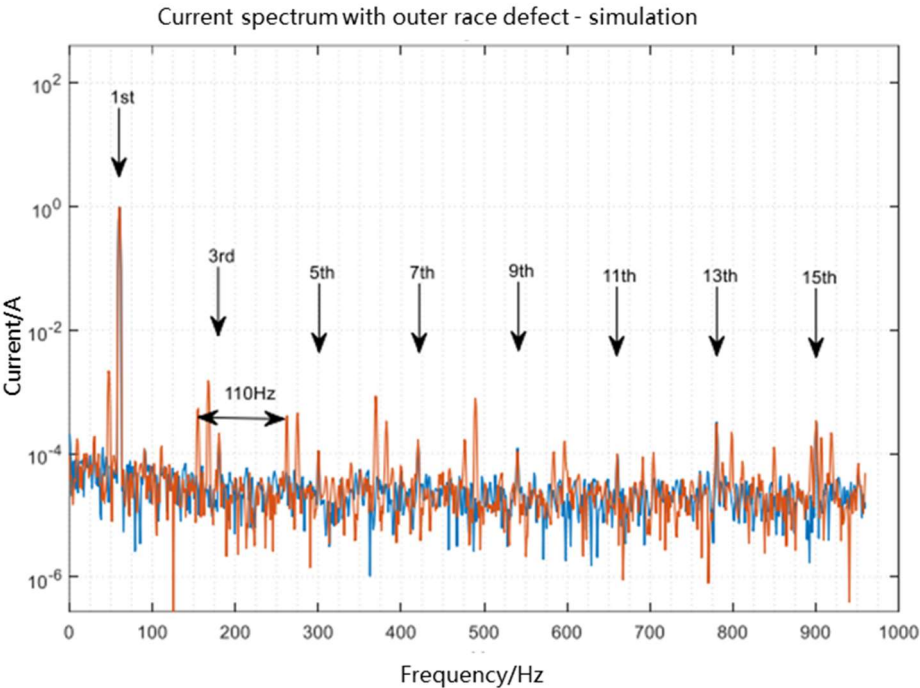
Figure 34 Coupled simulation results with outer race faults
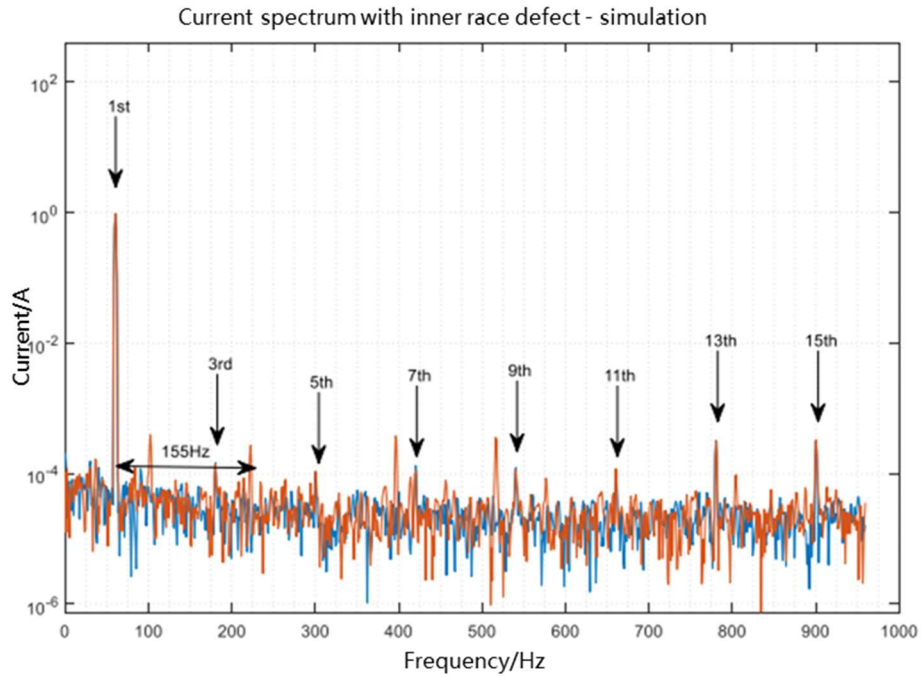
Figure 35 Coupled simulation results with inner race faults

To investigate the interaction between the severity of bearing defects and the electrical signatures, the amplitudes of frequency components along with the maximum deflection during both OR and IR are plotted in Figure 36 and Figure 37. Clearly, all fault related harmonics such as 169Hz, 369Hz in OR and 102Hz, 222Hz in IR increase when the vibration induced by the bearing fault goes up. However, unlike the case in SE and DE discussed in Chapter II, no observable pattern can be found on odd harmonics at 780Hz and 900Hz.
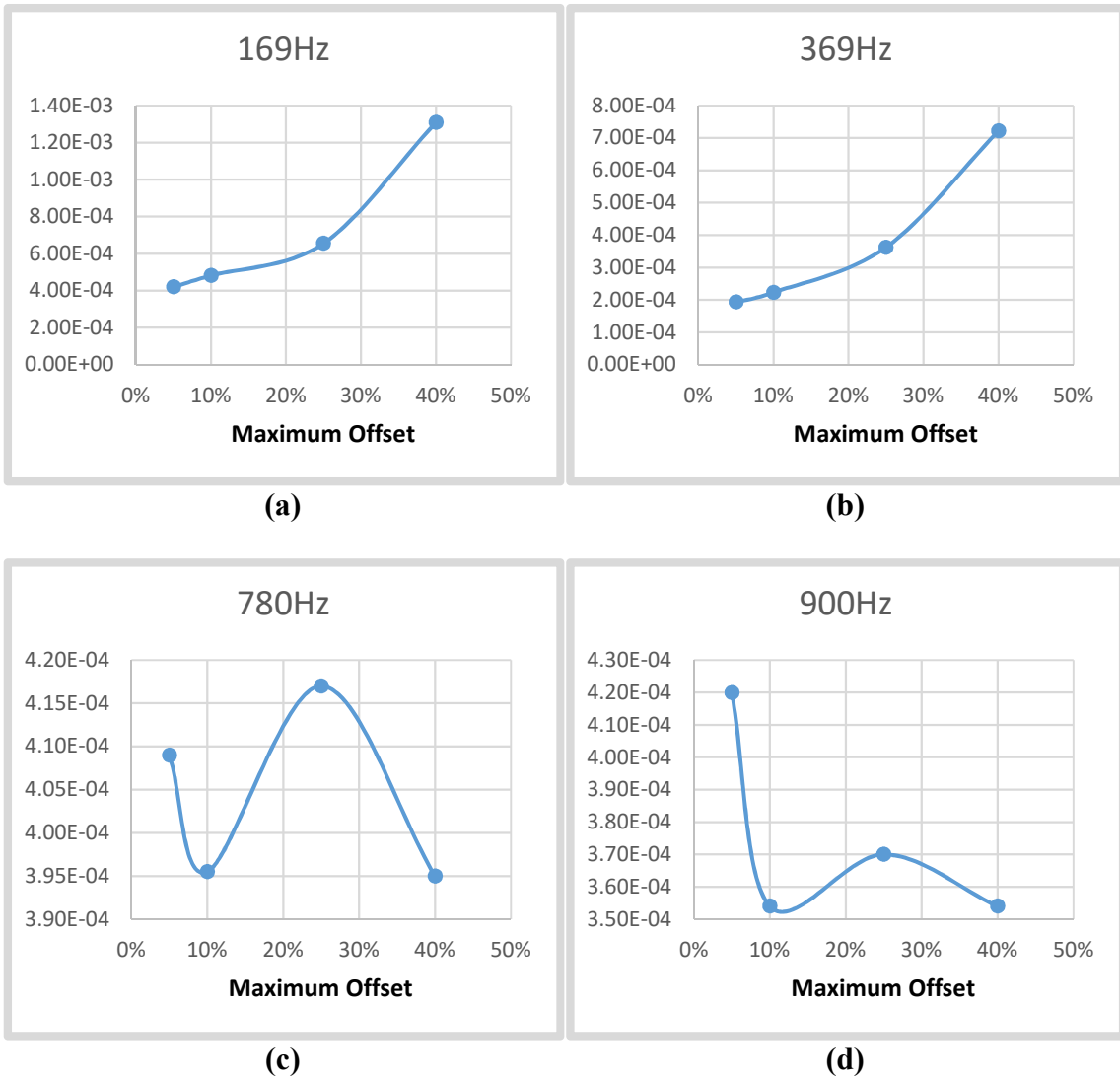
Figure 36 Frequency components changes by vibration level - OR
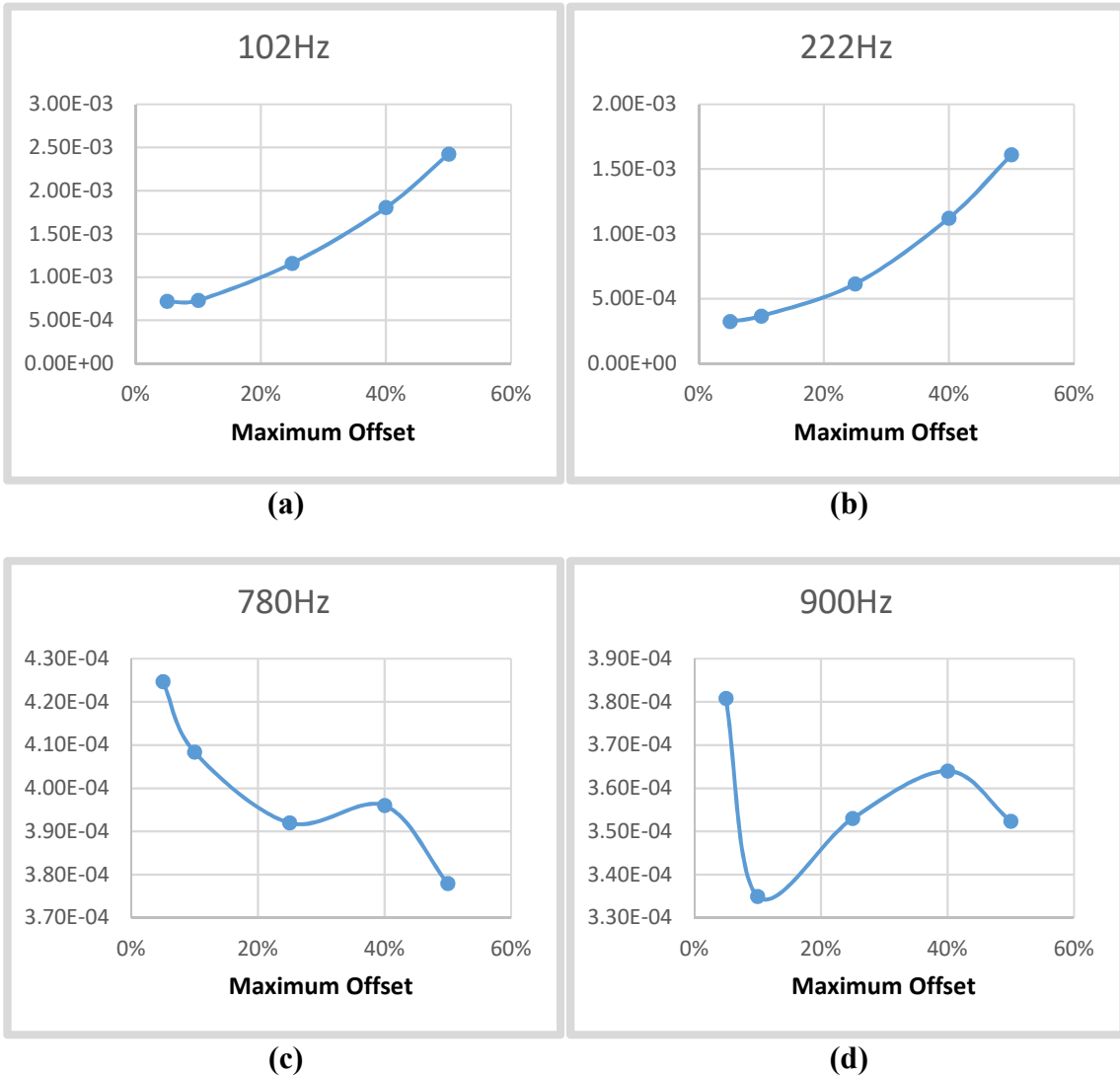
Figure 37 Frequency components changes by vibration level - IR

CHAPTER IV

ESA AND EXPERIMENT RESULTS

In this chapter, first the in-situ bearing deterioration experiment setup will be simply illustrated. Then we will investigate the nature of the generalized roughness bearing defect and its physical link to current signature. The power quality variation will be illustrated to show how the non-stationarity of power input could affect the ESA of subtle current signature of generalized roughness bearing defect. The discussion on the nonstationary, locally and piecewise stationary signal lead to applying principal component analysis (PCA) to the experimental data. The data processing results are shown in Section 3.

4.1 Experiment Setup

4.1.1 In-situ Bearing Deterioration

Modern AC converters have a high du/dt combined with a high switching frequency, i.e. the sum of the 3 phase voltages is no longer zero. This nonzero and high-frequency common-mode voltage can be considered the root cause for different kinds of bearing currents. Basically, the damage is always caused by partial discharge, which is called Electrical Discharge Machining (EDM). This film of lubricant serves as a dielectric and allows the bearing to behave as a capacitor. The capacitor created within a bearing between the inner /outer race and the ball is shown in Figure 38. This capacitor is charged by the bearing currents. When the voltage level is high enough, it is discharged by a short circuit. Eventually, the metal is eroded by the periodic discharging.
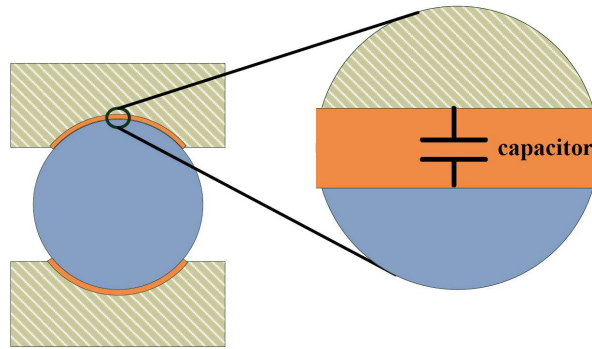
Figure 38 Capacitor model between the bearing housing and the rolling element

In [60], a shaft current injection method was proposed to emulate the generalized roughness bearing defect, which is a more practical anomaly in the field, and avoid the disassembly of the electrical machines and operational disruption. Therefore, the possibly

misleading vibration and electric signatures induced by reinstalling the bearing in the offline defect creation method are eliminated.

4.1.2 Experiment Setup
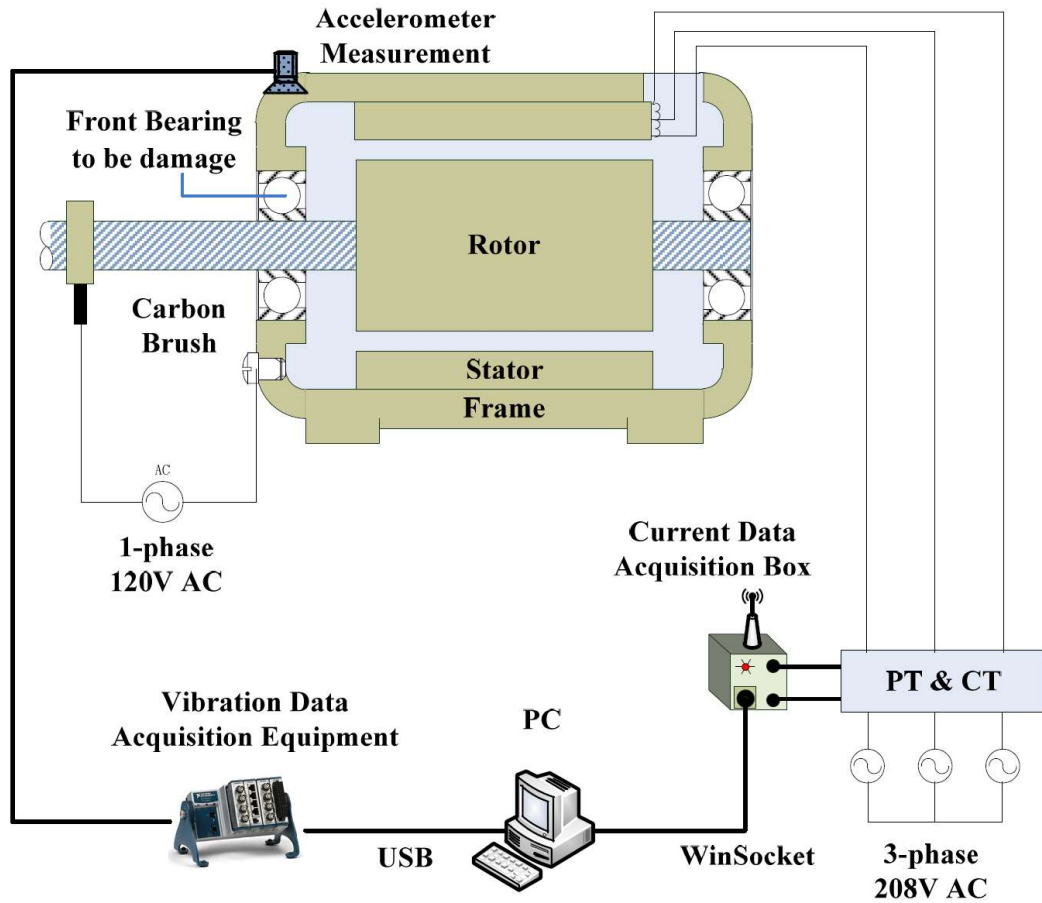
Figure 39 The experiment setup of the in-situ bearing deterioration process

The setup for the experiments performed for airgap variation induced by bearing generalized roughness is shown in Figure 39. Motor terminal quantities are sensed through current/voltage transducers and fed into a customized data acquisition box, and the

vibration signals are measured by an NI DAQ device. The two Marathon Electric synchronous machines 281PDL1722 with 8.8KW rated power, 240V/3 Phase are used in the test-bed as shown in Figure 40. One is used in motor mode as the primary drive and the other one is used in generator mode loaded by a water heater.

Figure 40 The testbed

For current injection, an external voltage source is applied to the shaft of the motor via a carbon brush. Because of convenience and availability, a single-phase, 120V 60Hz AC power adjusted by a transformer is used to provide the controllable shaft voltage. Replacing the NDE bearing with a ceramic one allows a current to flow from the shaft through the drive end bearing and return to the power negative from the stator frame. The deterioration process is accelerated by removing part of the lubrication grease in the

bearing. An aluminum disk is mounted onto the shaft to provide a smooth contact surface for the brush.

The vibration signals on the top of the bearing housing are collected to evaluate the deterioration level of the bearing. The accelerometer 352C33 with an amplitude range from -50g to 50g, a sensitivity of $100mV/G$, and a frequency range from $0.2 - 5000Hz$ is used to measure the vibration, and the. DAQ system NI USB-9234 is used to collect the vibration data. The latter system, a USB-based four-channel C Series dynamic signal acquisition module that makes high-accuracy audio frequency measurements from sensors, is ideal for a wide variety of portable applications, such as industrial machine condition monitoring, in-vehicle noise, vibration, and harshness testing. The device and its chassis cDAQ-9174 is shown in Figure 41.
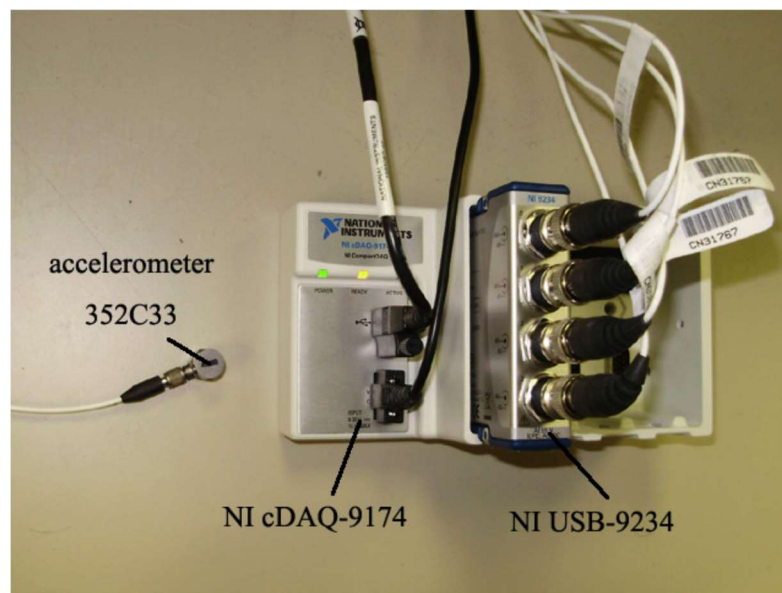
Figure 41 Vibration DAQ system

Because the electrical signals cannot be measured directly by the data acquisition system, the phase currents and the line voltages have to be converted to low measurable voltage signals through current transducer (CT) and potential transducer (PT), respectively as shown in Figure 39. The AD73360, a six-input channel analog front-end processor, is used in the electrical signals collection. It is particularly suitable for industrial power metering as each channel samples synchronously, i.e. in this setup, the voltage signals and the current signals of three channels are sampled simultaneously. The sampling rate is set to 8 kHz.

4.2 Electrical Signature Analysis

In Chapters II and IV, the physical link between the airgap variation and current signatures in a synchronous machine is investigated. Based on the simulation results, the airgap variation caused by the bearing defects is modulated on the fundamentals and the odd harmonics of the electrical signals. Thus, the bearing defects are detectable by using electrical signature analysis.

In a real-world environment, an incipient bearing defect usually occurs in the form of a generalized roughness surface, but it is not possible to identify a specific frequency in the defect's signature. Instead, unpredictable broadband changes in vibration and stator current spectrum are induced, which can be detected by simply using Root Mean Square (RMS) analysis. The RMS vibration value provides a good indicator for the health level of the machine, as stated in ISO-10816. However, in the electrical signature, the components after modulation are small compared to the fundamental harmonics.

Therefore, appropriate preprocessing methods and high-resolution data processing algorithms are required to analyze the electrical signature.

4.2.1 Signal Segmentation

In real world, current and voltage signals in an electrical machine are nonstationary. When electrical machines are running, factors such as power supply quality and load disturbances cause deviations in the values of current and voltage signals. For example, the load-induced harmonics in the stator current spectrum would obscure certain fault signatures, if the load of an electrical machine fluctuates over time. The sensitivity of any proposed ESA based fault detection methods would be degraded in this situation. When the measured signal is nonstationary, more complicated signal processing techniques are required in a fault diagnosis system than in a system dealing with stationary signals.

Because of the nonstationary nature of the electrical signals, methods considering whole-spectrum energy content have been proposed to detect generalized roughness bearing faults, e.g., in [61] non-bearing faults components were removed from the signal and the residual was used to seek the frequency bands with a high probability of the presence of a bearing fault. The spectral kurtosis of the signals investigated in [62] [63], has proved useful for identifying the bandwidth where the fault-related signatures were more likely to appear on localized bearing faults and vibration monitoring. None of these studies, however, accounted for the influence of power quality change, load change, speed change, and other environmental variables.
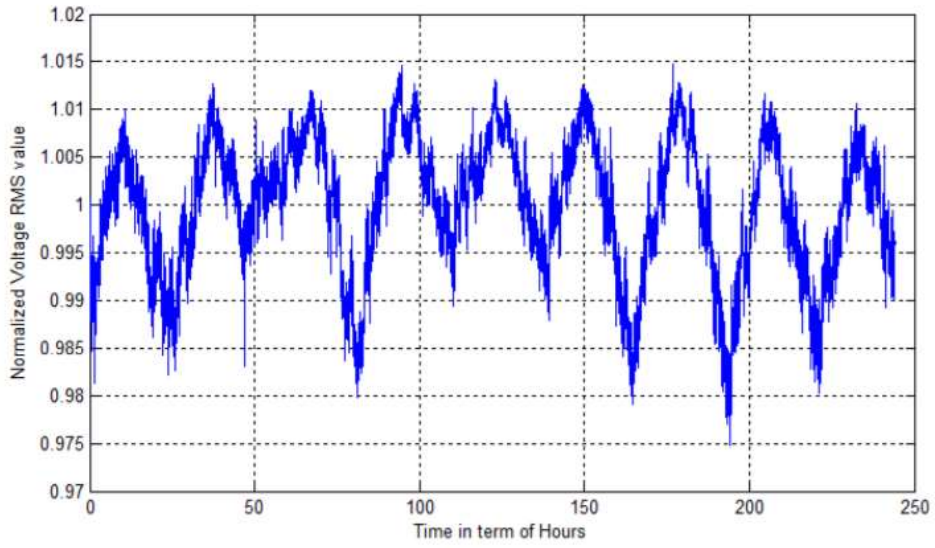
Figure 42 Voltage RMS variations with time
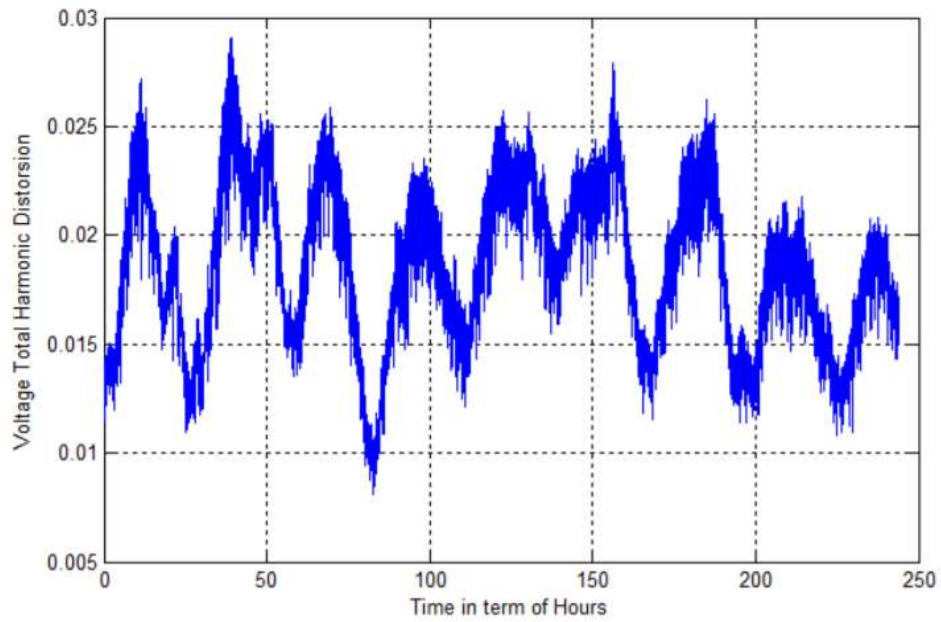
Figure 43 Voltage THD variations with time

The voltage amplitude change during the 240 hours of normal operation is shown in Figure 42. The difference between the peak and the valley is about 2% of the average value. Total harmonics distortion (THD) is another measurement for the quality of the power input as shown in Figure 43.The voltage THD, which varies 25% during the operation, has significant impact on the magnitude of the modulated signal. The main sources of these variations may come from static frequency converters, cycloconverters, load changes in the power grid, etc. In the presence of these nonstationary variables, the electrical signature are difficult to pick up by directly applying spectral analysis approach [64]; thus, the data must be segmented in order to isolate the influence of the nonstationary variables.

4.2.2 Feature Extraction

Feature extraction is the essential step of the diagnostic of machinery, which can be treated as a problem of pattern classification/recognition. In the field of machinery fault diagnosis, signatures in time domain and frequency domain are the two main sources that features can be extracted from vibration analysis. The features both in time and frequency domain have been applied successfully [73]. In electrical signature analysis, because the fault signals are modulated on the line frequency and higher order harmonics, the features are usually extracted in frequency domain for stationary signal. In this dissertation, multiscale analysis is applied on the frequency domain and the features in the time domain are extracted by combining zoomed FFT and PCA.

4.2.2.1 Zoom Fast Fourier Transform

As mentioned, the characteristic bearing fault frequency is modulated on the fundamental and space harmonics of the electrical signatures. Traditional FFT methods are implemented to perform the spectrum analysis of the stator current. The magnitude of these fault frequencies, however, is subtle compared to other frequency components. Therefore, to identify the subtle changes in the electrical signatures, a high-resolution frequency analysis method is required.

The zoom FFT (ZFFT) is a useful algorithm to zoom in the narrow frequency band centered on a selected frequency [63]. The frequency resolution of the FFT is related to the sampling time and the number samples. In real applications on DSP-based systems, the size of FFT is limited by the memory available on the boards. Compared to traditional FFT method, ZFFT can reduce the sampling rate to decrease the number of samples and keep the same frequency resolution. The ZFFT algorithm used in this dissertation is shown in Figure 44.
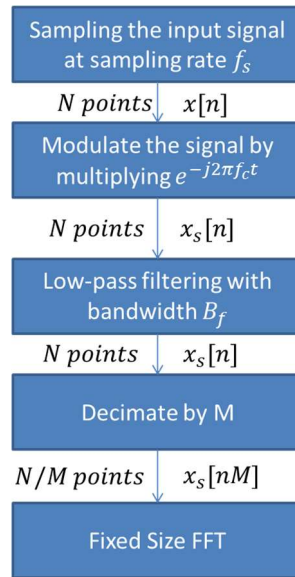
Figure 44 ZFFT algorithm

Initially, the sampled signal $x[n]$ is obtained after sampling the signal $x(t)$ at the

rate f_s. Then by multiplying $e^{j\frac{2\pi}{f_s}f_c}$, the spectrum of the signal is shifted by f_c in the

frequency domains as shown in (4. 1). In this way, the sampled sequence $x_s[n]$ is centered

on f_c. The complex signal $x_s[n]$ is then filtered by a low-pass filter with bandwidth B_f.

After filtering, the frequency range becomes $[f_c, f_c + B_f]$. To extract the frequencies in

this band, a $2B_f$ sampling rate is enough according to the Nyquist-Shannon theorem. By

downsampling the sequence at an integer rate $M = \frac{0.5f_s}{B_f}$, the new sequence $x_s[nM]$ has

N/M samples, and the reduced frequency signal dimension order saves both computation

time and memory for the given bandwidth:

$$x[n]e^{j\frac{2\pi n}{f_s}f_c} \leftrightarrow X[k - \frac{N}{f_s}f_c]$$

(4. 1)

The frequency spectrum includes the amplitude spectrum and power spectrum. Both are utilized in fault diagnosis. The odd harmonics and inter-harmonics are generated by different root causes. Odd harmonics in the electrical machine are usually caused by the setup of the windings, which is also called space harmonics, and synchronous vibrations such as oil whirl and rotor unbalance. The root causes of inter-harmonics can be bearing defects, shaft crack, gear faults, etc. Therefore, the frequency range is divided into 24 bins. Applying ZFFT to each bin obtains the spectrum of the expanded bandwidth. The sum of inter-harmonics in the selected range is calculated as fault features as well as odd harmonics.

Table 8 The selected 24 features (f is the line frequency)

Feature No.	1	2	3	4	5	6	7	8	18-23	24
Bandwidth	(0,f)	f	(f,2f)	(2f,3f)	3f	(3f,4f)	(4f,5f)	5f	...	(15f,16f)

4.2.2.2 Principal Component Analysis

In vibration monitoring, the amplitude of vibration signals increases when the severity of the defect in the machine components degrades [65]. However, as the defect severity increases, the overall vibration curve is composed of an increasing trend and local variations of smaller magnitudes. Because of the stochastic nature of the fatigue failure progression process, it can be difficult to apply fault detection method to obtain usable

85

indicators from a contending feature set [78]. As shown in [76], features that provides incorrect information reduce the accuracy of fault diagnosis. Therefore, an appropriate feature selection method is needed to select the features that describe the defect condition best and eventually lead to reliable fault classification, diagnosis/prognosis. In multivariate data analysis, PCA is commonly used to analyze the covariance structure of data. This approach was developed to reduce the dimensionality of the input features for supervised and unsupervised classification purposes.

Originated in the fundamental work of Pearson [66], PCA is generalized as a classic technique in statistical data analysis, feature extraction and data compression. The basic idea of PCA is that the elements are correlated mutually. Redundant information exists in multiple elements, which makes compression possible. By finding a rotated orthogonal coordinate such that the elements of x in the new space are uncorrelated, the redundancy induced by the correlation can be removed.

Figure 45 shows that with PCA the sample is centered and rotated to line up with the direction of highest variance. It is noted that on the new coordinates, the variance on z2 is small so that it can be ignored and the number of features is reduced from two to one.
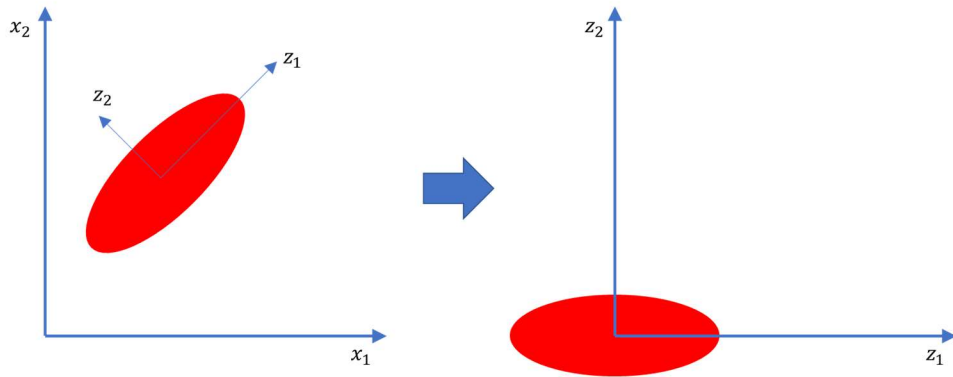
Figure 45 Coordinate transform

Considering a random vector x with n elements, a sample $x(1), ..., x(N)$ is collected by N measurements of x. Let X be the sample matrix $[x(1)\ x(2) ... x(N)]$. Based on PCA algorithm, the feature selection method is illustrated below:

1) For the covariance matrix $C = Cov(X)$, find a singular value decomposition $C = U^T S U$ such that S is a diagonal matrix and the singular values are put in descending order on the diagonal.

2) Project the original features onto a new coordinate with the transform matrix U as $y = Ux$.

3) Take into account the first k components that explain more than 90% of the variance according to $\Sigma_{i=1}^{k} s_i / \Sigma_{i=1}^{n} s_i$, where s_i is the ith largest singular value.

4) Use the projected features to classify.

87

It should be noted that PCA only valid when the following assumptions and limits are met [81]:

- The problem is linear. For nonlinear problem, other methodologies must be used to project the data from nonlinear space to the linear space such as kernel method.

- The probability distribution of the variables must be normal.

- The principal components are orthogonal, which offers an intuitive simplification that makes PCA soluble with linear algebra decomposition methods.

- Large variances have significant dynamics, which implies the data have high SNR.

4.2.3 Proposed Method

As mentioned, the airgap variations caused by mechanical faults are included in the electrical signatures. ESA therefore does not require additional sensors and can provide continuous monitoring of the machine. It is also a non-invasive method. The vibration caused by bearing defects is modulated on the fundamental and higher order harmonics. Thus, the fault information is hidden in the sidebands of odd harmonics. In this dissertation, a new bearing faults diagnosis method that combines the high resolution spectral analysis method ZFFT with the PCA multivariate monitoring approach is proposed. The flowchart is shown in Figure 46.
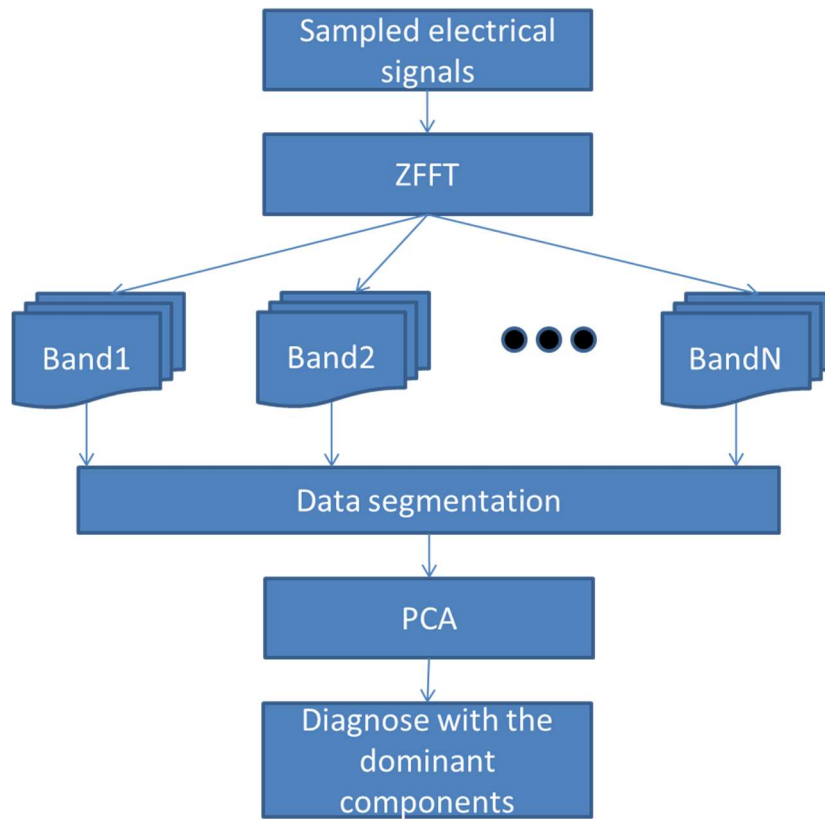
Figure 46 Flowchart of the proposed method

In the proposed diagnosis method, voltage and current signals for three phases are sampled simultaneously for every given time window t. ZFFT is then employed on each sideband of the odd harmonics, and the amplitudes of each frequency band are summed. The resulting metrics matrix with the features is reported in Table 8. Loading of the machine is used to segment the metrics matrix, PCA is applied on the segmented data, and the first two principal components are selected for the diagnosis.
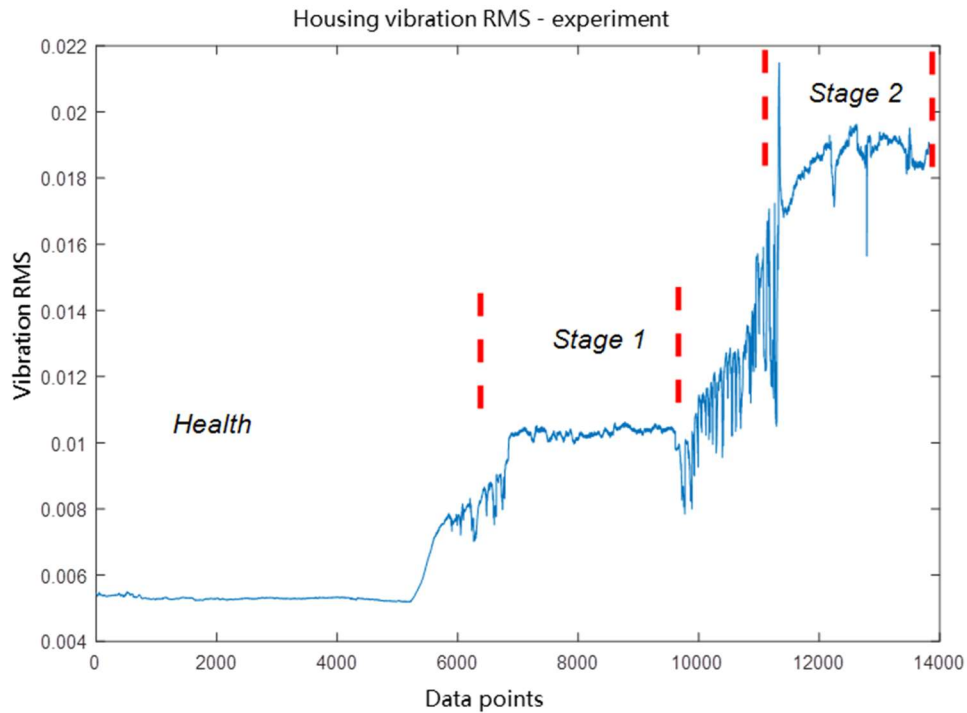
Figure 47 Housing vibration RMS for bearing deterioration experiment

The experiment consists of 3 phases: a normal operation phase with health bearings, and two stages with defected bearings of different deterioration levels. Each phase lasts about four days. A current is injected into the bearing cage between phases to damage the bearings. The deterioration period lasts about one day. According to ISO 10816, vibration RMS is preferred to evaluate the health status of the rotary machines. Thus, the vibration data is used both as the reference and to validate the ESA results.

The RMS value of housing vibration during the entire experiment is shown in Figure 47. Each data sample is collected in a 60 sec interval. The trending of the vibration indicator gives the transition of health condition of the bearing during its operational

lifetime. As the severity level of the bearing fault increases, the vibration also increases. Three phases are clearly isolated by the vibration indicator. The vibration level is raised by 100% compared to the health case after each deterioration phase. The ramping up trend shows the deterioration process resulting from the current injection. During the current injection phase, the vibration indicator is not as smooth as the phase when the injected current is removed. The reason is that when there is a shaft current, the vibration pattern is affected by the thermal effect and the unbalanced magnetic pull caused by the injected current, both of which cause a larger variation on the ramping up trend of the vibration indicator.

The vibration spectrums of the three phases are shown in Figure 48. The sampling frequency of the vibration DAQ is 12800Hz, according to which the bandwidth of the spectrum is 6400Hz, indicates that the vibration over a broadband increases as the condition of the bearing worsens. Because the vibration information is modulated on the electrical signals, the higher the frequency, the lower the amplitude of the modulated signal. 0~1000Hz is the frequency range of interest for ESA. The zoomed view of the vibration spectrum in Figure 48 (b) shows the series of peaks at 30Hz, 60Hz, 90Hz, …, etc., induced by the unbalanced rotor. The peaks show little change when the bearing condition deteriorates. The broadband changes of the spectrum are from 600Hz to 800Hz over the frequency band.

(a)   (b)
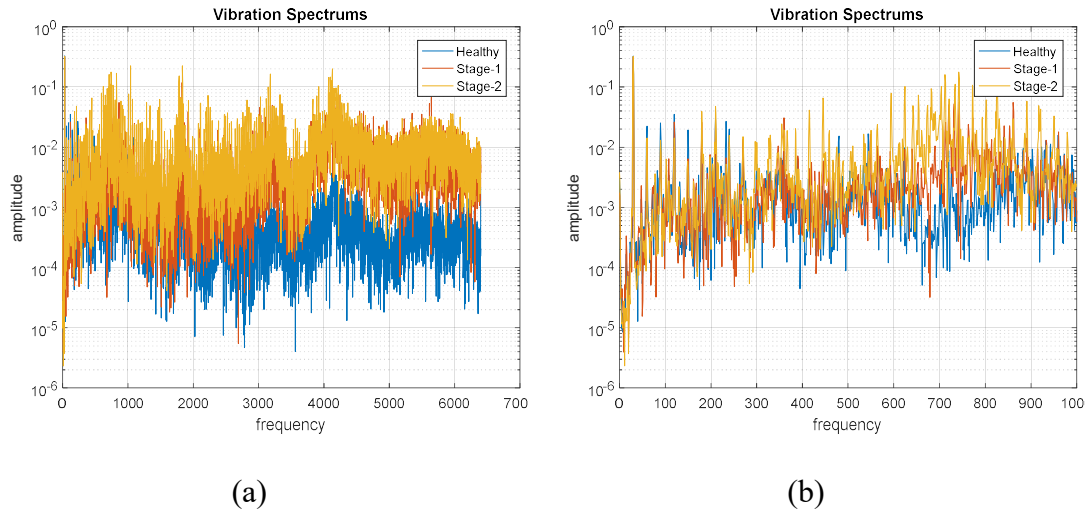
Figure 48 Vibration spectrums

During the long operation time, the electrical signal is sensitive to the environment variables and easily polluted by the loop current from the grid. The accumulated spectrum energy of the three selected bands which vary in different patterns is shown in Figure 49. Clearly, the time series of the variables are stochastic processes. The distribution of spectrum energy for the fundamental harmonics is mostly closer to the normal distribution as shown in Figure 49(b). The distributions of the spectrum energy for the 11th harmonics and the band (360Hz, 420Hz) are skewed to the lower values, which indicates that the high peaks in the time series are more likely to be noises.
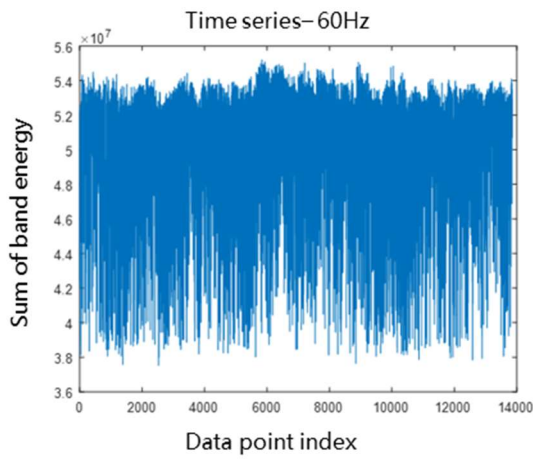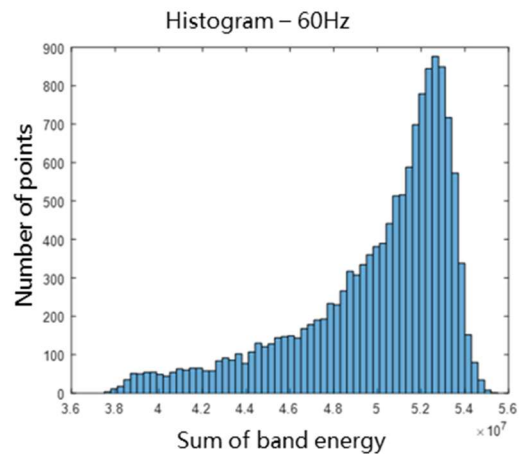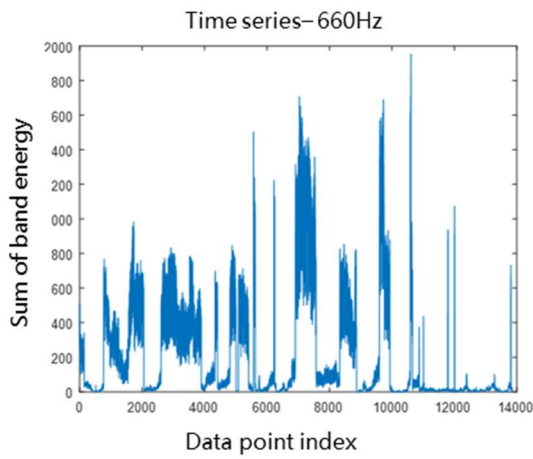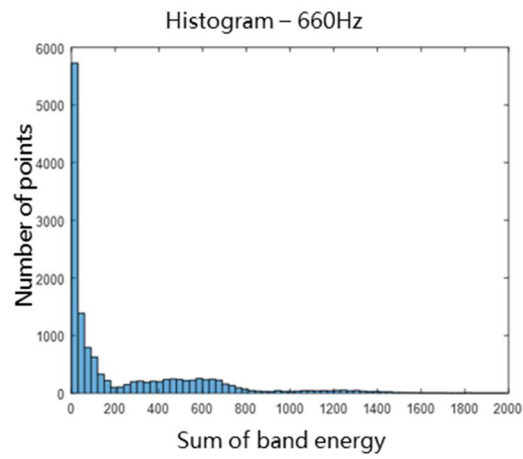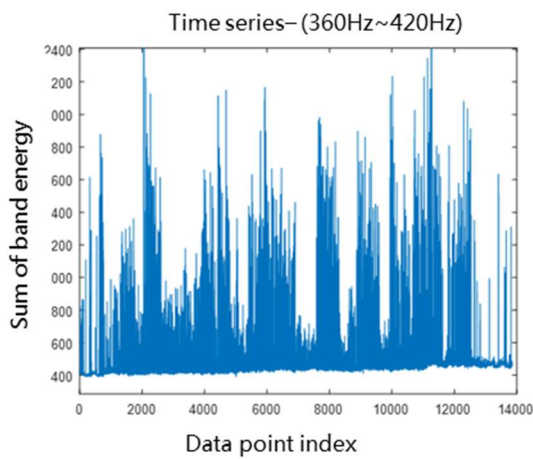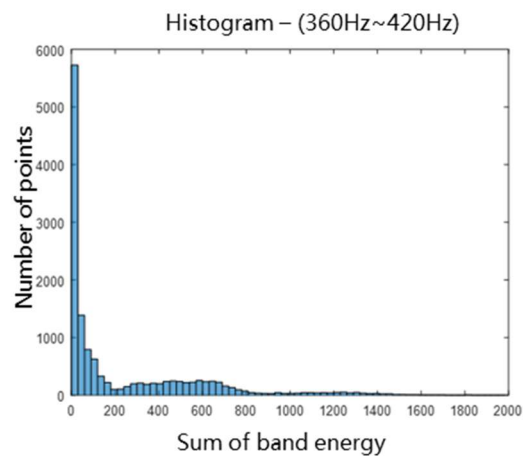
Figure 49 Time series and histograms of some features

The band (360Hz, 420Hz) is examined further to investigate the changes with bearing deterioration. Zooming in on the base line of the series indicates that the low values of the series are clearly separated into 3 stages as shown in Figure 51. According to the histogram plot of the variables in Figure 49, 80% of the points are in the range of 400 to 600, which are useful data for ESA. Moreover, if the whole dataset is used, the distribution of the variables eliminates the assumption that the probability distribution of x_i must be Gaussian. Thus, data segmentation should be applied to the dataset prior to extracting the fault information.
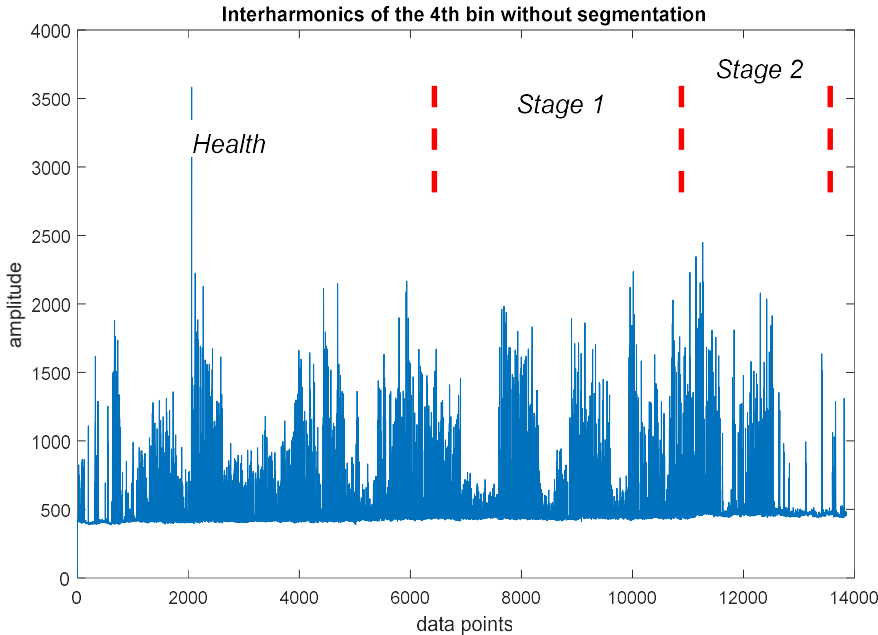
Figure 50 Inter-harmonics of 360–420Hz without segmentation
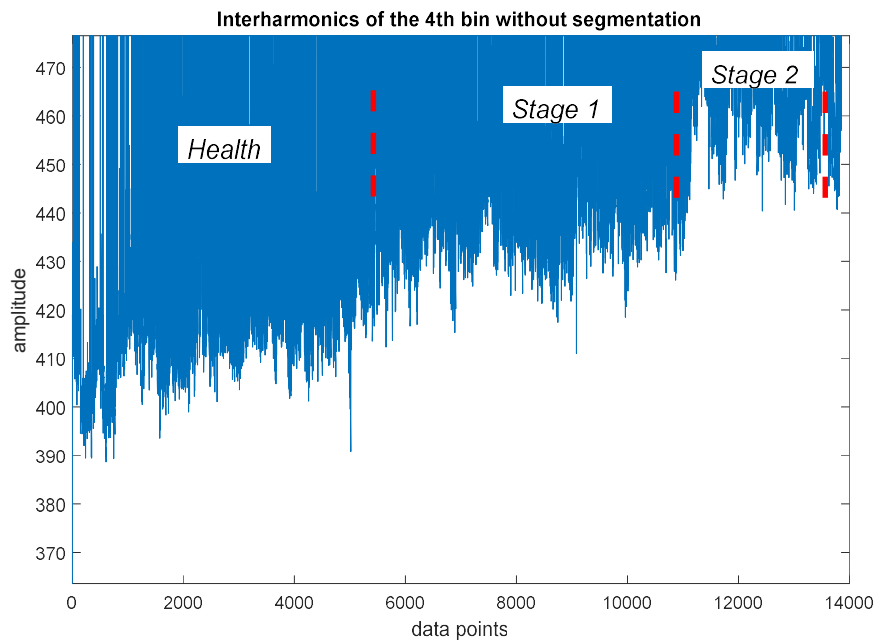
Figure 51 Inter-harmonics of 360-420Hz without segmentation (zoomed)

The correlation coefficients are calculated and summarized in Table 9. For simplicity, only part of the variables are listed. The correlation between variables is higher if the absolute value of the coefficient is larger. Note that all inter-harmonics to some extent are correlated in the same direction. The 11th harmonics is correlated in the opposite direction with the 7th and the 9th harmonics and has little correlation with the 3rd and the 5th harmonics. Based on the analysis, the vibration information appears on multiple bands in the selections and the basic assumption holds by applying the data segmentation method. After pre-processing the data, it is preferable to use PCA to extract the features from the correlated variables.

95

Table 9 Correlation coefficients of inter-harmonics and harmonics

	3rd	[180-240Hz]	[240-300Hz]	5th	[300-360Hz]	[360-420Hz]	7th	[420-480Hz]	[480-540Hz]	9th	[540-600Hz]	[600-660Hz]	11th
3rd	1.00	-0.03	-0.02	-0.04	-0.02	-0.01	0.08	-0.01	-0.03	0.05	-0.03	0.02	-0.06
[180-240Hz]	-0.03	1.00	0.84	-0.13	0.86	0.49	-0.12	0.73	0.83	0.08	0.67	0.32	0.04
[240-300Hz]	-0.02	0.84	1.00	-0.19	0.77	0.58	-0.20	0.68	0.74	0.08	0.64	0.50	0.15
5th	-0.04	-0.13	-0.19	1.00	-0.12	-0.40	0.19	-0.16	-0.13	-0.10	-0.16	-0.16	0.07
[300-360Hz]	-0.02	0.86	0.77	-0.12	1.00	0.49	0.00	0.84	0.81	0.14	0.65	0.28	-0.07
[360-420Hz]	-0.01	0.49	0.58	-0.40	0.49	1.00	0.02	0.54	0.47	0.29	0.50	0.54	-0.05
7th	0.08	-0.12	-0.20	0.19	0.00	0.02	1.00	0.03	-0.07	0.63	-0.15	-0.03	-0.81
[420-480Hz]	-0.01	0.73	0.68	-0.16	0.84	0.54	0.03	1.00	0.78	0.20	0.71	0.38	-0.12
[480-540Hz]	-0.03	0.83	0.74	-0.13	0.81	0.47	-0.07	0.78	1.00	0.17	0.84	0.35	0.01
9th	0.05	0.08	0.08	-0.10	0.14	0.29	0.63	0.20	0.17	1.00	0.24	0.30	-0.59
[540-600Hz]	-0.03	0.67	0.64	-0.16	0.65	0.50	-0.15	0.71	0.84	0.24	1.00	0.52	0.08
[600-660Hz]	0.02	0.32	0.50	-0.16	0.28	0.54	-0.03	0.38	0.35	0.30	0.52	1.00	0.04
11th	-0.06	0.04	0.15	0.07	-0.07	-0.05	-0.81	-0.12	0.01	-0.59	0.08	0.04	1.00

After using PCA on the segmented data, principal components #1 and #2 are shown in Figure 52 and Figure 53, respectively. Comparing Figure 52, Figure 54, and Figure 55 shows the harmonics distortion induced from the power quality variations is represented by principal component #1. The changes of harmonics distortion come from the same source and have a variation larger than the inter-harmonics, where the bearing faults information are most likely hidden.

The visually recognizable trend of principal component #2 is shown in Figure 53. The moving average operation is applied to smooth the change of the indicator. The trend shows that as the bearing deteriorates principal component #2 increases. The results prove that the electrical indicator created from the proposed method extracts the bearing faults from the electrical signals and shows a good agreement with the vibration indicator.
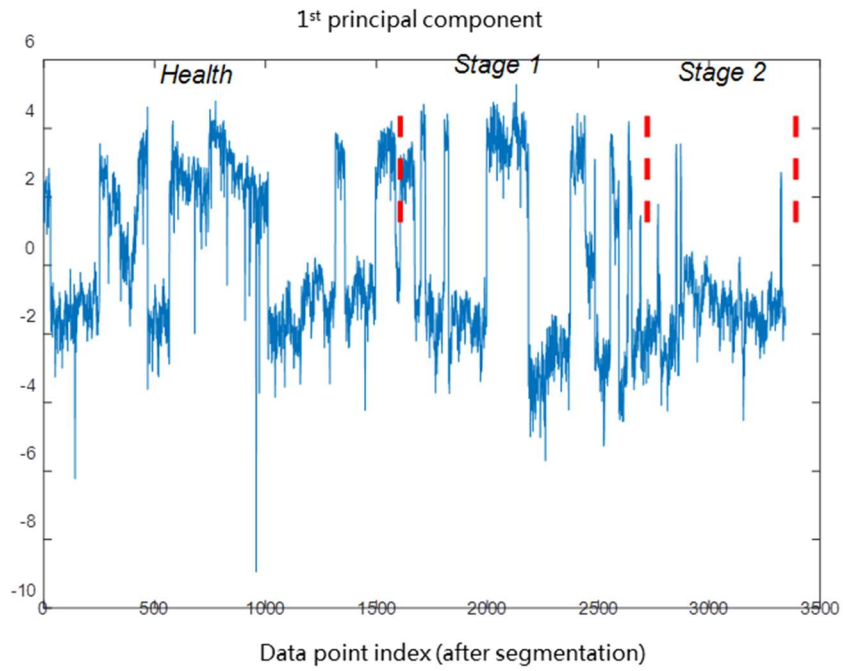
Figure 52 Principal component #1
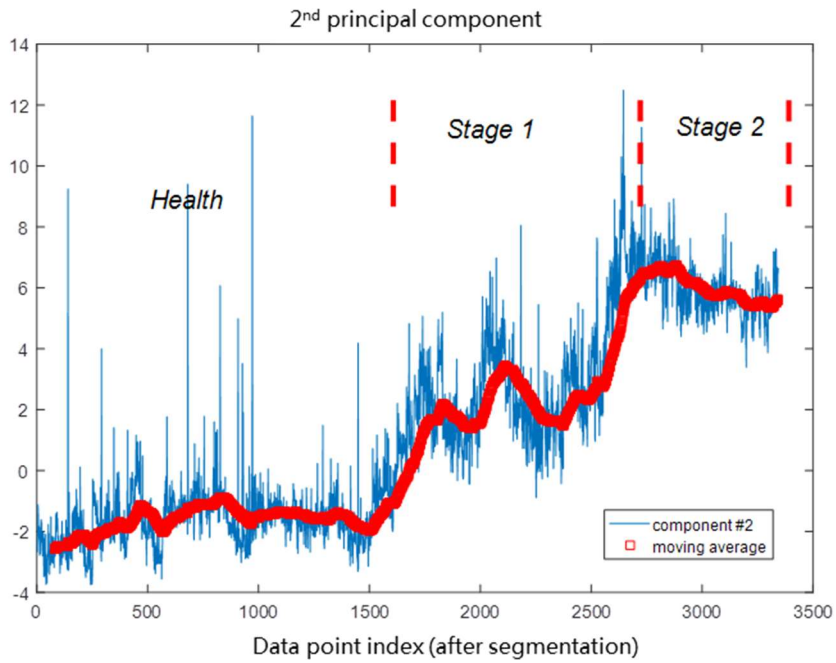
Figure 53 Principal component #2
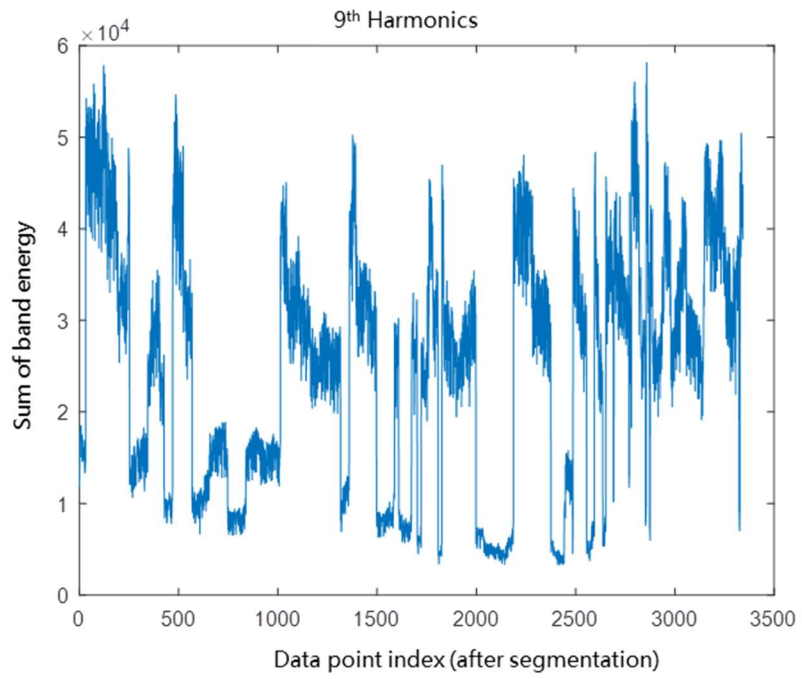
Figure 54 The 9th harmonics
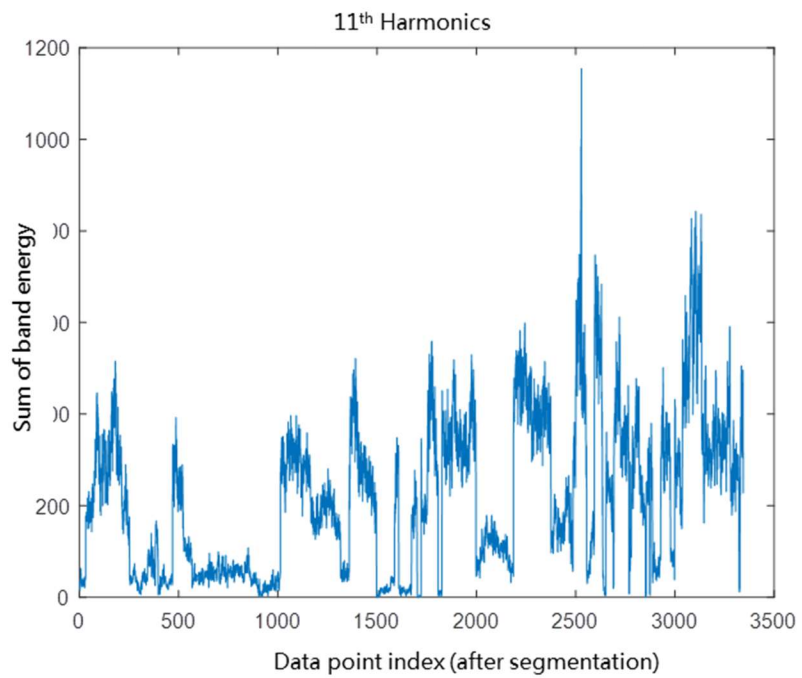
Figure 55 The 11th harmonics

CHAPTER V

SUMMARY AND FUTURE WORK

In this section, a summary of the research work discussed in earlier sections is presented. This dissertation was mainly concerned with developing a SPSM model which is good to analyze the relationship between the bearing defects and the electrical signatures. A new diagnosis technique based on the findings is also proposed.

5.1 Summary of Research

At the start of the dissertation, common failures of electrical machines are briefly overviewed. The causes of bearing anomalies and the detection techniques are discussed. An introduction of the development for bearing fault modeling is also presented. In the end, the research objectives and a roadmap of the proposed method are outlined.

In the following chapter, a winding function approach based method was introduced to model the SPSM. In this model, the actual winding distribution is used, which includes the space harmonics caused by the winding configuration. The airgap variation can be taken into account in the proposed model, which can be used to simulate the machine under different bearing anomalies. All machine inductances were calculated as a function of the rotor position using the winding function method, based on the geometry of the machine and its winding configuration. A simple method of modeling the dynamic eccentricity was also presented. The electromagnetic torque equation was derived, and the machine differential equations were given which are solved using Matlab. The simulated machine waveforms and their spectrums were presented for the cases

99

during different level of dynamic eccentricity at the steady state, for open circuit mode and loaded mode.

Then, to investigate the mechanism that how the bearing faults would affect the electrical signatures, a high fidelity rotor-bearing system with detailed nonlinear ball bearing model and a flexible finite element shaft model was built. Dynamic differential equation of the defect vibration model was numerically solved and the localized defect of the rolling element bearing was simulated by the ode solver in Matlab. The simulation result was theoretically analyzed and experimentally verified. The validity of the proposed defect model is thus verified. The simulation coupled both rotor bearing system and the electromagnetic circuit model of a SPSM was performed. It was found that the lateral vibration induced by bearing faults are modulated on the harmonics of the electrical signals, which could provide theoretical basis to the research on the potential condition monitoring and fault diagnosis algorithms of rolling element bearing in the future.

Spalls over an extended area on the bearing race surface caused by inject shaft current are more practical than localized single point bearing fault. In Chapter IV, the experiment data for the general roughness bearing faults was analyzed and a new method to process the non-stationary signals was proposed by applying ZFFT and PCA. The results demonstrated the capability of using electrical signals to detect bearing defects in a SPSM.

The main work of this research is to build an inter-coupled simulation model in bridging the gap between electromagnetic circuit modeling of the electrical system and

the dynamical modeling of the mechanical system. The following contributions are achieved through this research.

- A multi-physics model combining a detailed bearing model in a synchronous generator is developed, which allows introducing bearing faults

- SPSM voltages and currents under bearing defects induced air-gap variation and torsional vibration are analyzed

- A new fault detection method is proposed, which is capable of picking up the bearing faults in a noisy environment.

5.2 Suggestions for Future Work

An inter-coupled model developed in this research bridges the gap between electromagnetic circuit modeling of the electrical system and the dynamical modeling of the mechanical system. The model has been validated with FEM and experimental data to be a viable tool to analyze rolling element bearing faults. The proposed fault detection algorithm for bearing faults has proven to be effective in an experimental study. However, there are still some improvements to be done to make the model and the approach more reliable and extendable to more general cases.

- Damper winding and voltage fed field circuit could be taken into consideration, which may lead to the detection of failures through field current.

- The interaction of the rotor and the stator due to the unbalanced magnetic pull (UMP) could be explored and modeled.

- Shaft orbit profile could be obtained by Eddy current sensors through the experiment. This may provide a more direct way to validate the developed model.

101

- An ideal fault detection method should be load independent, so that it is more applicable for practical analysis. The influence of load changes on the proposed fault detection method should be examined in the future.

REFERENCES

[1] Greene; Hammerschlag; Keith, "Distributed Resources and Their Emissions: Modeling the Impacts," Natural Resources Defense Council(NRDC), 2001.

[2] I. Energy and Environmental Analysis, "Distributed generation operational reliability and availability database," 2004.

[3] A. Jar dine and B. Lin, "A review on machinery diagnostics and prognostics implementing condition-based maintenance," *Mechanical Systems and Signal Processing,* vol. 20, no. 7, 2006.

[4] S. Orhan, N. Akturk and V. Celik, "Vibration monitoring for defect diagnosis of rolling element bearings as a predictive maintenance tool: Comprehensive case studies," *NDT&E International,* vol. 39, 2006.

[5] R. B. Randall and J. Antoni, "Rolling element bearing diagnositics-A turorial," *Mechanical Systems and Signal Processing,* vol. 25, 2011.

[6] S. Nandi and H. A. Toliyat, "Condition monitoring and fault diagnosis of electrical machines-a review," in *IEEE IAS*, Phoenix,AZ, 1999.

[7] H. Haynes, E. D. and D. M., "Motor current signature analysis method for diagnosing motor operated devices". United States of America Patent 4,965,513, 14 November 1989.

[8]   O. Thorsen and M. Dalva, "A survey of faults on induction motors in offshore oil industry, petrochemical industry, gas terminals, and oil refineries," *Industry Applications, IEEE Transactions,* vol. 31, no. 5, pp. 1186-1196, 1995.

[9]   J. R. Stack, T. G. Habetler and R. G. Harley, "Fault classification and fault signature production for rolling element bearings in electric machines," *IEEE Transactions on industrial applications,* vol. 40, no. 3, 2004.

[10] G. Curcuru, M. Cocconcelli, F. Immovilli and R. Rubini, "On the detection of distributed roughness on ball bearings via stator current enery: experimental results," *Diagnostyka,* vol. 51, no. 3, 2009.

[11] J. R. Stack, T. G. Habetler and R. G. Harley, "Fault classification and fault signature production for rolling element bearings in electric machines," *IEEE Transactions on Industrial Application,* vol. 40, no. 3, 2004.

[12] N. Sawalhi and R. Randall, "Simulating gear and bearing interactions in the presence of faults: Part II: Simulation of the vibrations produced by extended bearing faults," *Mechanical Systems and Signal Processing,* vol. 22, no. 8, pp. 1952-1966, 2008.

[13] R. R. Schoen, T. G. Habetler, F. Kamran and R. G. Bartheld, "Motor bearing damage detection using stator current monitoring," *IEEE Transactions on Industry Applications,* vol. 31, no. 6, 1995.

[14] J. R. Stack, R. G. Harley and T. G. Habetler, "An amplitude modulation detector for fault diagnosis in rolling element bearings," *IEEE Transactions on Industrial Electronics,* vol. 51, no. 5, 2004.

[15] J. Yan, L. Lu, D. Zhao and G. Wang, "Diagnosis of Bearing Incipient Faults Using Fuzzy Logic Based Methodology," in *International Conference on Fuzzy Systems and Knowledge Discovery*, 2010.

[16] J. Rosero, J. Cusido, A. G. Espinosa, J. A. Ortega and L. Romeral, "Broken bearings fault detection for a permanent magnet synchronous motor under non-constant working conditions by means of a joint time frequency analysis," in *IEEE International Symposium on Industrial Elctronics*, Vigo, 2007.

[17] F. Immovilli, C. Bianchini, M. Cocconecelli, A. Bellini and R. Rubini, "Bearing fault model for induction motor with externally induced vibration," *IEEE Transactions on Industrial Electronics,* vol. 60, no. 8, 2013.

[18] W. Zhou, T. G. Habetler and R. G. Harley, "Bearing fault detection via stator current noise cancellation and statistical control," *IEEE Transactions on Industrial Electronics,* vol. 55, no. 12, 2008.

[19] J. R. Stack, T. G. Habetler and R. G. Harley, "Bearing fault detection via autregressive stator current modeling," *IEEE Transaction on Industrial Applications,* vol. 40, no. 3, 2004.

[20] B. Lu, M. NowakAn, S. Grubic and T. G. Habetler, "Adaptive noise-cancellation method for detecting generalized roughness bearing faults under dynamic load conditions," in *Energy Conversion Congress and Exposition*, San Jose, CA, 2009.

[21] S. Cheng, *Utilizing the connected power electronic converter for improved condition monitoring of induction motors and claw-pole generators,* Georgia Institute of Technology, 2012.

[22] F. Immovilli; M. Cocconcelli, "Experimental Investigation of Shaft Radial Load Effect on Bearing Fault Signatures Detection," *IEEE Transactions on Industry Applications,* vol. 99, pp. 1-1, 2016.

[23] F. immovilli, A. Bellini, R. Rubini and C. Tassoni, "Diagnosis of Bearing Faults in Induction Machines by Vibration or current signals: a Critical Comparison," *IEEE Transactions on Industry Application,* vol. 46, no. 4, 2010.

[24] N. W. Duncan, Torsional vibration of turbomachinery, McG-Hill, 2004.

[25] R. Yacamini, K. S. Smith and L. Ran, "Monitoring torsional vibrations of electro-mechanical systems using stator currents," *Jounal of Vibration and Acoustics,* vol. 120, no. 1, pp. 72-79, 1998.

[26] H.Kim, "On-line mechanical unbalance estimation for permanent magnet synchronous machine drives," *IET Electr. Power Appl.,* vol. 3, no. 3, pp. 178-186, 2009.

[27] X. Shi, J. Shao, J. Si and B. Li, "Experimental and simulation of rotor's torsional vibration based on sensorless detection technology," in *IEEE ICAL*, 2008.

[28] S. H. Kia, H. Henao and G.-A. Capolino, "Torsional vibration effects on induction machine current and torque signatures in gearbox-based electromechanical system," *IEEE Transactions on Industrial Electronics,* vol. 56, no. 11, 2009.

[29] R. Ong, J. H. Dymond and R. D. Findlay, "Bearing damage analysis in a large oil-ring-lubricated induction machine," *IEEE Trans. Ind. Electron.,* vol. 47, no. 5, pp. 1085-1091, 2000.

[30] G. M. Joksimovic, "Dynamic simulation of cage induction machine with air gap eccentricity," *Pro. Inst. Elec. Eng. - Elect. Power Appl.,* vol. 152, no. 4, pp. 803-811, 2005.

[31] J. R. Cameron, W. T. Thomson and A. B. Dow, "Vibration and current monitoring for detecting airgap eccentricitity in large induction motors," *IEE Proceedings,* vol. 133, no. 3, pp. 155-163, 1986.

[32] G. B. Kliman, "Methods of motor current signature analysis," *Elect. Mach. Power Syst.,* vol. 20, no. 5, pp. 463-474, 1992.

[33] H. A. Toliyat, M. S. Arefeen and A. G. Parlos, "A method for dynamic simulation of air-gap eccentricity in induction machines," *IEEE Transactions on Industry Applications,* vol. 32, no. 4, 1996.

[34] S. Nandi, H. A. Toliyat and A. G. Parlos, "Performance analysis of a single phase induction motor under eccentric conditions," in *IEEE Industry Application Society Annual Meeting*, New Orleans, Louisiana, 1997.

[35] S. Nandi, R. Mahan and H. A. Toliyat, "Performance analysis of a three-phase induction motor under mixed eccentricity condition," *IEEE Transactions on Energy Conversion,* vol. 17, no. 3, 2002.

[36] J. Gojko, M. Durovic and O. Aleksandar, "Skew and linear rise of MMF across slot modeling - winding function approach," *IEEE Transactions on Energy Conversion,* vol. 14, no. 3, 1999.

[37] X. Li, Q. Wu and S. Nandi, "Performance analysis of a three-phase induction machine with inclined static eccentricity," *IEEE Trans. Ind. Appl.,* vol. 43, no. 2, pp. 531-541, 2007.

[38] J. Faiz, B. M. Ebrahimi, B. Akin and H. A. Toliyat, "Finite-Element Transient Analysis of Induction Motors Under Mixed Eccentricity Fault," *IEEE Transactions on magnetics,* vol. 44, no. 1, 2008.

[39] H. A. Toliyat and N. A. Al-Nuaim, "Simulation and detection of dynamic air-gap eccentricity in salient-pole synchronous machines," *IEEE Trans. Industry Application,* vol. 35, no. 1, 1999.

[40] J. F. Tabatabei, H. Lesani and M. T. Nabavi-Razavi, "Modeling and simulation of a salient-pole generator with dynamic eccentricity using modified winding function theory," *IEEE Trans. Magnetics,* vol. 40, no. 3, pp. 1550-1555, 2004.

[41] M. Kiani, W. J. Lee, R. Kenarangui and B. Fahimi, "Detection of rotor faults in synchronous generators," in *IEEE International Symposium on Diagnostics for Electric Machines*, 2007.

[42] C. Bruzzese, A. Giordani and E. Santini, "Static and Dynamic Rotor Eccentricity On-Line Detection and Discrimination in Synchronous Generators By No-Load E.M.F. Space Vector Loci Analysis," in *International Symposium on Power Electronis, Electrical Drives, Automation and Motion*, 2008.

[43] C. Bruzzese, E. Santini, V. Benucci and A. Millerani, "Model-based eccentricity diagnosis for a ship brushless-generator exploiting the machine voltage signature analysis (MVSA)".

[44] T. Ilamparithi and S. Nandi, "Comparison of modified winding function approach and finite element method results for eccentric salient pole synchronous motor," in *IEEE International Conference on Power Electronics, Drives and Energy Systems*, Bengaluru, India, 2012.

[45] G. Joksimovic, C. Bruzzese and E. Santini, "Static eccentricity detection in synchronous generators by field current and stator voltage signature analysis - Part I: Theory," in *International Conference on Electrical Machines*, Rome, 2010.

[46] C. Bruzzese, G. Joksimovic and E. Santini, "Static eccentricities detection in synchrnous generators by field current and stator voltage signature analysis - Part II: Measures," in *International Conference on Electrical Machines*, Rome, Italy, 2010.

[47] A. B. Jones, "A general theory for elastically constrained ball and radial roller bearings under arbitray load and speed conditions," *Journal of Basic Engineering*, pp. 309-320, 1960.

[48] T. Harris, Rolling Bearing Analysis 3rd ed., John Wiley & Sons, 1991.

[49] P. Gupta, "Dynamics of rolling -element bearings, part 3: ball bearing analysis," *Journal of Lubrication Technology,* vol. 101, pp. 312-318, 1979.

[50] P. Gupta, "Dynamics of rolling element bearings - experimental validation of the DREB and RAPIDREB computer programs," *Journal of Tribology,* vol. 107, pp. 132-137, 1985.

[51] J. Datta and K. Farhang, "A nonlinear model for structural vibrations rolling element bearings: part 1-derivation of governing equations," *Journal of Mechanical Design,* vol. 100, pp. 229-235, 1978.

[52] P. McFadden and J. Simith, "Model for the vibration produced by a single point defect in a rolling element bearing," *Journal of Sound and Vibration,* vol. 96, no. 1, pp. 69-82, 1984.

[53] P. McFadden and J. Smith, "The vibration produced by multiple point defects in a rolling element bearing," *journal of Sound and Vibration,* vol. 98, no. 2, pp. 263-273, 1985.

[54] Linkai Niu, Hongrui Cao, , Zhengjia He, Yamin Li, "A systematic study of ball passing frequencies based on dynamic modeling of rolling ball bearings with localized surface defects," *Journal of Sound and Vibration,* vol. 357, pp. 207-232, 2015.

[55] Sarabjeet Singh, Carl Q. Howard, Colin H. Hansen, "An extensive review of vibration modelling of rolling element bearings with localised and extended defects," *Journal of Sound and Vibration*, vol. 357, pp. 300-330, 2015.

[56] D. Zarko, D. Ban, I. Vazda and V. Jaric, "Calculation of Unbalanced Magnetic Pull in a Salient-Pole Synchronous Generator Using Finite-Element Method and Measured Shaft Orbit," *IEEE Transactions on Industrial Electronics*, vol. 59, no. 6, 2012.

[57] DeBortoli, MJ and Salon, SJ and Burow, DW and Slavik, CJ, "Effects of rotor eccentricity and parallel windings on induction machine behavior: A study using finite element analysis," *IEEE Transactions on Magnetics*, vol. 29, no. 2, pp. 1676--1682, 1993.

[58] Vaseghi, Babak and Takorabet, Noureddine and Meibody-Tabar, Farid, "Transient finite element analysis of induction machines with stator winding turn fault," *Progress In Electromagnetics Research*, vol. 95, pp. 1-18, 2009.

[59] Toliyat, Hamid A., Thomas A. Lipo, and J. Coleman White, "Analysis of a concentrated winding induction machine for adjustable speed drive applications. I. Motor analysis," *IEEE Transactions on Energy conversion*, vol. 6, no. 4, pp. 679-683, 1991.

[60] Milimonfared, Jafar and Kelk, H Meshgin and Nandi, Subhasis and Minassians, AD and Toliyat, Hamid A, "A novel approach for broken-rotor-bar detection in

cage induction motors," *IEEE Transactions on Industry Applications,* vol. 35, no. 5, pp. 1000--1006, 1999.

[61] Joksimovic, Gojko M and Penman, Jim, "The detection of inter-turn short circuits in the stator windings of operating motors," *IEEE Transactions on Industrial Electronics,* vol. 47, no. 5, pp. 1078--1084, 2000.

[62] Akbari, Hamidreza and Meshgin-Kelk, H and Milimonfared, Jafar, "Extension of winding function theory for radial and axial nonuniform air gap in salient pole synchronous machines," *Progress In Electromagnetics Research,* vol. 114, pp. 407--428, 2011.

[63] Babaei, Mojtaba and Faiz, Jawad and Ebrahimi, Bashir Mahdi and Amini, S and Nazarzadeh, Jalal, "A detailed analytical model of a salient-pole synchronous generator under dynamic eccentricity fault," *IEEE Transactions on Magnetics,* vol. 47, no. 4, pp. 764--771, 2011.

[64] T. A. Lipo, Analysis of synchronous machines, Madison Wisconsin: Wisconsin Power Electronics Research Center, 2008.

[65] D. K. Cheng, Field and Wave Electromagnetics, New York: Addison-Wesley Publishing Company, Inc, 1983.

[66] G. M. Joksimovic, "Dynamic simulation of cage induction machine with air gap eccentricity," *IEE Proceedings of Electric Power Applications,* vol. 152, no. 4, pp. 803-811, 2005.

[67] Tallian, TE and Gustafsson, OG, "On competing failure modes in rolling contact," *ASLE transactions,* vol. 10, no. 4, pp. 418-435, 1967.

[68] K. Johnson, "The strength of surfaces in rolling contact," *Proceedings of the Institution of Mechanical Engineers, Part C: Mechanical Engineering Science,* vol. 203, no. 3, pp. 151-163, 1989.

[69] M. L. Adams, "Analysis of Rolling Element Bearing Faults in Rotating Machinery," Ph.D. dissertation, Department of Mechanical and Aerospace Engineering, Case Western Reserve University, Cleveland, OH, 2001.

[70] S. P. Harsha, "Nonlinear dynamic analysis of an unbalanced rotor supported by roller bearing," *Chaos, Solitons & Fractals,* pp. 47-66, 2005.

[71] R.R. Schoen, T.G. Habetler, and R.G. Bartheld, "Experimentally generating faults in rolling element bearings via shaft current," *IEEE Transaction on industrial,* pp. 25-29, 2005.

[72] Stack, Jason R., Thomas G. Habetler, and Ronald G. Harley, "Bearing fault detection via autoregressive stator current modeling," *IEEE Transactions on Industry Applications,* vol. 40, no. 3, pp. 740-747, 2004.

[73] Immovilli, Fabio, Marco Cocconcelli, Alberto Bellini, Riccardo Rubini, "Detection of generalized-roughness bearing fault by spectral-kurtosis energy of vibration or current signals," *IEEE Transactions on Industrial Electronics,* vol. 56, no. 11, pp. 4710-4717, 2009.

[74] A. Bellini, A. Yazidi, F. Filippetti, C. Rossi and G. A. Capolino, "High Frequency Resolution Techniques for Rotor Fault Detection of Induction Machines," *IEEE Transactions on Industrial Electronics,* vol. 55, no. 12, pp. 4200-4209, 2008.

[75] Lu, B., Nowak, M., Grubic, S., Habetler, T. G, "An adaptive noise-cancellation method for detecting generalized roughness bearing faults under dynamic load conditions," in *Energy Conversion Congress and Exposition*, San Jose, CA, USA, 2009.

[76] Sun, Weixiang and Chen, Jin and Li, Jiaqing, "Decision tree and PCA-based fault diagnosis of rotating machinery," *Mechanical Systems and Signal Processing,* vol. 21, no. 3, pp. 1300--1317, 2007.

[77] T. Harris, Rolling Bearing Analysis, New York: Wiley, 1991.

[78] M. N. a. H. T. A. Kotzalas, "Fatigue failure progression in ball bearings," *Transactions-American Society of Mechanical Engineers Journal of Tribology,* vol. 123, no. 2, pp. 238--242, 2001.

[79] A. Malhi ; R.X. Gao, "Feature selection for defect classification in machine condition monitoring," in *IEEE Instrumentation Measurement Technology Conference*, 2003.

[80] Pearson, Karl, "LIII. On lines and planes of closest fit to systems of points in space," *The London, Edinburgh, and Dublin Philosophical Magazine and Journal of Science,* vol. 2, no. 11, pp. 559-572, 1901.

[81] J. Shlens, "A tutorial on principal component analysis," [Online]

http://www.cs.cmu.edu/~elaw/papers/pca.pdf, 2003.

[82] H. Hotelling, "Analysis of a complex of statistical variables into principal

components," *Journal of Educational Psychology,* vol. 24, p. 417–441, 1933.